CHAPTER 3: Results and Discussion (Part-I)

Objective I: *Synthesis of Poly (N-Acryloylglycine-b-Acrylamide) Hydrogel And Evaluation For its Neuroprotective And Neuroregenerative Properties.*

3.1.1 ABSTRACT. In this work, glycine based-acryloyl monomer has been polymerized to obtain neurogenic polymeric hydrogel for regenerative applications. Synthesized poly(N-acryloylglycine-acrylamide) [poly(NAG-b-A)] nanohydrogel exhibits high swelling (~1500%) and is mechanically very stable, biocompatible and proliferative in nature. Poly(NAG-b-A) nanohydrogel provides a stable 3D extracellular mimetic environment and promotes healthy neurite growth for primary cortical neurons by facilitating cellular adhesion, proliferation, actin filament stabilization and neuronal differentiation. Further, the protective role of poly(NAG-b-A) hydrogel for the neurons in oxidative stress conditions has been revealed, and found that it is a clinically relevant material for the neuronal regenerative applications, such as for promoting nerve regeneration via the GSK3β inhibition. This hydrogel additionally plays an important role in modulating the biological microenvironment, either as an agonist, antagonist or as an anti-oxidant and favors the physiological responses and ease the neurite growth efficiency. Further, we found out that the conversion of glycine based acryloyl monomer into their corresponding polymer modulates the mechanical performance, mimics the cellular microenvironment and it accelerates the self-healing capacity due to the responsive behavior reactive oxygen species (ROS). Thus, p(NAG-b-A) hydrogel could be a potential candidate to

induce the neuronal regeneration, since it provides the physical cue and significantly boosts the neurite outgrowth along with maintaining the microtubules integrity in neuronal cells.

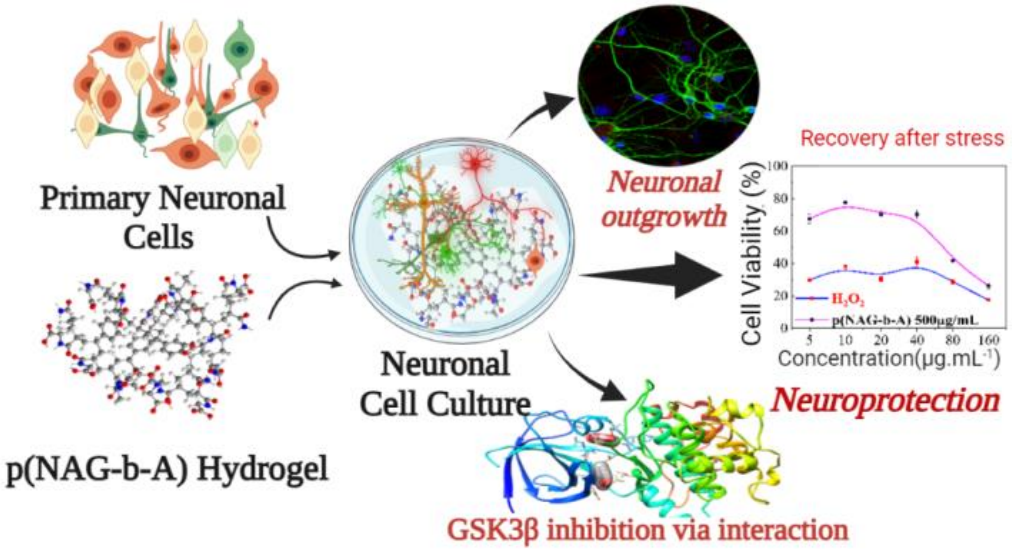

***Table of Contents**: poly(N-acryloylglycine-acrylamide) nanohydrogel can mimic cellular environment, an inhibitor of GSK3β, promotes in vitro neuronal growth and protective from the severe oxidative stress.*

3.1.2 INTRODUCTION

Neural regeneration is clinically challenging, while progressive neuronal damage causes severe consequence like Alzheimer's disease (AD) and Parkinson's disease (PD) and there is limited options for the treatment.[1-3] However, neurotransmitters act as trophic factors in immature nervous system, which influences the cellular proliferation, differentiation, migration of neurons, axonal growth and development of neuronal circuits.[4,5] Disruption in neurotransmitters leads to excitatory/inhibitory imbalance and it causes severe neurological disorders.[6] Glycine is a well-known inhibitory neurotransmitter in adult mature neuron and it generates the first electrical signal in immature neurons during embryogenesis.[6] Glycine further promotes neurogenesis via promoting calcium transients in neuronal stem cells, which

further helps to enhance the inter-neuron and neurogenic program.[7, 8] On the other hand, insulin like growth factor-1 (IGF-1) can induce the proliferation and differentiation, because it initiates activation of downstream substrate PI3K and AKT, and phosphorylate the glycogen synthase kinase 3 (GSK3β) at SER9. This phosphorylated GSK3β leads the GSK3β inhibition.[9, 10] The over expression of GSK3β in adult neurons is one of the responsible component for the faster neuronal death in injury, AD and PD.[11] Therefore, GSK3β could be a potential target in regenerative medicine. However, reports on the glycine and glycine derivative mediated GSK3β inhibition are limitedly available. It can also be noted that glycine elucidated by intracerebral ventricular delivery of glycine-proline-glutamate, which prevents the loss of astrocytes, and reduces the caspase-3-dependent and -independent apoptosis in hippocampus.[12] The modulation and role of the glycine based polymer in neurogenesis is still unknown. Therefore, there is a huge scope to overcome clinical challenges prevailing with the existing polymers and hopefully glycine-based polymers will help to develop the biological clue and to improve the therapeutic efficiency.

In the above line, in this work glycine has been used as a small molecule and precast into polymeric hydrogel to mimic the cellular microenvironment for promotion of neurite growth. Small molecule-based polymers demonstrate increased molecular weight, modulating the material property such as mechanical strength and consequently regulate the biological behavior.[13] Bio-functionalized self-assembled peptide and injectable hydrogels provide higher cytocompatibility with structural and mechanical similarities, stabilize the extracellular matrix components and provide the biological cue mimicking the neural environment.[14] It is also important to note that the neurite outgrowth is important for the nerve regeneration[3] and the

effort has been intended in this direction through the present work using the synthesized N-acryloylglycine based polymeric hydrogel.

It is observed that amino acid based polymers are biologically active and helpful for the release of fibroblast growth factor (FGF), promotes the toxin binding activities and protein-protein inhibition activities.[15,16] Amino acid derived acrylic polymer such as poly(acrylic acid), poly acrylamide, poly-(N-acryloyl glycinamide) etc. are studied for their upper critical solution temperature behavior.[17] Poly(N-acryloyl glycinamide) possesses gelling property, robust adhesion behavior and promotes wound healing efficacy[18] and exhibits osteo-regeneration properties.[19] Similarly, poly-(N-acryloyl glycine) (PNAG) shows the pH- and thermo-responsive drug releasing behavior.[20] A number of natural and synthetic polymers such as chitosan, alginate, natural silk, polymers of lactic and glycolic acids etc. were evaluated for neural regeneration.[2] Self-assembled peptide conjugated with nanoparticles were also used for neurite/axonal outgrowth with improved myelination.[21] Similar to chemical properties, the mechanical stability of the materials controls the neuronal regeneration and glial differentiation.[22] Despite the continuous research, still neuronal repair is the challenging task because CNS follows the break system, which limits the regeneration property with maturity.[23] Hence, incorporation of controlled topography and biochemical cue can facilitate the redevelopment of biological system.[24] However, development of materials with biochemical cue are challenging.

Herein this work, we have reported the proof of the concept of the use of poly(N-acryloyl glycine-acrylamide) p(NAG-b-A) co-polymeric hydrogel and studied efficiency of the neuronal growth and neuroprotective role in oxidative stress conditions. First, we have prepared a ‘mer’ with glycine and N-acryloyl chloride and then we have synthesized the co-

polymeric p(NAG-b-A) hydrogel using AIBN as initiator and DVB as a cross-linking agent and characterized for structural, chemical and mechanical properties. Then we have studied the response towards the primary neuronal cells and PC12 differentiated cells in oxidative stress conditions to check the neuron regenerative properties of the synthesized p(NAG-b-A) hydrogel. For the neurite growth the swelling of the hydrogel and the pH at the local environment is important and therefore, the swelling behavior has been studied at physiological temperature (37 ^{o}C) and at different pH (3-8). The mechanical stability of the hydrogel is important to modulate and mimic the microenvironment for neuro-regeneration, which has been studied in the physiological temperature range using rheological measurement. The cell viability of the hydrogel has been studied through the various cell-based studies using PC12, Hek293, and HepG2 cell lines. The primary cortical neurons were isolated from Wistar rats and neuron regenerative properties were studied. The growth of the neurons has been studied up to 21 days of post treatment with the hydrogel and the morphology and the nature of the growth such as 3D reconstruction, morphology, and co-localization have been studied using immunofluorescence staining. Additionally, extensive *in silico* molecular interaction studies were performed to analyze the behavior of glycine, N-acryloylglycine (NAG) monomer, and co-polymeric p(NAG-b-A) hydrogel in GSK3β inhibition for the neuronal growth. Further, the neuronal cells are vulnerable to oxidative damage and imbalance between generation of free radicals and antioxidant defense often lead to oxidative stress followed by the neuro-pathological conditions.[25] In order to elucidate the applicability of p(NAG-b-A) hydrogel in clinical settings, PC12 cells were grown in presence of oxidative stress generated by H_2O_2 and treated with the p(NAG-b-A) hydrogel. In order to establish the mechanism of the interactions between neurons and hydrogel, the macromolecule preparation and energy minimization were

conducted on UCSF Chimera 1.10.2 with 100 steepest descent steps by applying AMBER ff14SB and ligand structure, as well as through the energy minimization approach and by applying MMff94 force field. The molecular docking was performed by using the Autodock 4.2 tool to check the molecular interactions. Finally, the impact of the glycine moiety and its conversion into copolymer hydrogel to check whether it provides the physical cue or not and significant role to boost the neurite outgrowth along with maintaining the microtubules integrity in neuronal cells has been studied.

3.1.2. EXPERIMENTAL

3.1.2.1. Synthesis of N-acryloyl glycine. N-acryloyl glycine (NAG) monomer was synthesized according to our previously reported method (*Patent No.: 419638, Granted on. 30-01-2023*).[26]

3.1.2.2. Preparation of poly(N-acryloylglycine-acrylamide) co-polymeric hydrogel. Brief of the copolymer synthesis method has been shown in Scheme 3.1.1. Poly(NAG-b-A) co-polymeric hydrogel was prepared by a free radical mini-emulsion polymerization approach (mentioned in chapter2). Detail method was reported in an Indian Patent (*Patent No.: 419638, Granted on. 30-01-2023*).

3.1.2.3. Characterization of NAG and p(NAG-b-A) co-polymeric hydrogel. Functional groups and structural analysis were confirmed through FTIR, ^{1}H NMR and ^{13}C NMR spectroscopy. The molecular weight of p(NAG-b-A) was calculated by MALDI-TOF (MS: Bruker AutoFlex Speed MALDI ToF). Thermal stability was studied with TGA (a TGA-50 TGA instrument), Phase transition of polymer was studied through DSC (DSC-60 Plus), X-

Ray diffraction (XRD) patterns of the samples were recorded in between 2θ = 5 to 90° using a HR-XRD (Rigaku Smart Lab 9 kW Powder type) equipped with Cu Kα X-Ray radiation source of λ = 1.54 Å).

3.1.2.4. Morphological evaluation. Morphology and 3D structural analysis of p(NAG-b-A) co-polymeric hydrogel was characterized by field- emission scanning electron microscopy (FESEM) (Model: Nova Nano SEM 450) with the accelerating voltage of 15 kV and with High-resolution transmission electron microscopy (HRTEM) (model: Technai G2 20 TWIN).

3.1.2.5. Swelling behavior of poly(NAG-b-A) co-polymeric hydrogel. To find out the dynamic swelling behavior of the prepared p(NAG-b-A) nanohydrogel, a defined amount of hydrogel was taken and then incubated in the PBS buffer of different pH such as 3, 5, 6, 7.4 and 8 at room temperature (25 ^{o}C). After the specified time interval, both the weight and volume of the swelled hydrogel were recorded. The Mass Swelling Index (MSI) and Volume Swelling Index (VSI) was calculated by the eq. (3.1.1) and eq. (3.1.2):

$$\text{MSI} = \frac{Ws - Wi}{Wi} * 100 \dots \dots \dots (3.1.1)$$

$$\text{VSI} = \frac{Vs - Vi}{Vi} * 100 \dots \dots \dots (3.1.2)$$

Where W_s = weight of swollen hydrogel, W_i = initial dry weight of hydrogel, V_s = swelled volume of hydrogel and V_i = initial dry weight of hydrogel. All the experiments were performed in triplicates.

3.1.2.6. Rheological behavior of hydrogel. Rheological characterization of the hydrogels was performed using an Anton Paar MCR 102 Rheometer with parallel plate (30 mm diameter). The frequency sweep tests were conducted to evaluate the change in the viscoelastic modulus as a function of angular frequency (0.1-100 rad s^{-1}) with an oscillating strain of 5%.

The temperature ramp test was carried out to determine the relationship between viscoelastic modulus and loss modulus (G″), and storage modulus (G′) and the complex viscosity as a function of angular frequency and temperature.

3.1.2.7. In vitro cytotoxicity assay. The cytotoxicity and neurotoxicity of p(NAG-b-A) copolymers were assessed through the MTT assay on PC12, Hek293, and HepG2 cell lines. All cell lines were acquired from NCCS, Pune repository, India., to evaluate the material response under the stress conditions, PC12 cells were treated with different concentration (10, 20, 40, 80 and 160 μM) of H_2O_2 and were treated with 100 μg mL^{-1} and 250 μg mL^{-1} concentrations of hydrogel (in presence of stress and by removal of stress) and cell viability was measured using MTT assay.

3.1.2.8. Animal Ethics Permission. Animal work involved in this project was approved by the Institute Animal Ethical Committee of IIT (BHU), Varanasi, Uttar Pradesh, India (Regd. No. 2123/GO/Re/S/21/CPCSEA (IAEC Approval Number: IIT(BHU)/IAEC/2022/079). All the experimental procedures and handling of the animals were followed as per the ethical guidelines.

3.1.2.9. Immunofluorescence Staining. The 3 x 10^6 primary neuronal cells were loaded on the hydrogel as well as in poly(L-lysine) coated 12 well plate with neurobasal media supplemented with 10% FBS, 1X B27 and 50 ng NGF. After incubation of different time intervals as per the experimental design, the cells were fixed by 4% paraformaldehyde in PBS for 20 min followed by incubation with chilled methanol and then permeabilization was conducted for 20 mins with 0.1 wt % Triton X-100 in 1X PBS. Cells were blocked with 2% BSA for 1 h at room temperature. Further, the blocked cells were incubated for overnight at 4 °C with primary antibody β-tubulin III (1: 500) in 0.1% BSA followed by 1 h incubation with

secondary anti-mouse antibody (1:1000), Rhodamine phalloidin and Hoechst 33258. It can be noted that in each step of transition the cells were washed with 1X PBS for three times. Then confocal microscopy images were acquired using a LSM780 Carl Zeiss confocal microscope (Make Germany) for 3D visualization, and Z-stack images were then imported into Fiji J software[27] for 3D reconstruction, morphological analysis, and co-localization.

3.1.2.10. In-vitro recovery from oxidative stress. To evaluate the material's response in stress condition, 1 x 10^4 PC12 cells per well were seeded on 96 well plate with FBS supplemented complete DMEM media and incubated in CO_2 incubator at 37 ℃ for 24 h. For the measurement of protective role, the cells were treated with different concentrations of H_2O_2 (10, 20, 40, 80 and 160 μM) and treated with 500 μg mL^{-1} of hydrogel and the cell viability was estimated using MTT assay. Similarly, for the evaluation of recovery status, after 24 h of incubation 1 x 10^4 cells per well, they were treated with different concentrations of H_2O_2 (10, 20, 40, 80 and 160 μM) and again incubated for 12 h in 5% CO_2 supplemented humidified environment. After 12 h, complete H_2O_2 treated media removed and cells were treated with 500 μg mL^{-1} concentration of hydrogel and cell viability was estimated using MTT assay. Further for macroscopic examination, 500 μg mL^{-1} (in 1X HBSS solution) of hydrogel was coated on sterile coverslip and placed in 12 well plate. 1 x 10^5 cells per well were seeded in a 12 well plate for 24 h and treated with 40 μM concentration of H_2O_2 for another 24 h followed by AO/EtBr staining. After, staining cells were fixed with 4% paraformaldehyde and fluorescent macroscopic images were acquired. Similarly, to analyze the protective role of hydrogel on differentiated neurons, 1x10^5 cells per well were seeded on 500 μg mL^{-1} hydrogel coated slide and differentiated by providing 50 ng NGF supplemented DMEM complete media for 3 days. Then differentiated neurons were treated with 40 μM concentration of H_2O_2 for 24

h and then Immunolabeling was performed as mentioned in the subsequent sections. After Immunolabeling, confocal macroscopic images were acquired and evaluated for the morphology. To elucidate the p(NAG-b-A) hydrogel assisted protective role, 500 μg mL^{-1} of p(NAG-b-A) hydrogel was treated with 40 μM concentration of H_2O_2 in 1.5 mL centrifuge tube for 24 h at 37 ℃. Further, hydrogel was centrifuged and lyophilized. Then the Raman and FTIR spectroscopic analysis were performed and the results were compared with the untreated hydrogel.

3.1.2.11. Protein ligand interaction screening. Molecular docking approach was used to determine the nature of interactions between the NAG monomer and different unit of the polymeric units like dimer of N-acryloylglycine-N-acryloylglycine (G-G), N-acryloylglycine- acrylamide(G-A); trimer of N-acryloylglycine-N-acryloylglycine-N-acryloylglycine (G-G-G), N-acryloylglycine-N-acryloylglycine-acrylamide (G-G-A; G-A-G; G-A-A) and with GSK3β protein PDBID-1q5k (https://www.rcsb.org/structure/1Q5K).

3.1.2.12. Statistical analysis. All data presented were confirmed using at least 3 replicates for each of the experimental groups. The results are expressed as the mean of the values ± standard error of the mean. One-way ANOVA was performed to determine the statistical significance ($p < 0.05$), unless otherwise stated.

3.1.3. RESULTS

3.1.3.1. Synthesis: The N-acryloyl glycine (NAG) monomer was synthesized in the presence of potassium hydroxide. Acryloyl chloride reacts with glycine, by applying the basic principle of Shorten-Baumann reaction mechanism.[28] Further, acidification of aqueous phase followed by saturation with NaCl and extraction with ethyl acetate improves the yield of the monomer (Scheme 3.1.1). Copolymerization of NAG monomer and acrylamide was

accomplished by free radical polymerization by using radical initiator AIBN in 1,4 dioxane solution. In the presence of AIBN, vinyl groups of acryloyl glycine and acrylamide monomer form the linear aliphatic chain containing polymer. The use of DVB in small amount and the presence of two vinyl group yield high swelling capacity containing cross linked polymers.[29] Generally, DVB yield the highly branched polymer, however use of DVB in mini-emulsion process produced the spherical shaped cross linked polymeric hydrogel (Scheme 3.1.1 and Scheme 3.1.2).

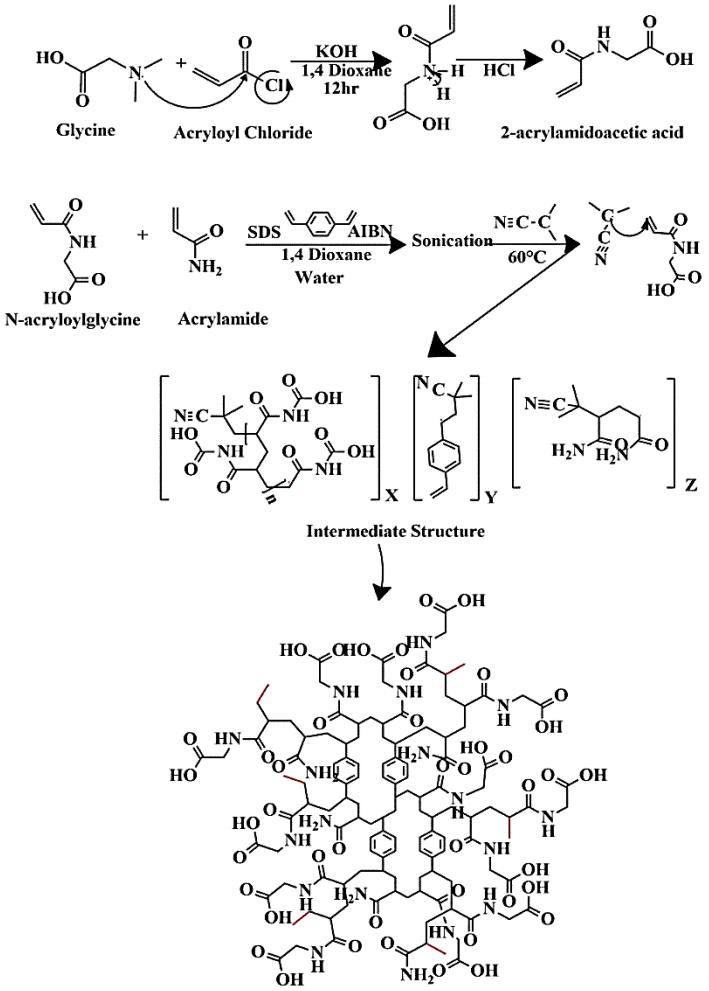

Scheme3.1. 1 Shows the probable mechanism involved in the synthesis of poly(N-acryloylglycine-acrylamide) hydrogel.

.

3.1.3.2. Physical and physicochemical properties of hydrogel. Chemical functionalities of synthesized N-acryloylglycine (NAG) were confirmed through FTIR (Figure S3.1.1), ^{1}H NMR (Figure S3.1.2a) and ^{13}C NMR (Figure S3.1.2b). The p(NAG-b-A) copolymer was synthesized and characterized through FTIR, ^{1}H NMR and ^{13}C NMR. FTIR spectrum of p(NAG-b-A) (Figure S3.1.3) confirmed the presence of characteristic bands at 3409 cm^{-1}, and 1725 cm^{-1} due to the presence of ─NH (stretched)/-OH and for C=O (aliphatic ketone), respectively. An overtone band of ─OH appeared at 1547 cm^{-1}. The sharp bands appeared at 2930 cm^{-1}, 1408 cm^{-1} and 1220 cm^{-1} due to the presence of aliphatic alkane (─CH_2), C=C and -C-N (stretching of amine), respectively. ^{1}H-NMR ($CDCl_3$) spectrum (Figure S3.1.4a) of p(NAG-b-A) confirmed the formation of cross-linked polymer with chemical shifts (δ in ppm) at 12.8 (O─H of carboxylic acid), 8.3 (N─H of 2° amine), 7.26 ($CDCl_3$), 6.8 (Aromatic-H), 4.7 for the ─CH_2. Similarly, in ^{13}C NMR spectra (Figure S3.1.4(b)) all the chemical shifts which were observed for NAG monomer are found disappeared in p(NAG-b-A) hydrogel and 44 ppm (45.36 ppm, 45.26 ppm, 45.09 ppm, 44.99 ppm, and 44.81 ppm) are the splinted peak of 2° alkanes which conform the synthesis of p(NAG-b-A) hydrogel. To evaluate the solubility, 1 mg of the p(NAG-b-A) hydrogel immerged in 1 mL any of the solvent or their mixture (e.g., water, terahydrofuran, toluene, chloroform, methanol, acetonitrile, acetone and in dimethylformamide, tetra chloromethane etc.). Among these solvent p(NAG-b-A) hydrogel shows swelling behavior in water, partial solubility in toluene, chloroform and tetra chloromethane. However, it is insoluble in other solvent (Figure S3.1.5a) with in 12 hour of incubation with stirring. MALDI-ToF was performed using ditharnol matrix and chloroform as a solvent (Figure S3.1.5(b-c)). Since the hydrogel nanoparticles are cross-linked polymers, therefore, the molecular weight obtained is Mc, i.e., molecular weight of the chain length

between two adjacent cross-links. Figure S3.1.5(b-c) shows the hetrogenous fragments of MALDI-ToF spectrum which evident that the maximum molecular weight (MW) of p(NAG-b-A) hydrogel ranging in between 1357 to 3106 Da. However, the maximum intensity for the MW is achieved to be 1357 Da. The repeating unit are varied from 200 to 120 and shows the heterogeneous population, which conform the formation of random and cross linked polymer. The first highest fragment was observed at Mw = 1357 (m/z), Mn = 1327 (m/z) and PDI ≈ 1.02, second highest fragment Mw = 1538 (m/z), Mn = 1550 (m/z) with of PDI ≈ 1.00. Similarly, in the repeated intrapersonal variable batch, the first highest fragment was observed at Mw = 1357 (m/z), Mn = 1309 (m/z) and PDI ≈ 1.03, second highest fragment 1596 (m/z), 1527 (m/z) with PDI ≈ 1.04. From these results, it can be concluded that the fragment sets are random, however the synthesis method shows the repeatability.

Thermal stability of p(NAG-b-A) co-polymeric hydrogel was evaluated by TGA (Figure S3.1.6a-b). Hydrogel is stable at physiological temperature (i.e., at 37 ^{o}C). The weight loss (7.45 wt%) in TGA (Figure S3.1.6a) around 100 ℃ has been observed due to the loss of moisture. However, hydrogel is stable up-to 220 ℃ and weight loss above this temperature occurs due to the thermal decomposition. Some residue of the hydrogel still remained beyond 500 ℃. To identify the thermal phase transition of p(NAG-b-A) hydrogel, DSC was recorded from -140 ℃ to 550 ℃ (Figure S3.1.6b). The glass transition temperature of the hydrogel is observed to be at -20.11 ℃. The broad endothermic transition observed at 69 ℃ (ΔH= 86.22 J g^{-1}) was due to the loss of moisture or for some low molecular weight mass. A second endothermic transition was observed at 210 ℃ due to the melting of the block-copolymer hydrogel. Exothermic heat flow is observed from 300 ℃ and above, due to the degradation (weight loss) of the polymer, which matches well with the TGA (Figure S3.1.6a) and obtained

due to the degradation of polyamide ketone and nitrile derivatives.[30030032] The acrylamide was cross-linked with DVB and due to heating, the evolution of NH_3 was started at 210 ℃ which can be correlated with the TGA results of p(NAG-b-A).[33] However, the DVB-associated cross-linking bonds in copolymer hydrogel enhances the thermal stability of the synthesized hydrogel.[31, 32] The alkene evolution was started from 480 ℃ and it was continued until 600℃.[33]A similar phenomenon was observed when (amylamide-sodium acrylate) copolymer was pyrolyzed at 492 ℃ and the carboxylate residue remained.[34] Therefore, the observed 49% residue obtained due to the presence of highly stable cross-linked parts generated due to the DVB (a cross-linker) and carboxylate functional parts of the hydrogel.

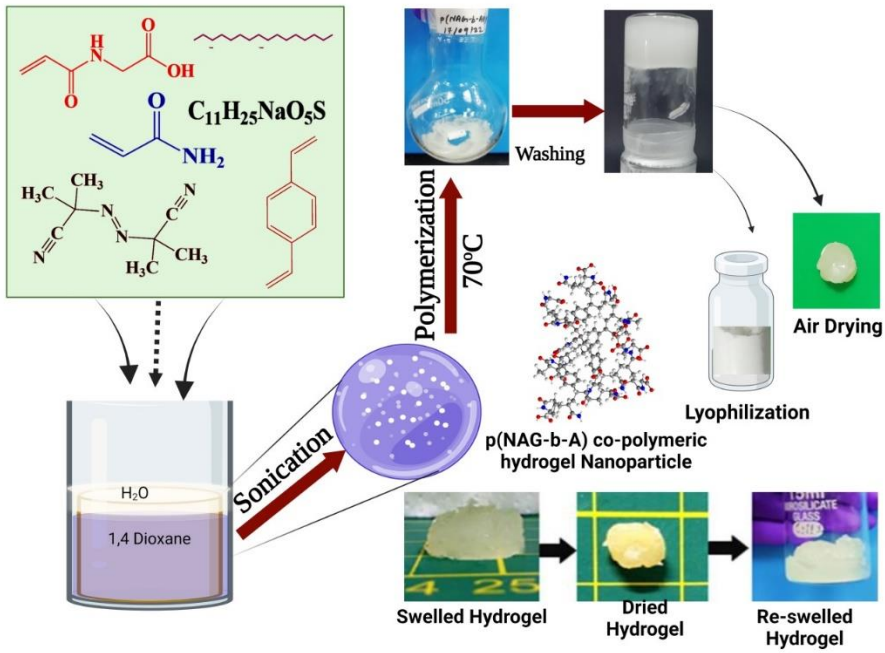

Scheme3.1. 2 Synthesis of poly(N-acryloylglycine-acrylamide) co-polymeric hydrogel and various processing steps to achieve its different forms.

3.1.3.3. Morphology of p(NAG-b-A) co-polymeric hydrogel. Particle size and morphology of the p(NAG-b-A) hydrogel was confirmed through the SEM and HRTEM

(Figure 3.1.1). SEM images confirmed the particle size of 20-40 nm in diameter (Figure 3.1.1a, b). From HRTEM (Figures 3.1.1c-d), the particle size was calculated to be 25-30 nm in diameter (Figure 3.1.1e). It is also revealed that the hydrogel nanoparticles are co-connected to each other through the cross-linking and helps to create macropores (HRTEM Figure 3.1.1c). Further, HRTEM (Figure 3.1.1d) revealed that the polymeric hydrogel particles are porous in nature and the pore sizes are calculated to be 1.8 to 2.5 nm in diameter (Figure 3.1.1f). It can also be noted that these pore sizes can expand during the hydrogel swelling in a similar ratio as of hydrogel. In HRTEM micrograph (Figure3.1.1d), it is observed that the fringes of the semicrystalline plains are formed due to the cross-linking of the polymeric chains and the distance between the two adjacent fringes is calculated to be 2 nm. Further, the semi crystalline nature of the polymer has been confirmed through the XRD (Figure 3.1. S7). XRD pattern of NAG mers show the major crystalline peaks appeared at $2\theta = 11.18^{o}$, 16.3^{o}, 21.2^{o}, 22.32^{o} and 27.16^{o} in addition with a broad crystalline peak appeared at $2\theta = 20^{o}$ with the 87% of crystallinity (Figure S3.1.7a). Whereas, the hydrogel nanoparticles are found to be semi-crystalline in nature and exhibited a broad diffraction peak at $2\theta = 20^{o}$ (Figure S3.1.7b).

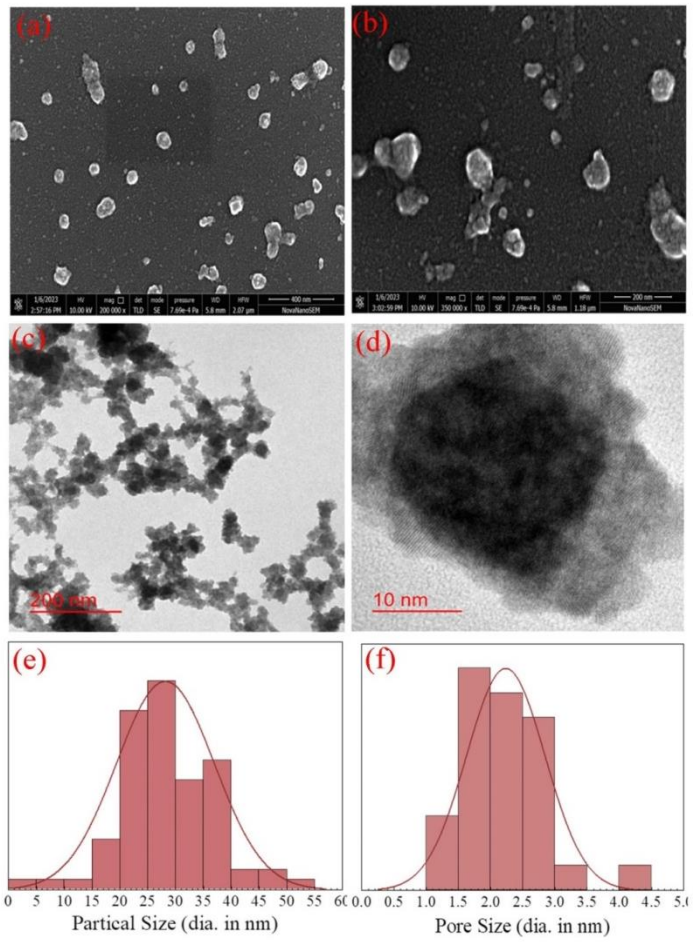

Figure 3.1. 1 Morphology and particle size distribution analysis of p(NAG-b-A) co-polymeric hydrogel. (a)-(b) SEM micrographs, (c-d) HRTEM micrographs, (e) histogram for average particle size distribution obtained from (c) and (d), and (f) the pore size distribution obtained from HRTEM images (Figure 3.1.d).

3.1.3.4. Swelling behavior of p(NAG-b-A) for cellular microenvironment. Hydrogel can provide an excellent microenvironment for differentiating the neuronal cells and the soft hydrogel could provide the mechanical support and physical cue for regenerating the neuron.[35] Further, the swelling of polymeric hydrogel could help in controlling the release of exogenous molecule such as neurotrophic factor, neuronal growth factor and inhibitors.[36] The swelling behavior was evaluated by equilibrating the hydrogel in different pH (such as pH 3, 5, 6, 7.4 and 8) in PBS (Figure 3.1.2a). It is noticed that this hydrogel can expand to a higher extent and

the swelling nature is pH dependent (Figure 3.1.2b-c). The synthesized hydrogel can be swelled up to 1700% (v%) within 90 min of incubation in PBS. Further, it is noticed that with the increase in pH, the swelling ratio has also been increased with a larger extent. However, the highest mass and volume swelling index was observed to be in the order of pH 8 >7.4> 6≥ 3>5, within 90 minutes of incubation in PBS (Figure 3.1.2b-c). Further, the hydrogel was dispersed in water and the size distribution and zeta potential were measured (Figure S3.1.8a-b). From DLS it is found that particle size increased with increase in the incubation time, such as at 120s, d ≈ 141±10^{-6} nm, at 248 secs, d ≈164.2±10^{-6} nm and at 480 sec, d ≈ 725±77 nm; due to the swelling of particle (Fig. S.3.1.8(a)). The minor hump of particles size was observed may be due to the smaller fragment or smaller sizes of parties. From an average zeta potential value (ξ) has been calculated to be -25 (± 4) mV (Figure 3.1. S8(b)). This increase in particle size (hydrodynamic diameter) is obtained from TEM and is due to the swelling of the particles in water. The average particle size of dried p(NAG-b-A) hydrogel (TEM results, Figure 3.1.1e) is compared with the DLS (hydrodynamic diameter of the hydrogel, Figure S3.1.8a) and it is exhibited ~ 25-32 times (2566% –3100%) increased in swelling ratio within 5 minutes of incubation in PBS (at pH 7.4) and these results are well corroborated with the swelling behavior of the hydrogel observed in PBS (Figure 3.1.2). However, the obtained zeta potential result (ξ -25 ± 4 mV) revealed that the hydrogel particles are colloidal stable.

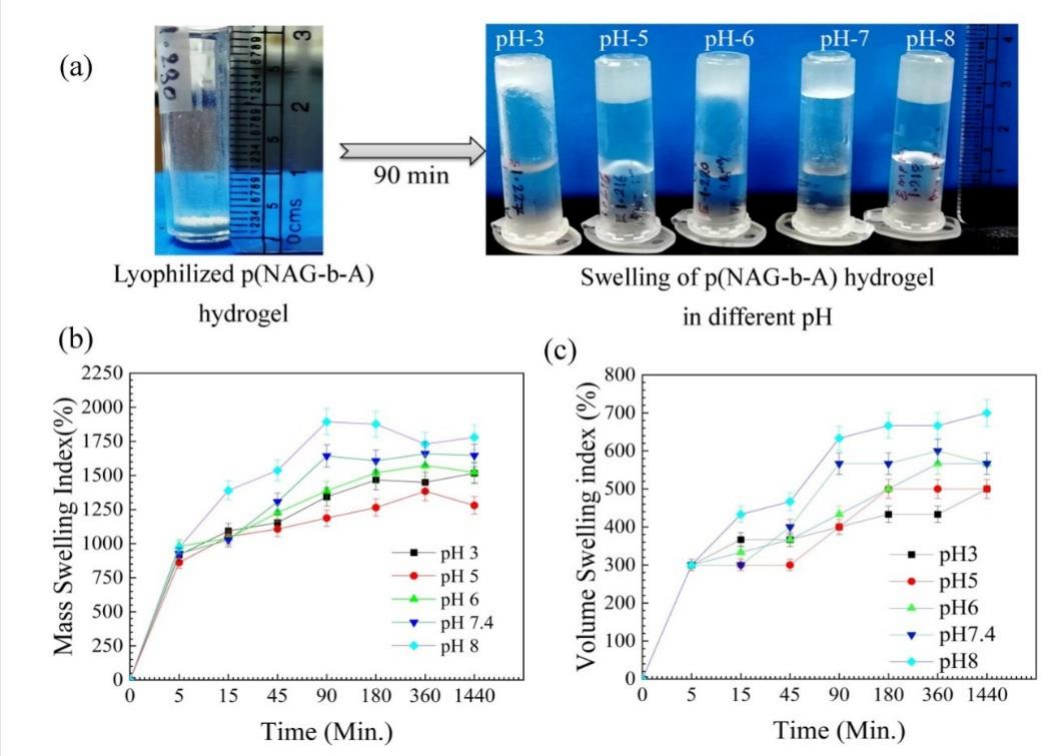

Figure 3.1. 2. Swelling behavior of p(NAG-b-A) co-polymeric hydrogel. (a) Pictorial representation of swelling behavior of hydrogel at different pH of PBS, (b) percentage of mass swelling index at different pH and (c) volume swelling index of hydrogel at different pH.

3.1.3.5. Rheological properties of p(NAG-b-A) hydrogel. Mechanical properties and viscoelastic behavior of polymeric material strongly influence the proliferation and differentiation of neuronal stem cells.[22] Therefore, dynamic rheological behavior of p(NAG-b-A) hydrogel was studied at different physiological temperatures through frequency sweep measurement, The storage modulus (G′), Loss modulus (G″) and complex viscosity (η*) were measured as a function of angular frequency (ω) for p(NAG-b-A) hydrogel and the results are shown in Figures 3.1.3a, 3.1.3b and 3.1.3c, respectively. The steady shear measurements were used to elucidate the flow behavior and molecular network structure of the synthesized hydrogel.[37] At the physiological temperature the storage modulus was found to be varied from 2.9 kPa to 3.7 kPa at 0.1 to 100 rad sec^{-1} (Figure 3.1.3a) and loss modulus was found to be

varied from 2.4 kPa to 2.3 kPa (Figure 3.1.3b). The G′ value decreases with the increase in the temperature (34 to 40 ºC). For the similar reasons, the loss modulus (G″) for the hydrogel varied with change in the temperature and ω. Further, it is noticed that at 37 ℃ the G′ is nearly equal to G″ at 0.15 rad sec^{-1}, which comprises the complex viscoelastic behavior of our hydrogel. Similarly, at 40 ℃ and at lower ω (i.e., ω = 0.1 rad s^{-1}), the crossover point is observed, which comprises to the change in the viscoelastic behavior of the hydrogel due to the change in the swelling index and the inter polymer chain interactions/entanglement effects. The crossover point is related to the molecular architecture and cross-linking behavior of the polymeric hydrogel and the crossover points at low frequency refers to the low molecular weight polymeric structure,[38] which has been confirmed from the mass spectra (Figure S3.1.5). The polymeric hydrogel retains the viscoelastic property as G″ was lower than that of the G′ and this is observed due to the complex behavior of the hydrogel. However, other than 40 ℃ for all other temperatures the G′ and G″ values proportionally increased with increase in ω. It is also observed that with change in the ω, the complex viscosity η* changes and it is temperature dependent (Figure 3.1.3c).[39] Figure 3.1.3(d) shows that the viscosity changes with increase in the shear rate (γ). Figure 3.1.3e shows the decrease in the viscosity in response to the shear rate and in response to time, which refers to the shear thinning behavior (at 34 ℃ and 37 ℃) of the hydrogel. It is further noted that the shear stress vs. shear rate properties of the polymeric hydrogel can also be correlated (Figure 3.1.3f). However, the shear rate decreases with increase in the temperature at all the ω ranges (in the entire experimental region). This phenomenon has appeared due to the molecular motion, grafting and cross-linking of the polymer chains present in the hydrogel.

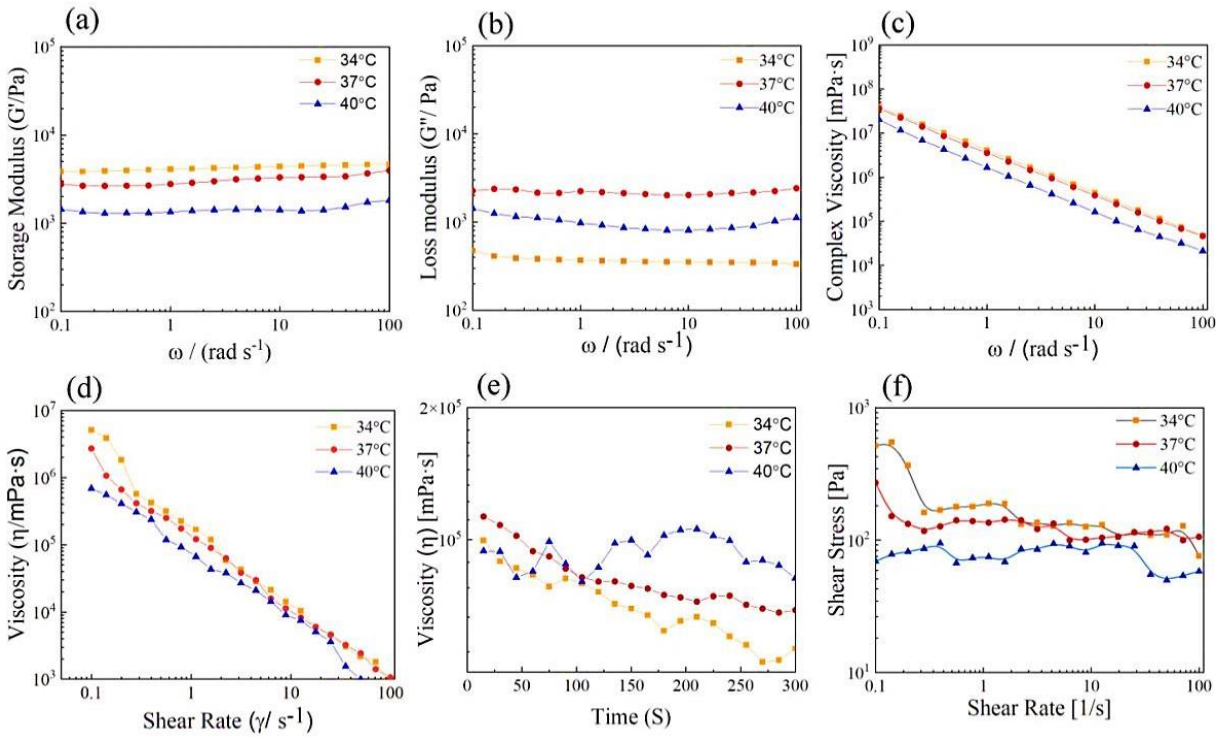

Figure 3.1. 3 Rheological properties of p(NAG-b-A) co-polymeric hydrogel were studied with different conditions. Frequency (ω) sweep measurements of p(NAG-b-A) hydrogel were performed at different temperatures (34 ℃, 37 ℃, 40 ℃ and 43 ℃); (a) storage modulus vs. ω; (b) loss modulus vs. ω, at different temperature; and (c) complex viscosity (η) vs. ω at different temperatures. (d) Viscosity (η) flow behavior of p(NAG-b-A) hydrogel as a function of shear rate (γ); (e) Viscosity (η) as a function of time and temperature and (f) show the change in shear stress with shear rate at different temperatures.*

3.1.3.6. Cytocompatible p(NAG-b-A) hydrogel protects cytoskeletal framework of cortical neurons. The cytocompatibility of p(NAG-b-A) was assessed at different concentrations of hydrogel on various cell lines such as, HEK293 (a human embryonic kidney cell could be transformed in human neuronal lineage cell), HepG2 cells (human hepatoma cells commonly used in drug metabolism and hepatotoxicity assessment studies)[38] and PC12 cells (a type of catecholamine cells, exhibits the feature of mature dopaminergic neuron).[40] In brief, $1x10^4$ cells were seeded in each well of 96 well plate and incubated for 24 h. followed by treatment with different concentrations of hydrogel (e.g., 10, 25, 50, 100,

250, 500 and 1000 μg mL^{-1}) for another 24 h. and the cell viability was calculated by using absorbance taken at λ = 570 nm. Our results showed that the HEK293 cells are cytocompatible upto the concentration of 100 μg mL^{-1} ($p<0.05$) (Figure 3.1.4a). However, above the 250 μg mL^{-1} concentration, HEK293 exhibited that ~ 80% cells are viable. Similarly, HepG2 cells are cytocompatible upto 500 μg mL^{-1} of hydrogel and significantly shows cell proliferation at the concentrations range of 50 to 100 μg mL^{-1} of p(NAG-b-A) (p ~0.03 and 0.02, respectively). However, at relatively higher concentration such as 1000 μg mL^{-1}, the cell viability obtained to be 79% ($p = 0.03$) (Figure 3.1.4a). Interestingly, in PC12 cells, we observed a significant increase in proliferation up to 150% at the concentration of 500 μg mL^{-1} ($p \sim 0.0024$) hydrogel, whereas at 1000 μg mL^{-1} the proliferation observed to be ~ 125% ($p \sim 0.007$). At higher concentration, the reduction in cell proliferation occurred due to the contact inhibition and mechanically generated stress by the swelling of hydrogel (Figure 3.1.4(a)). It is also noted that our finding for the cell viability of PC12 cells in presence of p(NAG-b-A) hydrogel supports our hypothesis for the application of p(NAG-b-A) hydrogel in neuroregenerative applications. Further, to assess the role of this hydrogel in neurogenesis, the primary neuronal cells (1 x 10^6 number) were cultured in the presence of different concentrations of hydrogel on the 12 well plate. Macroscopic images were obtained and the results revealed the increase in cell count with increase in the concentration of hydrogel (Figure 3.1.4b). Further, live and dead assay were performed using acridine orange (AO) and propidium iodide (PI) on the PC12 cell lines (Figure 3.1.4c) by culturing 1 x 10^5 cells on the slide coated with p(NAG-b-A) hydrogel of different concentrations (100 μg and 500 μg) for 5 days. The microscopic images revealed that in the control group the cell population has been decreased due to the apoptotic cell death. While in hydrogel the dead

cells observed are negligible. Thus, it can be concluded that, in p(NAG-b-A) hydrogel the cells remained healthy for longer duration (Figure 3.1.4c). Further to evaluate the cytoskeletal framework, 3 x 10^6 primary neuron cells were seeded in each well of a 48 well plate containing 500 μg of p(NAG-b-A) hydrogel with neuronal media supplemented with B27 and 50 ng of NGF for the differentiation of neuron till the 10^{th} day. After the 10^{th} day, cells were fixed with 4% paraformaldehyde and stained with rhodamine phalloidin, which selectively label the F-actin and nucleus with Hoechst 33258 (Figure S3.1.9). Then fluorescent microscopic images were acquired and it revealed that the p(NAG-b-A) hydrogel promotes cellular proliferation and the healthy network formation of actin filament and confirms very high stability of the cytoskeleton network (Figure S3.1.9) compared to the control sample.

3.1.3.7. Study the p(NAG-b-A) hydrogel assisted neurogenesis. To establish the potential use of p(NAG-b-A) hydrogel in neuronal applications and estimation of *in vitro* axonal regenerative properties, β-tubulin III expression was assessed by Immunolabeling of cells cultured on the surface of the granular hydrogel (500 μg mL^{-1} granular nanohydrogel coated slide) and on 1 mm thick film of p(NAG-b-A) hydrogel. 1 mm thin film is generated by following polymerization step for lesser time of 4 h compared to the steps mentioned in method and followed by pouring onto the glass petri plate. Then poured hydrogel is air-dried and washed repeatedly with water:ethanol (1:1) to remove impurities if any. To obtain the granular p(NAG-b-A) hydrogel, the polymerization step was continued till the end of the reaction as mentioned in the method section and subsequently washed with water:ethanol (1:1) followed by the lyophilization. Further, 500 μg mL^{-1} of granular nano hydrogel was suspended in 1X HBSS and smeared onto the cover slip followed by UV sterilization of film

and coated granular hydrogel. Further, the isolated hippocampal neurons (1 x 10^6) were seeded on the 500 µg mL^{-1} granular nanohydrogel coated slide p(NAG-b-A)(A-group), p(NAG-b-A) hydrogel film (B-group) and poly(L-lysine) coated cover slip (control creates the hydrophilic surface, which further facilitates the kinetics of neuronal adhesion[41] with supplemented media (neurobasal media + 10% FBS + 50 ng NGF + antibiotic).

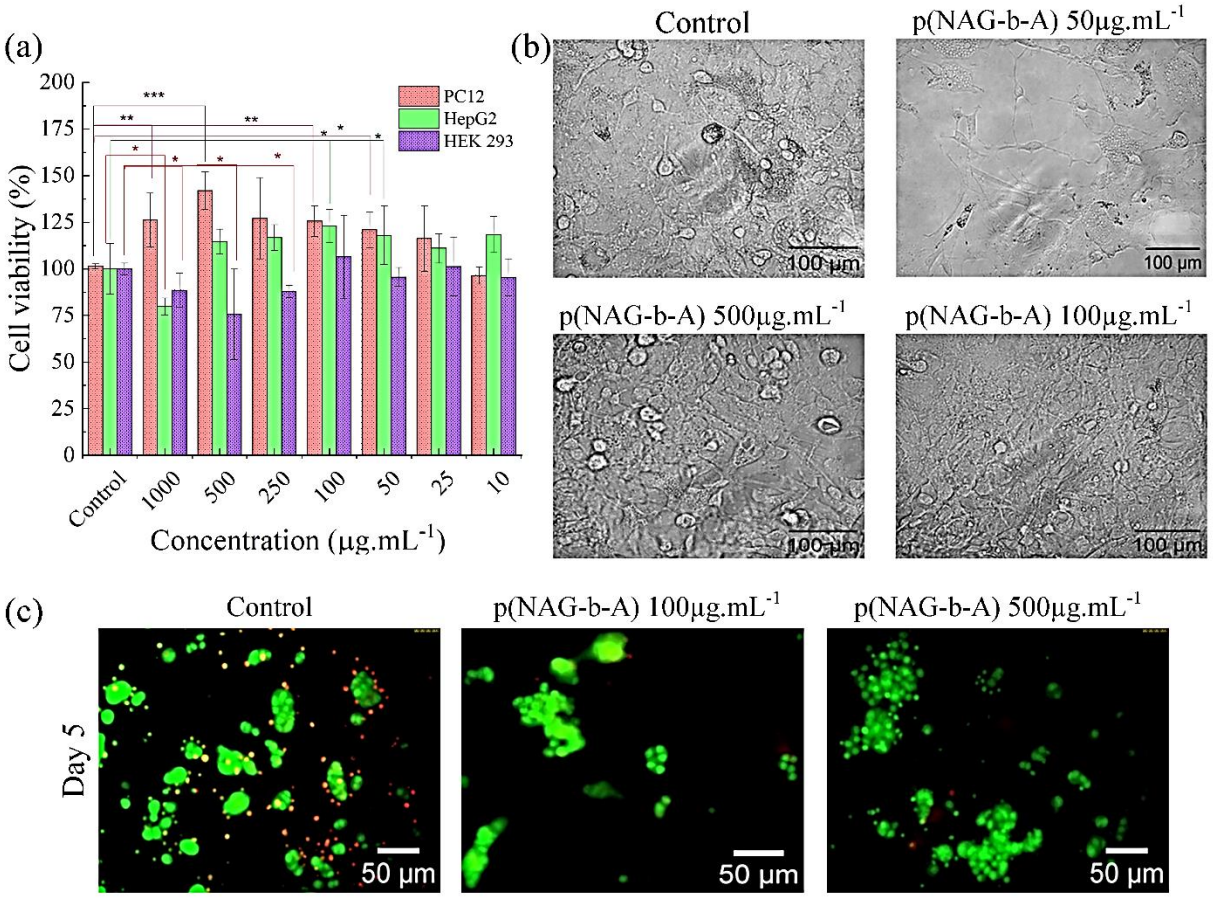

Figure 3.1. 4. Cytocompatibility and neurotoxicity results of p(NAG-b-A) co-polymeric hydrogel. (a) Show the cell viability results on HEK293, HepG2, and PC12 cells at different concentrations of p(NAG-b-A) hydrogel. (b) Shows the primary neuron differentiation in control and with different concentrations of hydrogel (50, 100 and 500 µg mL^{-1}). (c) Acridine orange and PI staining of PC12 cells grown on the control and p(NAG-b-a) hydrogel of concentration 100 µg mL^{-1} and 500 µg mL^{-1} concentration on 5^{th} day.

Further, cells were cultured for specified time interval and after proper Immunolabeling high-resolution confocal microscopy images were acquired on the 2nd (Figure 3.1.5a), 7th (Figure 3.1.5b)) and 14th day (Figure 3.1.5c and Figure S3.1.10) and analyzed using the FIJI software.[27] For this study, matrigel and laminin can also be used, however we limited our study to poly(L-lysine) coating for the control group and we obtained comparatively exciting results. Further, β-tubulin III expression was compared with control and treated groups by acquiring confocal images. The β-tubulin III specially localized in neuron and its heterodimer assembly forms the microtubule network and decrease β-tubulin III expression correlated with impaired axonal elongation.[42] The β-tubulin III is required for the formation of nervous system, however it has the specific role in peripheral axon regeneration.[43] Therefore, further analysis was conducted by using the microscopic images. The confocal microscopy results revealed that on 2nd day, primary neuronal cells have established the adhesion and the cell-cell association along with initial differentiation of neuronal cells in all control group, in p(NAG-b-A) (A-group) and p(NAG-b-A) (B-group) samples (Figure 3.1.5 and Figure S3.1.10). It is clearly evident that the cell population increased significantly with higher extent of p(NAG-b-A) (A group) ($p = 0.04$) used, whereas in control and p(NAG-b-A) (B-group) the cell population differences were found to be negligible. On the 7th day, substantially decrease in the cellular proliferation and increase in neuronal differentiation were statistically significant with increase in the number of junction points. In control group, p(NAG-b-A) (A-group) and p(NAG-b-A) (B-group) samples, the cellular proliferation and increased differentiation were statistically significant and difference in neurite length (green signal) are shown in (Figure 3.1.5) and (Figure S3.1.10). However, in the control group samples, mostly unipolar neuronal growth

was observed. Further, in both the p(NAG-b-A) (A-group) and (B-group) hydrogel samples, most of the neurons are found bipolar and pyramidal in nature with thicker axon and their number of junctions were also significantly increased ($p \sim 0.04$ and $p \sim 0.03$, respectively) with low signal of F-actin as shown in Figure 3.1.5. On 14th day, the cell population decreased in all control samples and in both A-group and B-group) (Figure 3.1.5d). It is further noticed that the density of the network structure also substantially increased (Figure S3.1.5b and 3.1.5c). The f-actin signal is increased with the healthy network structure of the neuron on 14th day (Figure 3.1.5c) with respect to the 7th day (Figure 3.1.5b). Similarly, longest axonal growth is observed in p(NAG-b-A) (A-group) compared to the p(NAG-b-A) (B-group) and for the control samples (Figure 3.1.5e). The differences in axonal growth in all the samples are found to be statistically significant. Further, it is observed that number of junctions formed on the 14th day are more in the control group of samples as compared to the 7th day (Figure 3.1.5f), whereas a negligible difference is observed in p(NAG-b-A) (A-group) sample. However, the numbers of junctions are found to be increased in p(NAG-b-A) (B-group) ($p \sim 0.03$), which means that the deep penetration of axons in hydrogel occurred resulting in increase in the numbers of branches. Similarly, on the 14th day, a high density neuronal network has been formed, which looks like the structure of astrocytes (Figures S3.1.10 a-f).[44] Further, a higher signal for f-actin surrounding the nucleus is observed, which evident for the formation of the dendrites (Figure S3.1.10c). Thus, the confocal microscopy results concluded that the p(NAG-b-A) hydrogel stimulates the stabilization of neuronal network with increasing the axonal regeneration property. The Z-stack projected images of neurons on p(NAG-b-A) (A-group) shown in Figure S3.1.10 (a-f) is found to be 8 μm in thickness,

while for the p(NAG-b-A) (B-group) it is found to be 28 μm in thickness. All these results supported that the neurons/axons penetrated more in the swelled hydrogel film (Figure S3.1.10g-l). Interestingly, on 14th day the treatment group neurons observed Purkinje neuron-like projections[45] as it is shown in Figure S3.1.10(d). It is known that Purkinje neuron cells play critical roles for proper cerebral functions and a major role in the transmission of electrical signals with propagation of impulsive signals to the various ventricular muscles.[46,47, 49]

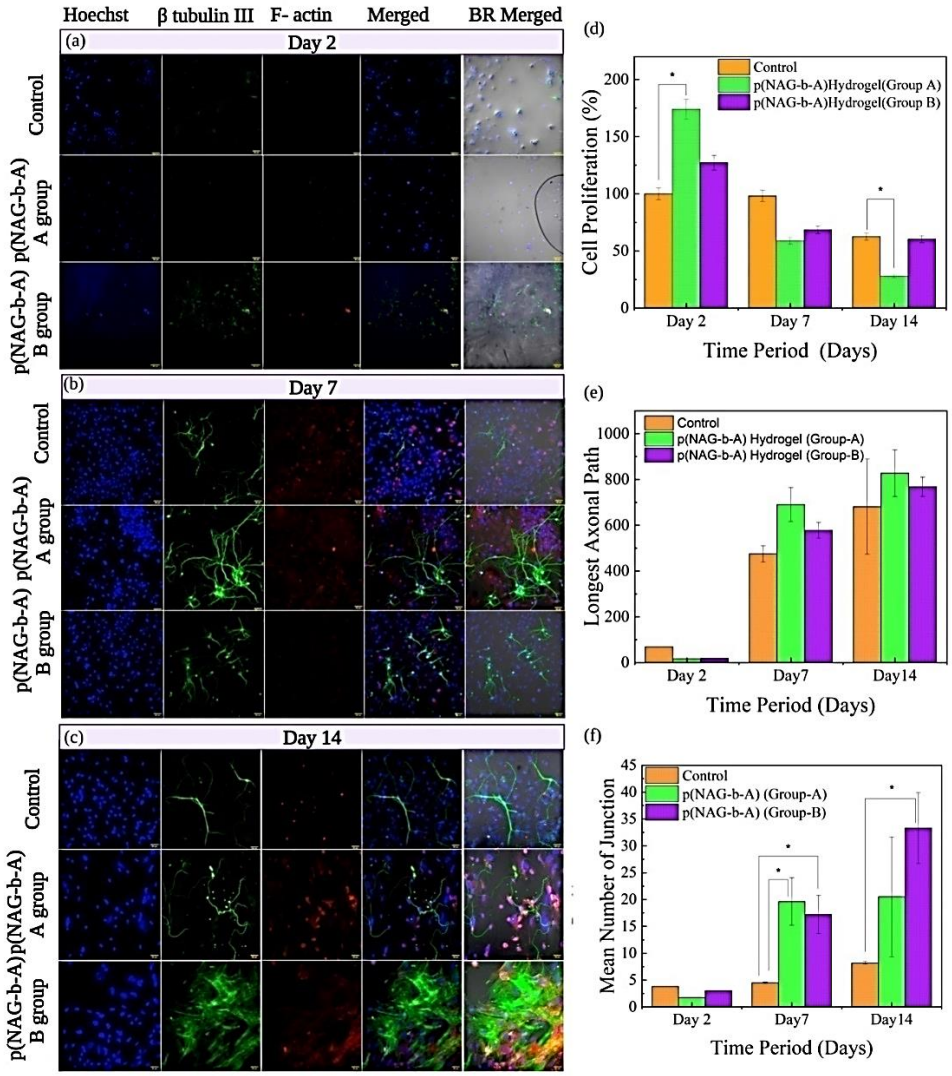

Figure 3.1. 5 Confocal microscopy images represent the neuronal growth on p(NAG-b-A) co-polymeric hydrogel: 500 μg mL^{-1} granular nanohydrogel coated slide (p(NAG-b-A), A-group),

p(NAG-b-A) hydrogel film (p(NAG-b-A), B-group) and control (poly(L-lysine) coated slide) till the 14th day. (a) Cellular adhesion and growth on 2nd day, (b) cellular differentiation and neurite extension on 7th day and (c) cellular differentiation and neurite extension on 14th day, (d) cellular proliferation (%) obtained from images. (e) Shows how the longest axonal path varied at different time periods, and (f) shows the increase in number of junctions (branching in neurons) at different time periods. Hoechst 33258 (blue) stains represent the nucleus, immune labeled β-Tubulin III (green) shows neurite extension and immune labeled with phalloidin (red) showed the F-actin (all the Confocal microscopy images captured in 20X).

3.1.3.8. Molecular interaction between polymer and GSK3β. Further to establish the mechanism, how the p(NAG-b-A) hydrogel is involved in neurogenesis, protein ligand interaction studies were performed through *in silico* approach. Among several molecular circuits, GSK3β is considered as a potential target in neurodegenerative therapy due to its wide expression in adult neuron, regulated by PI3K –AKT, and it leads to the increased ratio of active/inactive GSK3.[11] In adult neuron, mTOR signaling requires for the outgrowth, which is regulated by PI3K-AKT signal.[10] The inhibition of GSK3β leads to the activation of PI3K at the distal tip of the neuron and it helps in neuronal regeneration.[10] Majority of the kinase inhibitors show the affinity towards the ATP pocket of the GSK3β protein (PDBID-1Q5K). In the molecular structure of 1Q5K, the ATP pocket present at the interface of β-strand domain at N-terminal residues 25-138 and 139-343 regions, which are boarded by the glycine rich hinge regions.[11] Inhibitor TMU is a co-crystalize structure that is obtained with 1Q5K bounded in ATP pocket and shows the interactions with LEU132 and ARG141. In the GSK3β structure, ASP133 and VAl135 are the predominant and important residues, where a diverse range of inhibitors gets bound. Similarly, ARG96, ARG180 and LYS205 are the crucial residue for the priming substrate.[48] As per our obtained results, the reference molecule TMU has formed 6 hydrogen bonds. The selective inhibitor SB415286[49] interacted by forming 5 hydrogen bonds at one conformation, while in another conformation it has formed 3 hydrogen

bonds and potent inhibitor SB216763[50] formed two hydrogen bands at ATP pocket with almost similar binding energy from -6.9 to 8 kcal mol^{-1} at inhibitor constant of K_i = 7.48 μM to 1.37 μM along with hydrophobic interacting residue as provided in Table S1 and Figure 3.1.6. Further, we observed that NAG (G) and its polymeric unit (dimer and trimer) established the protein ligand interactions with ATP pockets of GSK3β with a higher binding energy at nanomolar (nM) concentration compared to the available inhibitors in micromolar (μM) concentration. With the modulation of glycine (Table S2) to n-acryloylglycine (Figure 3.1.7(a)), the binding energy was increased from -3 kcal mol^{-1} (K_i = 6.33 mM) to -4.74 kcal mol^{-1} (K_i = 338.04 μM), respectively. While for the repetitive units of N-acryloylglycine the significant increase in the binding affinity of GG (Figure 3.1.7b) is calculated to be -11.26 $kcal.mol^{-1}$ (K_i = 5.58 nM) with forming 2 hydrogen bonds and for GGG (Figure 3.1.7e) it is calculated to be -12.62 kcal mol^{-1} (K_i = 512.32 pM) and mostly hydrophobic interactions occurred compared to the reference inhibitor. GGG unit has formed the strongest interaction with the LEU153HN and LEU250-O residues. While in another conformation, it has interacted with the Val135 moiety. Further, we have checked the protein interactions with acrylamide dimer (Figure 3.1.7d) shows only hydrophobic interactions with Val135 (Ki = 1.19 mM) with binding affinity of -3.99 kcal mol^{-1} and heterodimer of NAG and N-acrylamide shows interaction with one hydrogen bond at HIS 106 along with increased binding affinity of -8.45 -3.99 kcal mol^{-1} at very low Ki of 644.27 nM (Figure 3.1.7c). Similarly, Heteromers (three mer units, i.e., AAG) (Figure 3.1.7h) has interacted with the ASP95 with binding affinity of -6.79 kcal mol^{-1} at K_i = 10.56 μM and with VAL135 at K_i = 11.83 μM. Interestingly, with increase in the G units, i.e., AGG (Figure 3.1.7f) and GAG (Figure 3.1.7g), an increase in the binding affinity of trimer is observed. Such as, AGG has interacted at K_i = 148.61 nM with interacting

residue LEU112 with a binding energy of -9.31 kcal mol^{-1}. In another conformation, it interacted at K_i = 405.69 nM with Val135 residues with binding affinity of -8.72 kcal mol^{-1}. The GAG trimer requires a higher value of K_i = 8.73 nM and binding energy of -10.99 kcal mol^{-1} to bind with the Leu112 residues. As a conclusion, with increase in the n-acryloylglycine (G) units into polymeric moiety, it increases the binding efficiency/affinity of polymer hydrogel to the GSK3β, which is further responsible for the neurite outer growth.

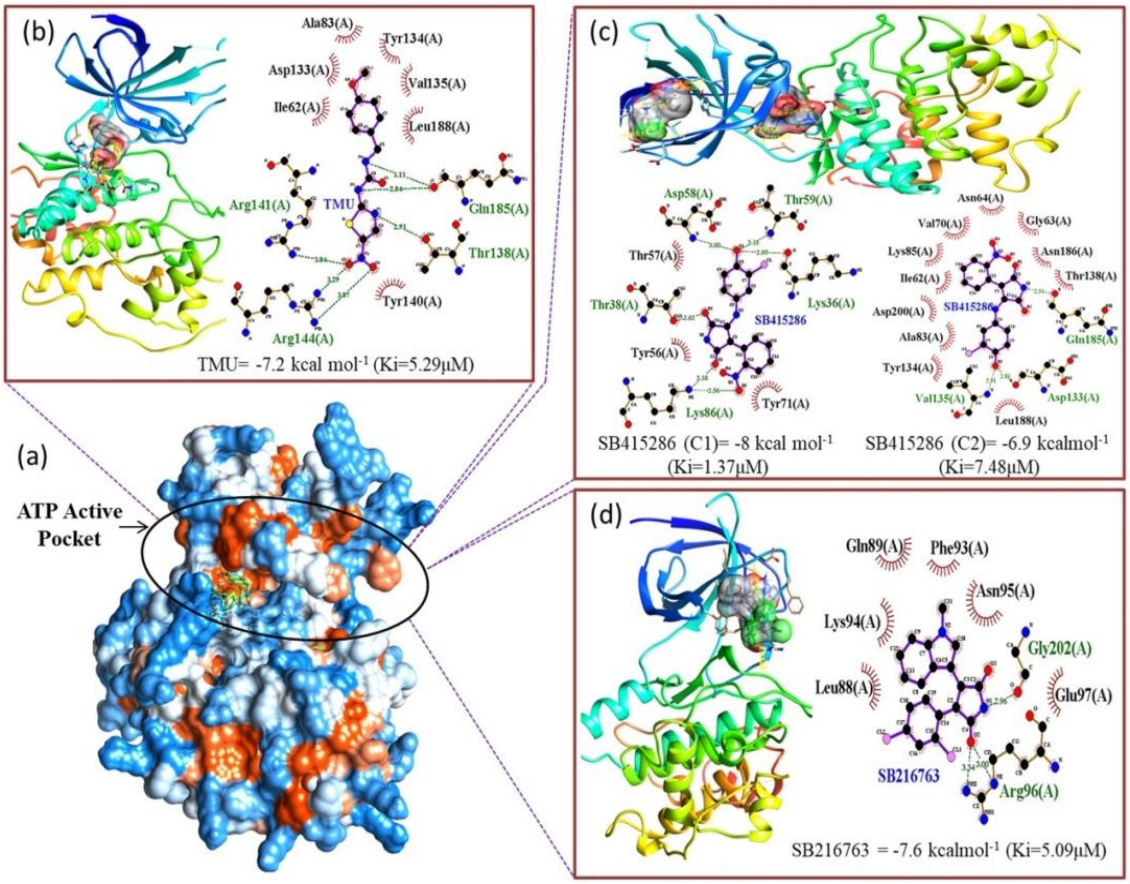

Figure 3.1. 6 Molecular interactions between GSK3β (PDBID-1Q5K) with reference inhibitors. (a) Surface structure shows the ATP binding pockets with TMU inhibitor, (b) ribbon conformation of 1Q5K with N-(4-methoxybenzyl)-N'-(5-nitro-1,3-thiazol-2-yl) urea (TMU) and ligplot shows the interacted residues, (c) ribbon conformation of 1Q5K-SB415286 and ligplot shows the interacted residues with two different pockets and (d) ribbon conformation of 1Q5K-SB216763 and ligplot shows the interacted residues of amino acid with highest binding energy in kcal mol^{-1} and K_i (inhibition constant).

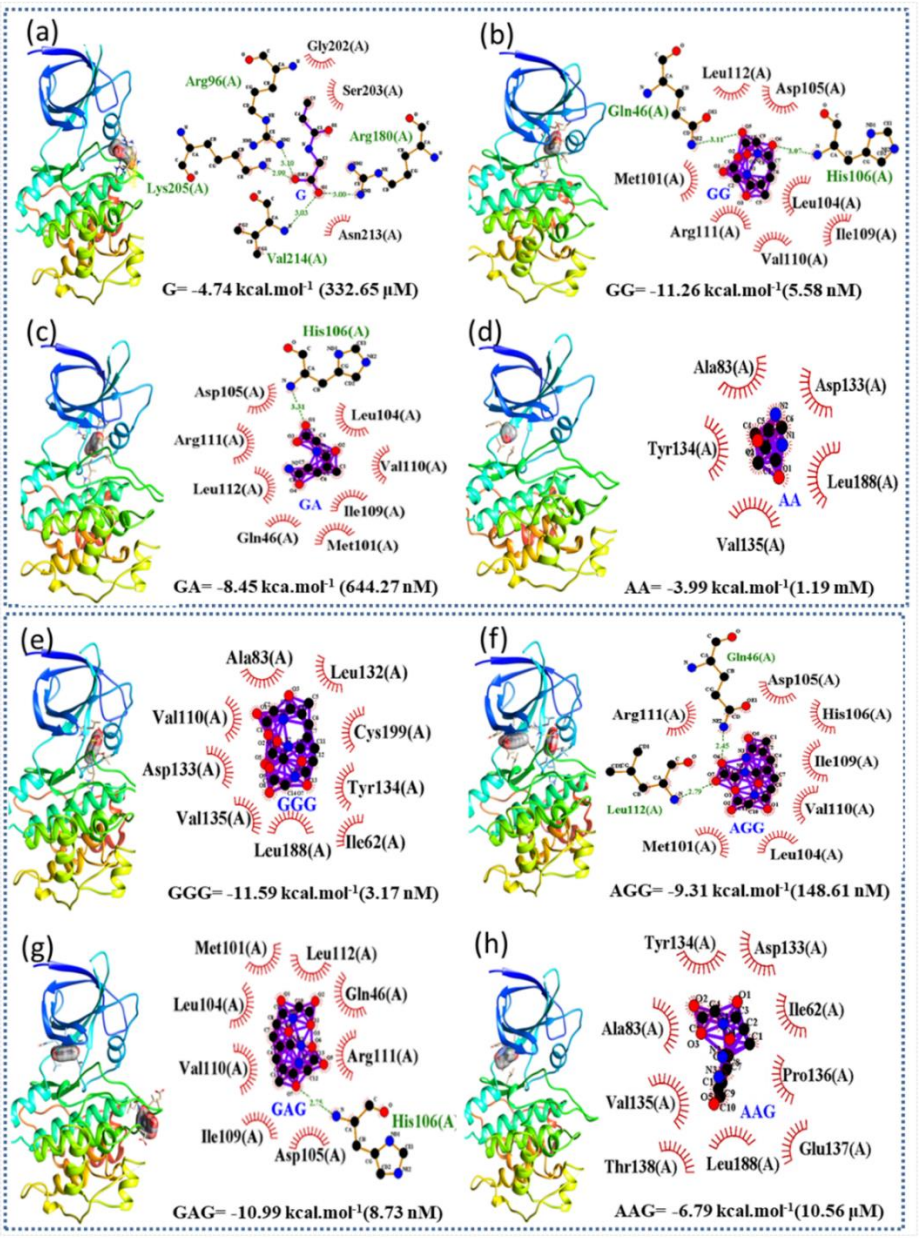

Figure 3.1. 7. Molecular interactions between GSK3β (PDBID-1Q5K) with different monomeric di-units (a-d) and tri-units ((e)-(h)) of poly (N-acryloylglycine-acrylamide). N-acryloylglycine represented as (G) and N-acrylamide represented as (A), (a) 1Q5K- N-acryloylglycine, (b) 1Q5K-GG (N-acryloylglycine di-unit), (c) 1Q5K-GA (N-acryloylglycine-acrylamide di-unit), (d) 1Q5K-AA (acrylamide di-unit), (e) 1Q5K-GGG (homomeric tri-unit of N-acryloylglycine), (f) 1Q5K-AGG (tri-unit of N-acryloylglycine and N-acrylamide), (g) 1Q5K-GAG (tri-unit of N-acryloylglycine and N-acrylamide), and (h) 1Q5K-AAG (triunit of N-acryloylglycine and acrylamide). Ribbon structure shows the docking site between 1Q5K and ligplot with each structure showing the interacted residue along with binding energy in kcal mol^{-1} and inhibition constants (K_i) in mM or µM or pM.

3.1.3.9. Protective role of p(NAG-b-A) in oxidative stress. In order to elucidate the applicability of p(NAG-b-A) hydrogel in clinical settings, PC12 cells were grown in the presence of oxidative stress that was generated by H_2O_2 and treated with the p(NAG-b-A) hydrogel. It is known that neuronal cells are vulnerable to oxidative damage. Imbalance between generation of free radicals and antioxidant defense often lead to oxidative stress followed by the neuropathological conditions.[25] For a proof of concept, PC12 cells were treated with different concentrations of H_2O_2 from 5 μM to 160 μM in the presence and absence of 500 μg mL^{-1} of p(NAG-b-A) hydrogel (Figure 3.1.8a) and we observed that almost 70%, 61% , 69% , 62% , 71% and 82% dead cells with respective concentration of H_2O_2. However, in presence of 500 μg mL^{-1} p(NAG-b-A) hydrogel almost minimal 10% to maximum 30% cell viability was increased in all different concentrations of H_2O_2 treated group which corroborates the protective behavior of p(NAG-b-A) hydrogel as shown in Figure 3.1.8a. Further, to check the recovery of damaged PC12 cells, they were initially treated with different concentrations of H_2O_2 for 24 h, and then the H_2O_2 containing media was replaced with fresh complete media and then treated with 500 μg mL^{-1} p(NAG-b-A) hydrogel (treated group) and only media containing without 500 μg mL^{-1} p(NAG-b-A) hydrogel (stress group). Interestingly, we did not observe any increase in cell viability (i.e., viability is almost 8 to 10%). However, in 500 μg mL^{-1} p(NAG-b-A) hydrogel treated group the cell viability was increased from 8% to 39.28% as the treatment concentrations of H_2O_2 maintained from 160 μM to 5 μM (Figure 3.1.8b). These findings are interesting evidence that our p(NAG-b-A) hydrogel promotes the recovery of damaged PC12 cells. Similarly, the status of the recovery for the AO/EtBr staining untreated PC12 cells, treated only with H_2O_2 (40 μM) and H_2O_2 (40 μM) with 500 μg mL^{-1} p(NAG-b-A)

treated PC12 cells was investigated. It is observed that the treatment with 500 μg. mL^{-1} p(NAG-b-A) prolongs the healthy cell viability and reduces the apoptotic death as shown in Figure 3.1.8(d). Further, confocal microscopic images revealed that treatment with H_2O_2 (40 μM) causes the nuclear damage along with destabilization of cytoskeleton network (H_2O_2 treatment on PC12 shows reduced red signal of f-actin) and with axonal terminal damage (Figure 3.1.8(e)). These damages were prevented by using 500 μg mL^{-1} of p(NAG-b-A) hydrogel treatment, which shows the intact nuclear structure with increased signal for F-actin and thicker axon growth (green signal for β-tubulin III). We hypothesized that this protective behavior of p(NAG-b-A) hydrogel could be obtained due to the neutralization of ȮH radicals by the ─NH and ─COOH groups of p(NAG-b-A) hydrogel. To establish this fact, further the hydrogel was treated with H_2O_2 (40 μM) for 24 h, and subsequently FTIR and Raman spectroscopy analysis were performed and the possible roles of these functional groups during the neuroprotection has been proven. FTIR spectrum of H_2O_2 treated p(NAG-b-A) hydrogel clearly revealed the diminished of the ─C═O (1734 cm^{-1}) and alkane (2923 cm^{-1}) bands. Further, from the Raman spectroscopic analysis (Figure 3.1.8(c)) the common bands in untreated p(NAG-b-A) hydrogel and H_2O_2 treated p(NAG-b-A) hydrogel, i.e., 1078 cm^{-1} and 1090 cm^{-1} (C─N of amide or protein or due bending vibration of CH), 1404 cm^{-1} and 1398 cm^{-1} (CH_3 umbrella mode), 2937 cm^{-1} and 2937 cm^{-1} (alkane), and 3142 cm^{-1} and 3239 cm^{-1} (─NH), respectively have been identified. However, in H_2O_2 treated hydrogel an additional Raman band has been observed at 1622 cm^{-1} due to the presence of amide bonds (─C=O mixed with ─NH deformation). This observation shows that when polymer comes in contact with H_2O_2, it triggers the release of CO_2 and H_2O molecules as by-products. It is further noticed that few FTIR bands

disappeared after the treatment with H_2O_2, which may have occurred due to the degradation of the polymer. Detailed investigations are required to completely understand the mechanism of actions that is being planned for future studies. Thus, it can be concluded that the p(NAG-b-A) hydrogel possesses a strong protective role for the living cells in oxidative stress conditions.

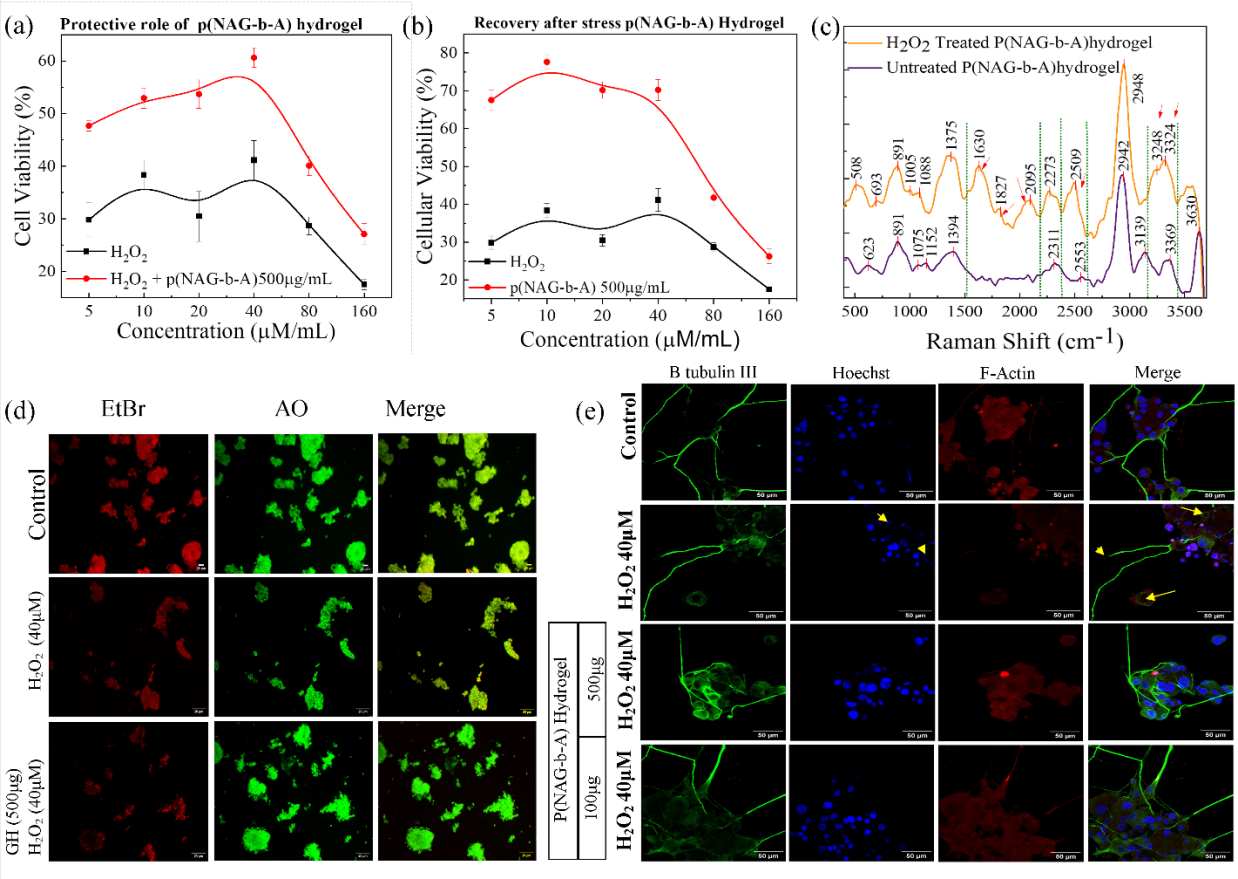

Figure 3.1. 8 Protective role and recovery status after H_2O_2 induce oxidative stress associated damage assisted by p(NAG-b-A) hydrogel. (a) Protective role of p(NAG-b-A) hydrogel obtained by cell viability assay, (b) stress induced recovery status of PC12 cells using p(NAG-Ac-NAE) hydrogel, (c) Raman shifting of p(NAG-Ac-NAE) hydrogel, (d) AO/EtBr staining of PC12 cells untreated control, treated with H_2O_2 (40 μM), and treated with 40 μM H_2O_2 along with 500 μg mL^{-1} of p(NAG-b-A) hydrogel and (e) cytoskeleton network stabilization by p(NAG-b-A) hydrogel in the presence of 40 μM H_2O_2 induced oxidative stress at highest proliferative concentration of 500 μg mL^{-1} hydrogel.

3.1.4. DISCUSSION

In the recent arena, polymeric hydrogel is considered as the potential drug delivery platform for the management of neurological conditions due to the high drug loading capacity, good permeability, high colloidal stability and which could bypass the physiological barrier (BBB). Glycine is an inhibitory neurotransmitter and takes part in early neurogenesis/neuroprotective activity. Therefore, glycine based polymeric hydrogel could boost the neurogenesis/neuroprotective activities. In the present work, glycine based p(NAG-b-A) hydrogel particles were synthesized (d ≈ 25-40 nm in diameter) (Figure 3.1.1). Void space of hydrogel network structure limits the cell infiltration. However, it can be overcome by heterogeneous granular hydrogel formation as the pore sizes are proportional to the assembling into micron sized particle that is useful for the cellular infiltration.[51] Synthesized p(NAG-b-A) hydrogel exhibits very high swelling behavior (~1500%) (Figure 3.1.2) within 12 h. However, the major limitation of the cross-linked polymer hydrogel is that it is not solubility or partially soluble in organic solvents and measuring molecular weight is very difficult.

In leading pathophysiological condition, change in the intracellular pH in neuron correlated with the neurodegenerative diseases, brain acidosis mediates the neuronal death, AD, HD and PD and the cerebral alkalosis leads to the ischemic stroke,[52,53] N-acyloylation of amino acid could favor the development of pendent polymer and the charge distribution in a stereo-selective configuration along with higher gelling property.[15,16] Due to the presence of carboxylic acid groups (─COOH) and amide groups (─CONH─) in N-acryloyl based polymeric chains (Figure S3.1.1-S3.1.3), it exhibits pH and temperature responsive behaviors in aqueous medium. Hence, it could be a good candidate for the loading of various therapeutic molecules (Figure 3.1.1(a)) and useful in various brain physio-pathological conditions and for

neurite growth. The p(NAG-b-A) nanohydrogel is quite stable between 30 ℃ to 200 ℃ (Figure S3.1.6). In the biological system p(NAG-b-A) nanohydrogel could show biodegradable behavior due to the presence of N-acryloyl glycine as a monomeric unit. Glycine N-acyltransferase produce a minor metabolite of fatty acids and the degradation of acyloylglycine through hydrolysis can produce the glycine.[54] The semi crystallinity of p(NAG-b-A) (Figure 3.1.1d and Figure S3.1.7b) allows mechanical stability and the high surface zeta potential of p(NAG-b-A) (-25mV) has established its colloidal stability in aqueous medium (Figure S3.1.8b). The shear thinning behavior of this hydrogel (Figure 3.1.3(e)) has increased the inject-ability and contributed in enhancing the mixability, pumpability and pourability.[55] Further, it has been reported that in soma (softest part) and neurite micro-compartment (stiffer part), it shows different mechanical responses i.e., young modulus values obtained to be of 1.05 kPa to 0.38 kPa and 7 kPa, respectively which is very important for the neuroregeneration.[56] With different range of elastic moduli, neuronal cell behaves differently like below 1 kPa (softer surface) moduli favored the neuronal differentiation and above 7 kPa (stiffer surface) moduli favor oligodendrocytes differentiation, between 1 kPa - 3 kPa moduli shows the astrocytes differentiation[57] and modulus of 2 kPa can increase the differentiation of immature to mature neurons.[58] p(NAG-b-A) hydrogel shows the elastic modulus value of 2.9 kPa to 3.7 kPa, which favors the differentiation of immature to mature neurons and promotes the astrocyte differentiation (Figure S3.1.10(a-f)). Along with the cytocompatibility, p(NAG-b-A) nano-hydrogel promotes the proliferation of the HepG2 and PC12 cell lines in high extent (Figure 3.1.4a and 3.1.4b). Similarly, in primary neuron culture it is observed that the p(NAG-b-A) hydrogel can induce an excellent neurite growth along with the microtubule stabilization which is possible due to the granular network formation capability of the hydrogel with 3D

cellular infiltration (Figure 3.1.5(a-c) (pNAG-b-A) group B). Deep penetration of cells (Figure 3.1.5e) into the hydrogel and the porous nature of hydrogel film provided the highest nutrient to the cells and helped to mimic the neuronal microenvironment. Strong signal of Rhodamine phalloidin for F-actin exhibited that the p(NAG-b-A) promotes the neuronal integrity (Figure 3.1.5(a-b)) along with development of dendrites and spine penetration (in Figure 3.1.5(a-c) and Figure S3.1.10).[59] additionally, the axonal elongation is confirmed through the β-tubulin III (green) expression. Inactivation of GSK3β promote the axon regeneration by increasing the microtubule growth speed in the growth cone.[60] As GSK3β mediates the phosphorylation of several proteins and involves in various signaling pathway like GSK3β-CRMP-2 axonal growth inhibitory pathway,[60] PI3K-AKT pathway[61] and Akt/GSK-3β/β-catenin and overexpression of GSK3β have correlation with several neurological disorders.[62] *In silico* study suggests that the polymeric unit interacted with GSK3β at ATP active pocket with higher binding efficiency comparable with the available inhibitors (Figure 3.1.6a and Figures 3.1.7a-h). Further, it suggests that the neurogenesis could occur due to the GSK3β inhibition.

Accumulation of reactive oxygen species followed by lipid peroxidation and mitochondrial dysfunction. As a consequence, neuronal death and persistent oxidative stress leads to the neurodegenerative diseases.[63,64] As per our observation, it can be concluded that the presence of free radicals in stress conditions may cause the oxidation of p(NAG-b-A) hydrogel. These free radicals can attack to ─C=O bond of polymer and can oxidize the p(NAG-b-A) and can release CO_2 and water as byproducts. Further the conversion of secondary amine is primary amine is occurred due to the attack of $OH^{\cdot}$ radical which has been confirmed from the FTIR band shifting from 1658 cm^{-1} (pNAG-b-A) to 1637 cm^{-1} (H_2O_2 treated p(NAG-b-A)) (Figure S3.1.11). This interaction of ROS and stimulatory effect on astrocyte assists the

neuroprotective role.[65]. Further, controlled synthesis and purification of (pNAG-b-A) hydrogel with different molecular weights can provide the clear insight about the neurogenesis and neuroprotection efficacy of the hydrogel.

3.2.5 SUMMARY and CONCLUSIONS

In this work, we have successfully synthesized porous, cross-linked p(NAG-b-A) hydrogel with high swelling behaviour. The p(NAG-b-A) shows shear thing behavior and injectable in nature. p(NAG-b-A) can promote the axon growth in primary neuron and can improve the microtubule integrity. However, its exact mechanism is yet to be found out. *In silico* study reveals that the p(NAG-b-A) hydrogel could be involved in the GSK3β inhibition and promotes neuronal growth via modulating the GSK pathway. Presence of various functional groups such as –COOH and amide group in p(NAG-b-A) hydrogel scavenge the free radicals via oxidation reaction and protect neuronal damage from the oxidative stress conditions. It is found that the viscoelastic nature of p(NAG-b-A) hydrogel favor astrocyte differentiation and consequently neuroprotection. Finally, it can be concluded that the p(NAG-b-A) hydrogel is a potential candidate to induce neuronal regeneration and can be used in other regenerative purposes. Furthermore, (pNAG-b-A) hydrogel can provide a huge scope to analyze the mechanistic activities for the various leading neurodegenerative diseases which could be the future direction of this work.

3.2.6. REFERENCES

(1) Serger, E.; Luengo-Gutierrez, L.; Chadwick, J. S.; Kong, G.; Zhou, L.; Crawford, G.; Danzi, M. C.; Myridakis, A.; Brandis, A.; Bello, A. T.; Müller, F.; Sanchez-Vassopoulos, A.; De Virgiliis, F.; Liddell, P.; Dumas, M. E.; Strid, J.; Mani, S.; Dodd, D.; Di Giovanni, S. The gut metabolite indole-3 propionate promotes nerve regeneration and repair. *Nature* **2022**, *607* (7919), 585-592. DOI: 10.1038/s41586-022-04884-x.

(2) Liu, Y.; Hsu, S. H. Biomaterials and neural regeneration. *Neural regeneration research* **2020**, *15* (7), 1243-1244. DOI: 10.4103/1673-5374.272573 From NLM.

(3) Scheib, J.; Höke, A. Advances in peripheral nerve regeneration. *Nature Reviews Neurology* **2013**, *9* (12), 668-676. DOI: 10.1038/nrneurol.2013.227.

(4) Ruediger, T.; Bolz, J. Neurotransmitters and the development of neuronal circuits. *Axon growth and guidance* **2007**, 104-114. DOI: DOI: 10.1007/978-0-387-76715-4_8.

(5) Hansen, J. Y.; Shafiei, G.; Markello, R. D.; Smart, K.; Cox, S. M. L.; Nørgaard, M.; Beliveau, V.; Wu, Y.; Gallezot, J.-D.; Aumont, É.; Servaes, S.; Scala, S. G.; DuBois, J. M.; Wainstein, G.; Bezgin, G.; Funck, T.; Schmitz, T. W.; Spreng, R. N.; Galovic, M.; Koepp, M. J.; Duncan, J. S.; Coles, J. P.; Fryer, T. D.; Aigbirhio, F. I.; McGinnity, C. J.; Hammers, A.; Soucy, J.-P.; Baillet, S.; Guimond, S.; Hietala, J.; Bedard, M.-A.; Leyton, M.; Kobayashi, E.; Rosa-Neto, P.; Ganz, M.; Knudsen, G. M.; Palomero-Gallagher, N.; Shine, J. M.; Carson, R. E.; Tuominen, L.; Dagher, A.; Misic, B. Mapping neurotransmitter systems to the structural and functional organization of the human neocortex. *Nature Neuroscience* **2022**, *25* (11), 1569-1581. DOI: 10.1038/s41593-022-01186-3.

(6) Bekri, A.; Drapeau, P. Glycine promotes the survival of a subpopulation of neural stem cells. *Frontiers in Cell and Developmental Biology* **2018**, *6*, 68. DOI: 10.3389/fcell.2018.00068.

(7) Eric Samarut1, A. B. a. P. D. Transcriptomic Analysis of Purified Embryonic Neural Stem Cells from Zebrafish Embryos Reveals Signaling Pathways Involved in Glycine-Dependent Neurogenesis. *Frontiers in Molecular Neuroscience* **2016**, *9* (22). DOI: 10.3389/fnmol.2016.00022.

(8) Edna Brustein, S. b. C., Julien Ghislain, Pierre Drapeau. Spontaneous Glycine-Induced Calcium Transients in Spinal Cord Progenitors Promote Neurogenesis. *Calcium Transients in Neurogenesis* **2012**. DOI: 10.1002/dneu.22050.

(9) Yang, L.; Wang, H.; Liu, L.; Xie, A. The Role of Insulin/IGF-1/PI3K/Akt/GSK3beta Signaling in Parkinson's Disease Dementia. *Front Neurosci* **2018**, *12*, 73. DOI: 10.3389/fnins.2018.00073.

(10) van Niekerk, E. A.; Tuszynski, M. H.; Lu, P.; Dulin, J. N. Molecular and cellular mechanisms of axonal regeneration after spinal cord injury. *Molecular & Cellular Proteomics* **2016**, *15* (2), 394-408. DOI: 10.1074/mcp.R115.053751.

(11) Daggupati, T.; Pamanji, R.; Yeguvapalli, S. In silico screening and identification of potential GSK3beta inhibitors. *J Recept Signal Transduct Res* **2018**, *38* (4), 279-289. DOI: 10.1080/10799893.2018.1478854.

(12) J. Guana, G. B. T., H. Lin b, S. Mathaib, D.C. Bachelor b, S. Georgea,; Gluckmana, P. D. Neuroprotective effects of the N-terminal tripeptide of insulin-like growth factor-1, glycine-proline-glutamate (GPE) following intravenous infusion in hypoxic–ischemic adult rats. *Neuropharmacology* **2004**, *47*, 892–903. DOI: 10.1016/j.neuropharm.2004.07.002.

(13) Zhang, Q.; Deng, Y.-X.; Luo, H.-X.; Shi, C.-Y.; Geise, G. M.; Feringa, B. L.; Tian, H.; Qu, D.-H. Assembling a Natural Small Molecule into a Supramolecular Network with High Structural Order and Dynamic Functions. *Journal of the American Chemical Society* **2019**, *141* (32), 12804-12814. DOI: 10.1021/jacs.9b05740.

(14) Peressotti, S.; Koehl, G. E.; Goding, J. A.; Green, R. A. Self-Assembling Hydrogel Structures for Neural Tissue Repair. *ACS Biomater Sci Eng* **2021**, *7* (9), 4136-4163. DOI: 10.1021/acsbiomaterials.1c00030.

(15) Cheng, Q.; Yu, X.; Xiong, Z.; Wan, Z.; Li, Y.; Ma, W.; Tan, W.; Liu, M.; Shea, K. J. Abiotic Synthetic Antibodies to Target a Specific Protein Domain and Inhibit Its Function. *ACS Applied Materials & Interfaces* **2022**, *14* (17), 19178-19191. DOI: 10.1021/acsami.2c02287.

(16) Bentolila, A.; Vlodavsky, I.; Ishai-Michaeli, R.; Kovalchuk, O.; Haloun, C.; Domb, A. J. Poly (N-acryl amino acids): a new class of biologically active polyanions. *Journal of medicinal chemistry* **2000**, *43* (13), 2591-2600. DOI: 10.1021/jm000089j.

(17) Seuring, J.; Agarwal, S. Polymers with Upper Critical Solution Temperature in Aqueous Solution: Unexpected Properties from Known Building Blocks. *ACS Macro Letters* **2013**, *2* (7), 597-600. DOI: 10.1021/mz400227y.

(18) Cui, C.; Wu, T.; Gao, F.; Fan, C.; Xu, Z.; Wang, H.; Liu, B.; Liu, W. An Autolytic High Strength Instant Adhesive Hydrogel for Emergency Self-Rescue. *Advanced Functional Materials* **2018**, *28* (42), 1804925. DOI: 10.1002/adfm.201804925.

(19) Gao, F.; Xu, Z.; Liang, Q.; Li, H.; Peng, L.; Wu, M.; Zhao, X.; Cui, X.; Ruan, C.; Liu, W. Osteochondral regeneration with 3D-printed biodegradable high-strength supramolecular polymer reinforced-gelatin hydrogel scaffolds. *Advanced Science* **2019**, *6* (15), 1900867. DOI: 10.1002/advs.201900867.

(20) Deepuppha, N.; Khadsai, S.; Rutnakornpituk, B.; Wichai, U.; Rutnakornpituk, M. Multiresponsive Poly(N-Acryloyl glycine)-Based Nanocomposite and Its Drug Release Characteristics. *Journal of Nanomaterials* **2019**, *2019*, 1-12. DOI: 10.1155/2019/8252036.

(21) Liumin He, Q. X., Yuyuan Zhao, Jun Li, Sathish Reddy, Xueshuang Shi, Xin Su, Kin Chiu,; Ramakrishna, a. S. Engineering an Injectable Electroactive Nanohybrid Hydrogel for Boosting Peripheral Nerve Growth and Myelination in Combination with Electrical Stimulation. *ACS Appl. Mater. Interfaces* **2020**, *12*, 53150−53163. DOI: 10.1021/acsami.0c16885.

(22) Hsieh, F.-Y.; Tseng, T.-C.; Hsu, S.-h. Self-healing hydrogel for tissue repair in the central nervous system. *Neural regeneration research* **2015**, *10* (12), 1922. DOI: 10.4103/1673-5374.169624.

(23) Nagappan, P. G.; Chen, H.; Wang, D.-Y. Neuroregeneration and plasticity: a review of the physiological mechanisms for achieving functional recovery postinjury. *Military Medical Research* **2020**, *7* (1), 30-30. DOI: 10.1186/s40779-020-00259-3 PubMed.

(24) Zamproni, L. N.; Mundim, M. T.; Porcionatto, M. A. Neurorepair and regeneration of the brain: a decade of bioscaffolds and engineered microtissue. *Frontiers in cell and developmental biology* **2021**, *9*, 649891. DOI: 10.3389/fcell.2021.649891.

(25) Zewen Liu, 2 Tingyang Zhou,1,3 Alexander C. Ziegler,4 Peter Dimitrion,4 and Li Zuo1,3. Oxidative Stress in Neurodegenerative Diseases: From Molecular Mechanisms to Clinical Applications. *Oxidative Medicine and Cellular Longevity* **2017**, 11. DOI: 10.1155/2017/2525967.

(26) Lv, Z.-F.; Xu, B.; Wang, J.-T. N-Acryloylglycine. *Acta Crystallographica Section E Structure Reports Online* **2006**, *62* (8), o3344-o3345. DOI: 10.1107/s1600536806026201.

(27) Schindelin, J.; Arganda-Carreras, I.; Frise, E.; Kaynig, V.; Longair, M.; Pietzsch, T.; Preibisch, S.; Rueden, C.; Saalfeld, S.; Schmid, B.; Tinevez, J.-Y.; White, D. J.; Hartenstein, V.; Eliceiri, K.; Tomancak, P.; Cardona, A. Fiji: an open-source platform for biological-image analysis. *Nature Methods* **2012**, *9* (7), 676-682. DOI: 10.1038/nmeth.2019.

(28) Yamala, A. K.; Nadella, V.; Mastai, Y.; Prakash, H.; Paik, P. Poly-N-acryloyl-(L-phenylalanine methyl ester) hollow core nanocapsules facilitate sustained delivery of immunomodulatory drugs and exhibit adjuvant properties. *Nanoscale* **2017**, *9* (37), 14006-14014. DOI: 10.1039/c7nr03724d.

(29) Brady, J.; Dürig, T.; Lee, P.; Li, J.-X. Polymer properties and characterization. *Developing solid oral dosage forms* **2017**, 181-223. DOI: https://doi.org/10.1016/B978-0-12-802447-8.00007-8.

(30) Ringeard, J. M.; Griesmar, P.; Caplain, E.; Michiel, M.; Serfaty, S.; Huerou, J. Y. L.; Marinkova, D.; Yotova, L. Design of poly (N-acryloylglycine) materials for incorporation of microorganisms. *Journal of Applied Polymer Science* **2013**, *130* (2), 835-841. DOI: 10.1002/app.39242.

(31) Shim, S. E.; Yang, S.; Jung, H.; Choe, S. Thermally robust highly crosslinked poly (methyl methacrylate-co-divinyl benzene) microspheres by precipitation polymerization. *Macromolecular research* **2004**, *12* (2), 233-239. DOI: 10.1007/BF03218393.

(32) Vlad, C. D.; Dinu, M. V.; Dragan, S. Thermogravimetric analysis of some crosslinked acrylamide copolymers and ion exchangers. *Polymer degradation and stability* **2003**, *79* (1), 153-159. DOI: 10.1016/S0141-3910(02)00268-9.

(33) Van Dyke, J. D.; Kasperski, K. L. Thermogravimetric study of polyacrylamide with evolved gas analysis. *Journal of Polymer Science Part A: Polymer Chemistry* **1993**, *31* (7), 1807-1823. DOI: https://doi.org/10.1002/pola.1993.080310720.

(34) Dassanayake, N. L.; Phillips, R. W. Determination of the composition of acrylamide/acrylate copolymers using thermogravimetric analysis. *Analytical Chemistry* **1984**, *56* (9), 1753-1755. DOI: https://doi.org/10.1021/ac00273a056.

(35) Kornev, V. A.; Grebenik, E. A.; Solovieva, A. B.; Dmitriev, R. I.; Timashev, P. S. Hydrogel-assisted neuroregeneration approaches towards brain injury therapy: A state-of-the-art review. *Comput Struct Biotechnol J* **2018**, *16*, 488-502. DOI: 10.1016/j.csbj.2018.10.011.

(36) Madhusudanan, P.; Raju, G.; Shankarappa, S. Hydrogel systems and their role in neural tissue engineering. *Journal of the Royal Society Interface* **2020**, *17* (162), 20190505. DOI: https://doi.org/10.1098/rsif.2019.0505.

(37) Shah, R.; Saha, N.; Kitano, T.; Saha, P. Influence of Strain on Dynamic Viscoelastic Properties of Swelled (H2o) And Biomineralized (Caco3) Pvp-Cmc Hydrogels. *Applied Rheology* **2015**, *25* (3), 13-22. DOI: 10.3933/applrheol-25-33979 (acccessed 2023-02-06).

(38) Donato, M. T.; Tolosa, L.; Gómez-Lechón, M. J. Culture and functional characterization of human hepatoma HepG2 cells. In *Protocols in In Vitro Hepatocyte Research*, Springer, 2015; pp 77-93.

(39) Lee, I. B.; Son, H. H.; Um, C. M. Rheologic properties of flowable, conventional hybrid, and condensable composite resins. *Dental materials : official publication of the Academy of Dental Materials* **2003**, *19* (4), 298-307. DOI: 10.1016/s0109-5641(02)00058-1.

(40) Wiatrak, B.; Kubis-Kubiak, A.; Piwowar, A.; Barg, E. PC12 cell line: cell types, coating of culture vessels, differentiation and other culture conditions. *Cells* **2020**, *9* (4), 958. DOI: 10.3390/cells9040958.

(41) Wang, J.; Tian, L.; Chen, N.; Ramakrishna, S.; Mo, X. The cellular response of nerve cells on poly-l-lysine coated PLGA-MWCNTs aligned nanofibers under electrical stimulation. *Materials Science and Engineering: C* **2018**, *91*, 715-726. DOI: DOI: 10.1016/j.msec.2018.06.025.

(42) Xu, G.; Pierson, C. R.; Murakawa, Y.; Sima, A. A. Altered tubulin and neurofilament expression and impaired axonal growth in diabetic nerve regeneration. *Journal of Neuropathology & Experimental Neurology* **2002**, *61* (2), 164-175. DOI: https://doi.org/10.1093/jnen/61.2.164.

(43) Latremoliere, A.; Cheng, L.; DeLisle, M.; Wu, C.; Chew, S.; Hutchinson, E. B.; Sheridan, A.; Alexandre, C.; Latremoliere, F.; Sheu, S. H.; Golidy, S.; Omura, T.; Huebner, E. A.; Fan, Y.; Whitman, M. C.; Nguyen, E.; Hermawan, C.; Pierpaoli, C.; Tischfield, M. A.; Woolf, C. J.; Engle, E. C. Neuronal-Specific TUBB3 Is Not Required for Normal Neuronal Function but Is Essential for Timely Axon Regeneration. *Cell Rep* **2018**, *24* (7), 1865-1879 e1869. DOI: 10.1016/j.celrep.2018.07.029.

(44) Dráberová, E.; Del Valle, L.; Gordon, J.; Marková, V.; Šmejkalová, B.; Bertrand, L.; de Chadarévian, J.-P.; Agamanolis, D. P.; Legido, A.; Khalili, K. Class III β-tubulin is constitutively coexpressed with glial fibrillary acidic protein and nestin in midgestational human fetal astrocytes: implications for phenotypic identity. *Journal of Neuropathology & Experimental Neurology* **2008**, *67* (4), 341-354. DOI: 10.1097/NEN.0b013e31816a686d.

(45) Silva, T. P.; Bekman, E. P.; Fernandes, T. G.; Vaz, S. H.; Rodrigues, C. A. V.; Diogo, M. M.; Cabral, J. M. S.; Carmo-Fonseca, M. Maturation of Human Pluripotent Stem Cell-Derived Cerebellar Neurons in the Absence of Co-culture. *Front Bioeng Biotechnol* **2020**, *8*, 70. DOI: 10.3389/fbioe.2020.00070.

(46) Clark, B. A.; Monsivais, P.; Branco, T.; London, M.; Häusser, M. The site of action potential initiation in cerebellar Purkinje neurons. *Nature neuroscience* **2005**, *8* (2), 137-139. DOI: 10.1038/nn1390.

(47) Masoli, S.; Solinas, S.; D'Angelo, E. Action potential processing in a detailed Purkinje cell model reveals a critical role for axonal compartmentalization. *Frontiers in Cellular Neuroscience* **2015**, *9*, 47. DOI: 10.3389/fncel.2015.00047.

(48) Bhat, R.; Xue, Y.; Berg, S.; Hellberg, S.; Ormo, M.; Nilsson, Y.; Radesater, A. C.; Jerning, E.; Markgren, P. O.; Borgegard, T.; Nylof, M.; Gimenez-Cassina, A.; Hernandez, F.; Lucas, J. J.; Diaz-Nido, J.; Avila, J. Structural insights and biological effects of glycogen synthase kinase 3-specific inhibitor AR-A014418. *The Journal of biological chemistry* **2003**, *278* (46), 45937-45945. DOI: 10.1074/jbc.M306268200.

(49) de la Torre, A. V.; Junyent, F.; Folch, J.; Pelegrí, C.; Vilaplana, J.; Auladell, C.; Beas-Zarate, C.; Pallàs, M.; Verdaguer, E.; Camins, A. GSK3β inhibition is involved in the neuroprotective effects of cyclin-dependent kinase inhibitors in neurons. *Pharmacological research* **2012**, *65* (1), 66-73. DOI: 10.1016/j.phrs.2011.08.006.

(50) Lee, Y.; Yoon, S. B.; Hong, H.; Kim, H. Y.; Jung, D.; Moon, B. S.; Park, W. K.; Lee, S.; Kwon, H.; Park, J.; Cho, H. Discovery of GSK3beta Inhibitors through In Silico Prediction-and-Experiment Cycling Strategy, and Biological Evaluation. *Molecules* **2022**, *27* (12). DOI: 10.3390/molecules27123825.

(51) Riley, L.; Schirmer, L.; Segura, T. Granular hydrogels: emergent properties of jammed hydrogel microparticles and their applications in tissue repair and regeneration. *Curr Opin Biotechnol* **2019**, *60*, 1-8. DOI: 10.1016/j.copbio.2018.11.001.

(52) Clausen, T.; Khaldi, A.; Zauner, A.; Reinert, M.; Doppenberg, E.; Menzel, M.; Soukup, J.; Alves, O. L.; Bullock, M. R. Cerebral acid—base homeostasis after severe traumatic brain injury. *Journal of neurosurgery* **2005**, *103* (4), 597-607. DOI: 10.3171/jns.2005.103.4.0597.

(53) Chaumeil, M. M.; Valette, J.; Baligand, C.; Brouillet, E.; Hantraye, P.; Bloch, G.; Gaura, V.; Rialland, A.; Krystkowiak, P.; Verny, C.; Damier, P.; Remy, P.; Bachoud-Levi, A.

C.; Carlier, P.; Lebon, V. pH as a biomarker of neurodegeneration in Huntington's disease: a translational rodent-human MRS study. *Journal of cerebral blood flow and metabolism : official journal of the International Society of Cerebral Blood Flow and Metabolism* **2012**, *32* (5), 771-779. DOI: 10.1038/jcbfm.2012.15.

(54) Anderson, R. L.; Merkler, D. J. N-FATTY ACYLGLYCINES: UNDERAPPRECIATED ENDOCANNABINOID-LIKE FATTY ACID AMIDES? *J Biol Nat* **2017**, *8* (4), 156-165. From NLM.

(55) Guvendiren, M.; Lu, H. D.; Burdick, J. A. Shear-thinning hydrogels for biomedical applications. *Soft Matter* **2012**, *8* (2), 260-272. DOI: 10.1039/c1sm06513k.

(56) Grevesse, T.; Dabiri, B. E.; Parker, K. K.; Gabriele, S. Opposite rheological properties of neuronal microcompartments predict axonal vulnerability in brain injury. *Sci Rep* **2015**, *5*, 9475. DOI: 10.1038/srep09475.

(57) Leipzig, N. D.; Shoichet, M. S. The effect of substrate stiffness on adult neural stem cell behavior. *Biomaterials* **2009**, *30* (36), 6867-6878. DOI: 10.1016/j.biomaterials.2009.09.002.

(58) Ali, S.; Wall, I. B.; Mason, C.; Pelling, A. E.; Veraitch, F. S. The effect of Young's modulus on the neuronal differentiation of mouse embryonic stem cells. *Acta Biomater* **2015**, *25*, 253-267. DOI: 10.1016/j.actbio.2015.07.008.

(59) Lamprecht, R. Actin Cytoskeleton Role in the Maintenance of Neuronal Morphology and Long-Term Memory. *Cells* **2021**, *10* (7). DOI: 10.3390/cells10071795.

(60) Liz, M. A.; Mar, F. M.; Santos, T. E.; Pimentel, H. I.; Marques, A. M.; Morgado, M. M.; Vieira, S.; Sousa, V. F.; Pemble, H.; Wittmann, T.; Sutherland, C.; Woodgett, J. R.; Sousa, M. M. Neuronal deletion of GSK3β increases microtubule speed in the growth cone and enhances axon regeneration via CRMP-2 and independently of MAP1B and CLASP2. *BMC Biology* **2014**, *12* (1), 47. DOI: 10.1186/1741-7007-12-47.

(61) Cuesto, G.; Jordan-Alvarez, S.; Enriquez-Barreto, L.; Ferrus, A.; Morales, M.; Acebes, A. GSK3beta inhibition promotes synaptogenesis in Drosophila and mammalian neurons. *PLoS One* **2015**, *10* (3), e0118475. DOI: 10.1371/journal.pone.0118475.

(62) Reddy, P. H. Amyloid beta-induced glycogen synthase kinase 3beta phosphorylated VDAC1 in Alzheimer's disease: implications for synaptic dysfunction and neuronal damage. *chim Biophys Acta* **2013**, *1832* (12), 1913-1921. DOI: 10.1016/j.bbadis.2013.06.012.

(63) Khatri, N.; Thakur, M.; Pareek, V.; Kumar, S.; Sharma, S.; Datusalia, A. K. Oxidative stress: major threat in traumatic brain injury. *CNS & Neurological Disorders-Drug Targets (Formerly Current Drug Targets-CNS & Neurological Disorders)* **2018**, *17* (9), 689-695. DOI: https://doi.org/10.2174/1871527317666180627120501.

(64) Musgrove, R. E.; Helwig, M.; Bae, E.-J.; Aboutalebi, H.; Lee, S.-J.; Ulusoy, A.; Di Monte, D. A. Oxidative stress in vagal neurons promotes parkinsonian pathology and intercellular α-synuclein transfer. *The Journal of Clinical Investigation* **2019**, *129* (9), 3738-3753. DOI: 10.1172/JCI127330.

(65) Smethurst, P.; Risse, E.; Tyzack, G. E.; Mitchell, J. S.; Taha, D. M.; Chen, Y.-R.; Newcombe, J.; Collinge, J.; Sidle, K.; Patani, R. Distinct responses of neurons and astrocytes to TDP-43 proteinopathy in amyotrophic lateral sclerosis. *Brain* **2020**, *143* (2), 430-440. DOI: 10.1093/brain/awz419.

CHAPTER 3. RESULTS AND DISCUSSION (PART-II)

Objective II: *Modulation Of P(NAG-b-Ac) Bio-Polymer By Glutamate To Synthesize For Poly (N-Acryloyl Glycine)-Co-(Acrylamide)-(N-Acryloyl Glutamate) For Angiogenesis And Neuroregeneration.*

3.2.1 **ABSTRACT.**

Traumatic injuries, neurodegenerative diseases and oxidative stress serve as the early biomarkers for neuronal damage, impede angiogenesis and subsequently neuronal growth. In this direction, the present work is aimed to develop angiogenesis/neurogenesis properties imprinted poly(N-acryloylglycine)-co-(acrylamide)-co-(N-acryloylglutamate) hydrogel [p(NAG-Ac-NAE)]. As constituents of this polymer modulate the vital role in biological functions, inhibitory neurotransmitter glycine regulates neuronal homeostasis, and glutamatergic signalling regulates angiogenesis. The p(NAG-Ac-NAE) is a highly-branched, biodegradable and pH-responsive polymer with very high swelling behavior of 6188%. Mechanical stability (G', 2.3-2.7 kPa) of this polymeric hydrogel is commendable in the differentiation of the mature neurons. This hydrogel is biocompatible (tested in HUVEC cells) and helps to proliferate the PC12 cells (152.7±13.7 %), whereas cytotoxic towards the aggressive cancer such as glioblastoma (LN229 cells) and triple negative breast cancer (TNBC, MDA-MB-231 cells) and helps to maintain the healthy cytoskeleton framework structure of primary cortical neurons by facilitating the elongation of the axonal pathway. Furthermore, FACS results revealed that the synthesized hydrogel potentiates the neurogenesis by inducing the cell cycle (G0/G1) and arresting the sub-G1 phase by limiting

apoptosis. Additionally, RT-PCR results revealed that this hydrogel induced an increased level of HIF-1α expression providing the preconditioning effects towards the neuronal cells under oxidative stress conditions via scavenging ROS and initiating the neurogenic and angiogenic signaling. This hydrogel further exhibits more pro-angiogenic activities via increasing the expression of VEGF isoforms as compared to the previously reported hydrogels. In conclusion, newly synthesized p(NAG-Ac-NAE) hydrogel could be one of the potential neuroregenerative materials for vasculogenesis-assisted neurogenic applications and paramount for the management of neurodegenerative diseases.

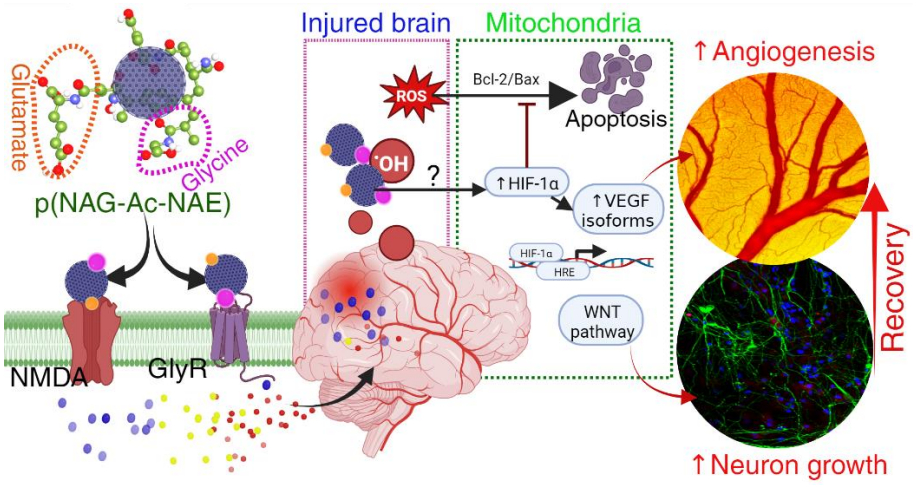

"***For Table of Contents Only****": Poly[(N-acryloylglycine)-co-(acrylamide)-co-(N-acryloyl glutamate)] is an angiogenic and neurogenic hydrogel, which assists neurite outgrowth and shows protective role via scavenging the ROS generation through the mitochondrial membrane depolarization in oxidative stress conditions.*

3.2.2 INTRODUCTION.

Lack of regenerative properties of nervous system (CNS/PNS), inadequate knowledge of CNS development, pathophysiology, disease progression mechanisms, diminished therapeutic effect of active ingredients due to blood-brain barrier (BBB) and lack of multifunctional responses of biomaterials limits the development of clinically effective neuroregenerative properties[1] along with limited therapeutic success rate.[1, 2] Injury and

aging-associated neurological disorders are continuously increasing, and are the second leading causes of death worldwide.[3, 4]' Among the neurological disorders, stroke, migraine, Alzheimer dementias (AD) are the major contributors for the traumatic brain injury (TBI). [4] [5] Vascular damage, increased inflammations, oxidative stress and insufficient blood supply are the leading causes of death and neurological disability in stroke/TBI and failure in recovery with the existing treatment options.[5, 6]'. Hence, angiogenic therapeutic material could promote the de nevo tissue formation along with the increase in developed blood vessels and axonal network. [7] [8] Polymeric materials exhibit fascinating advantages in medical biotechnology due to their biocompatibility, possibility to multiple interactions with proteins and excellent *in vivo* stability. [8] [9] Chitosan, albumin, polylactic acid (PLA) and poly(ethylenimine), etc. are the few polymers that are used to develop 3D scaffolds and hydrogels[9][10] for nerve repair. Unfortunately, available synthetic polymeric hydrogels have a lot of limitations, such as most of them are poor in cell adhesion, produce toxic degradation products and photo-responsive hydrogel shows potential toxicity due to the presence of functional groups and poor reproducibility of the structure. [1] For example, alginate hydrogel limits their applications due to the requirement of the multistep purification process. The use of various polymers such as polylactic glycolic acid (PLA) is limited due to the lack of functional groups and low electric conduction. polycaprolactone (PCL) limits its uses due to the high crystallinity and use of protein/peptide have failed to get FDA approval due to the unsatisfactory pharmacokinetics and unspecificity of targets. [10] [11]

The incorporation of amino acids into synthetic polymer forms the ordered hierarchical structures and favors the exceptional chemical, physical properties and stimuli-responsive properties along with excellent biocompatibility and degradability. [11] [12] Reported glutamate-based (poly(γ-glutamic acid) (PLGA)) is a promising polymer for biomedical

applications due to their biocompatible and non-immunogenic nature. [12] [13] PLGA in conjugation with different organic moieties exhibits pH responsiveness[13][14] and shows excellent adhesive strength in visceral tissues. [14] [15] PLGA composites inherited good mechanical strength with self-healing ability, beneficial in chondrogenic differentiation and accelerates the cutaneous wound healing efficiency. [15] [16] Recently, we have shown the neurogenic potential of p(NAG-b-A) hydrogel. [16][17] However, previous studies has limited to neurogenic potential but not explored for angiogenic properties. Similarly, none of the studies were explored, which supported the development of glutamate and glycine-based co-polymeric hydrogels development for their dual angiogenic and neurogenic potential.

Glutamate and glycine are the crucial components in neuronal homeostasis, in learning and memory, in cell-cell communication, play ubiquities role in neuroprotective action, neural stem cell survival and in neurogenic programming. Accumulated form of glycine and glutamate in synaptic vesicles involved in the synaptic plasticity. And aging are associated with the disturbed protein synthesis kinetic due to decreasing level of transmitters.[17, 18] Anatomically, neurons and vasculature undergo parallel development and hence material should deliver the neurotrophic factors in a specific concentration or should have the angiogenic and neurogenic properties. A few nanomaterials are known for both neurogenic and angiogenic properties [19, 20] but not known for hydrogel or hydrogel encapsulated with neurotrophic factors. [21] [22] Therefore, in the present work the novel polymeric hydrogel was applied to develop neurogenic and angiogenic dual property-bearing hydrogel for effective neurogenesis. Hence, in the present work the synthesis of angiogenic and neurogenic biological cues containing non-tumorigenic p(NAG-Ac-NAE) hydrogel was carried out. After performing physical characterization and analyzing the rheological properties, the biocompatibility was assessed in HUVEC and normal healthy cell lines. It

is known that the angiogenic potential of the material could show a positive impact on recovery from nerve injury. In the present work, the angiogenic behavior of p(NAG-Ac-NAE) has also been evaluated *in ovo* system and compared with the inhibitory glycine-containing p(NAG-b-A) hydrogel. Through the *in vitro* study neurogenic potential and protective role in oxidative stress has been investigated. Finally, based on the experimental evidence, the p(NAG-Ac-NAE) hydrogel has been used in this work that holds the potential role in promoting neurite growth along with the pro-angiogenic properties and is paramount for the management of the neurodegenerative diseases.

3.2.3 EXPERIMENTAL

3.2.3.1. Synthesis of N-acryloyl-glycine and N-acryloyl-glutamate monomers. N-acryloyl-glycine (*Patent No.: 419638, Granted on. 30-01-2023*) and N-acryloyl-glutamic acid[22] was prepared following the similar method mentioned in chapter 2.

3.2.3.2. Synthesis of p(NAG-Ac-NAE) Hydrogel. Free radical, mini-emulsification polymerization technique was used for the synthesis of p(NAG-Ac-NAE) hydrogel detail mentioned in chapter 2. Further, chemical functionality was confirmed through the FTIR, ^{1}H NMR and ^{13}C NMR. To measure the molecular weight MALDI-TOF experiments were performed for p(NAG-Ac-NAE) using $CDCl_3$ and DMSO-d_6 solvent (1:1) and using ditharnol matrix. The molecular weight (MW) and PDI were calculated using eq.1-3.

$$\mathrm{Mn} = \frac{\sum MiNi}{\sum Ni} \text{ ---------- (1)}$$

$$M\mathrm{w} = \frac{\sum \mathrm{Mi}^2\ \mathrm{Ni}}{\sum \mathrm{MiNi}} \text{ ---------- (2)}$$

$$\mathrm{PDI} = \frac{\mathrm{Mw}}{\mathrm{Mn}} \text{ ---------- (3)}$$

Where, number average molecular weight (M_n), weight average molecular weight (M_w), polydispersity Index (PDI), M_i is mass of the 'i' oligomer and N_i is number of the i^{th} oligomer.[23] Detailed synthesis method of this hydrogel has been filed for a Indian Patent (*Ref. 202311038604, Dated: June 5th, 2023).*

3.2.3.3. Physical and Morphological Evaluation of p(NAG-NAE-A) Hydrogel. For FTIR spectrum, ^{1}H NMR and ^{13}C NMR spectra TGA plot,and was obtained and for morphological evaluation HRTEM was performed.

3.2.3.4. Mass swelling index (MSI) measurement. Dynamic swelling behavior was obtained by immersing the hydrogel with a PBS buffer of different pH (3, 5, 6, 7.4 and 8). After the specified time interval the excess buffer was removed and the mass measured. Then the mass swelling indexes (MSI) were calculated by eq. 4.

$$MSI = \frac{(Ws - Wd)}{Wi} \times 100 \text{ ---------- (4)}$$

Where, W_s is the weight of swelled hydrogel and W_d is the weight of dried hydrogel.

Furthermore, hydrodynamic diameter was calculated using zeta sizer by immersing the hydrogel in water and the results were compared with the results obtained from HRTEM.

3.2.3.5. Biodegradation study. Bio-degradation studies were performed by immersing the 4 mg of p(NAG-Ac-NAE) hydrogel in 1 mL of PBS (pH 7.2) containing, 100 µg mL^{-1} proteinase K in PBS, 100 µg mL^{-1} Collagenase, in PBS and 100µg mL^{-1} lysozyme in PBS solution separately and incubated for 1, 7, 15, 21 and 30 days. After each time period of incubation MSI was calculated and graphically represented.

3.2.3.6. Rheological behavior study. The swollen hydrogel was placed between preheated/cooled rheometer parallel plates (30 mm in dia.) with a gap height of 0.5 mm and allowed to equilibrate at 25 °C for 2 min in each run and rheological data obtained by using Anton paar MCR 102 Rheometer. The shear test was performed in shear rate range from 10^{-6} to 10^{2} s^{-1} at 34 °C, 37 °C, 40 °C and 43 °C. Frequency sweep tests were conducted at

the range of 0.1-100 rad s^{-1} with an oscillating strain of 5 %. The temperature ramp test was carried out to determine the relationship between viscoelastic modulus and loss modulus (G″), storage modulus (G′), and the complex viscosity were measured as a function of angular frequency (ω) at different temperatures.

3.2.3.7. Cell cycle and cell proliferation assay. $1x10^5$/well PC12 cells were cultured for overnight (12 hrs) and 250 μg mL^{-1} p(NAG-Ac-NAE) hydrogel and p(NAG-b-A) hydrogel added separately in presence / absence of 40 μM H_2O_2 incubated for 24 hour. Afterward, cells were stained with propidium iodine (PI) and cell cycle stages determined by flow cytometry.

3.2.3.8. Animal ethical approval. Animal ethical approval has been taken (IIT(BHU)/IAEC/2022/079) and all the experimental procedures were performed as per the CPCSEA guideline obtained from Institution Animal Ethical Committee (IAEC) of IIT (BHU), Varanasi, Uttar Pradesh, India (Regd. No. 2123/GO/Re/S/21/CPCSEA).

3.2.3.9. Hemocompatibility of hydrogel. Whole blood samples were obtained from the animal and RBCs separated and 5 X 10^{10} were suspended in 5% dextrose solution (pH 7.4). Treatment with 5% dextrose solution was considered as negative control, while treatment with 0.1-1% Triton-X was considered as positive control. RBCs were incubated for 12 and 24 h at 37 °C/100 RPM with different concentrations (1000, 500, 250, 125 and 62.5 μg mL^{-1}) of p(NAG-Ac-NAE) hydrogel and generated haemolysis were estimated by recording the absorbance at 540 nm.

3.2.3.10. Determination of intracellular ROS generation and effect on mitochondrial potential. PC12 cells were seeded in 6 well plates and incubated for 24 h. After that the cells were exposed with 20 μM and 40 μM of H_2O_2 and with 250 μg mL^{-1} of p(NAG-Ac-NAE) hydrogel and p(NAG b-A) hydrogel separately for 24 h. Only 20 μM and 40 μM of H_2O_2 treated cells were considered as positive control and samples without

treatment were considered as the negative control. Similarly, PC12 cells were also treated with 250 μg mL^{-1} of p(NAG-Ac-NAE) hydrogel and p(NAG b-A) hydrogel separately without exposure of H_2O_2., After 24 h of incubation with H_2O_2, p(NAG-Ac-NAE) hydrogel and p(NAG b-A) hydrogel, cells were harvested by treating the cells with 1 mM of EDTA for 20 min and washed with ice-cold PBS by centrifuging at 1000 X g for 5 min. The pellet was re-suspended in 500 μL of PBS and 50 μM solution of 2',7'–dichlorofluorescin diacetate DCFDA added and incubated in 5% CO_2 incubator at 37 ℃ for 30 min. The ability of intracellular ROS production was measured by using a flow cytometer (Beckman coulter). Similarly, for determination of the effect on mitochondrial potential, $1X10^4$ PC12 cells seeded in per well of 48 well plate and the cells exposed with 20 μM and 40 μM of H_2O_2 and with/without 250 μg mL^{-1} of p(NAG-Ac-NAE) hydrogel and p(NAG b-A) hydrogel separately., After 24 h of treatment, treated media replaced with 5 μM Rhodamine 123 and 1 μg mL^{-1} of propidium iodide containing serum free media. After incubation of 15 min at 5% CO_2 incubator at 37 ℃, fluorescent intensity was measured at excitation of 488 nm to emission 520 nm and excitation of 550 nm to emission 610 nm.

3.2.3.11. Egg yolk angiogenesis assay. For the investigation of vascular sprouting CEA assay was performed with fertilized chicken eggs, which were purchased from certified poultry, Varanasi, Uttar Pradesh, India. Eggs were incubated at a humidified 37 ℃ incubator for 4 days. After that a small window was created and suspended particles of different concentrations1 μg mL^{-1}, 25 μg mL^{-1} and 100 μg mL^{-1} of hydrogel. Further images were acquired at different time intervals such as: 0, 2, 4 and 8 hours by fixing the Magnus Mag Cam DC-10-megapixel camera to the stereo zoom microscope. Images were then analyzed using Angiotool Fiji image J software.

3.2.3.12. Semi-quantitative reverse transcription and polymerase chain reaction (sqRT-PCR). In brief, $1x10^5$ PC12 cells and Raw264.7 cells were cultured in 6 well plate

and followed with treatment p(NAG-Ac-NAE) hydrogel and p(NAG b-A) in presence of H_2O_2 as per the experimental design. After 24 h of treatment, cells were collected and homogenized in 500µL TRIZOL reagent and RNA isolation was performed by phenol: chloroform extraction method. Next, RNA was precipitated from the collected aqueous layer using 1ml of isopropyl alcohol and centrifuge at 12000g for 15 min, 4° C. The RNA pellet was washed 2 times with 70% ice-cold ethanol and pallet was suspended in 50 µL DEPC treated water and quantified using nanodrop. After RNA quantification, 1µg of RNA was used for cDNA synthesis using oligo dT sequence and Reverse transcriptase polymerase as per the manufacture's protocol. Afterword, PCR was conducted using kicqkstart forward and reverse primer for biomarker target gene VEGFa, Kdr, HIF1α, TNFα, IL1β and housekeeping gene GAPDH as reference by using Taq polymerase (TAKARA R001A) with 35 repetitive cycle of denaturation at 95°C for 30 sec, annealing at 59° C for 35 sec and extension 72° C for 40 sec followed by final extension at 72° C for 7 min. PCR products were run on 2% agarose gel and densitometry calculations were performed.

3.2.3.13. Statistical Analysis. All the data were expressed as the mean of at least three means of separate experiments with (±) slandered error of the mean. Statistical significance ($p<0.05$) level was calculated by applying the one-way ANOVA test software.

3.2.4. RESULTS

3.2.4.1. Physical Characteristics of p(NAG-Ac-NAE) Hydrogel. p(NAG-Ac-NAE) hydrogel was synthesized through free radical/cross-linking polymerization approach as shown in Scheme 1. N-acryloylglycine, N-acrylamide and N-acryloylglutamate were taken in a 2:1:2 ratio, sonication was applied to get spherical hydrogel and polymerization was initiated by AIBN at 70 ℃ and cross-linking agent DVB

was used to obtain the spherical, pH-sensitive, highly branched and high wettability containing co-polymeric hydrogel nanoparticles. Chemical functionality for monomers and polymers were confirmed through the FTIR (Figure S3.2.1a), ^{1}H NMR and ^{13}C NMR (Figure S3.2.3). From FTIR the characteristic bands are detected at 3336 cm^{-1} (N─H (stretching)), 3182 cm^{-1} (─O─H stretching), 2912 cm^{-1} (─CH stretching, confirming the formation of a polymer chain) 1716 cm^{-1} (─C═O, carbonyl stretching), 1549 cm^{-1} (─O─H, overtone), and 1653 cm^{-1} (1st overtone of -NH) functional group. From ^{1}H NMR ($CDCl_3$) the chemical shifts of 12.5 δ (O-H of carboxylic acid), 8.9 δ (N─H of 2° amine), 7.26 δ (benzene), compound, 6.8 δ ($H_2C = CH_2$), 6.17 (─CH (12)) in ^{1}H NMR spectrum, and 44 and 34 ppm (8+2 splinted peak of 2° alkane) identified and 86-79 ppm (carboxylic ─OH and ester) in ^{13}C NMR spectrum confirmed the synthesis of p(NAG- Ac-NAE) polymers. To determine the average molecular weight, the MALDI-ToF spectrum was obtained (Figure S3.2.5) and results showed that the repeating unit varied from 194 to 224. The M_n and M_w are calculated to be 1690 Da, and 1773 Da, respectively with PDI of 1.04.

Particle size of the polymeric particles was confirmed through the FESEM (Figure 3.2.1a) and HRTEM (Figure 3.2.1b and 1c) and they are amorphous/semi crystalline in nature (Figure 3.2.1 d). The particle size was calculated to be 20-50 nm in diameter (Figure 3.2.1e-f), while the hydrodynamic diameter was obtained to be 189±5.16 nm (Figure 3.2.7). This increase in diameter is observed due to the swelling of hydrogel. Polymer particles developed here are highly branched, co-connected (HRTEM micrographs, Figure 3.2.1b) and porous in nature (pore dia. ~1.2 to 2.6 nm) (Figure 3.2.1c-g). From the HRTEM macrograph, it is also confirmed that there are short-range crystalline fringes (l ~2 nm) (Figure 3.2.1c) in the polymer particles which is responsible for the semi-crystalline nature of the hydrogel particles as it is shown in Figure 3.2.1d (SAED obtained from HRTEM), which is further confirmed through the XRD (Figure 3.2.1h). These particles are

crystalline/semi-crystalline due to the formation of ordered networks by cross-linking agent (DVB) and acryloylglycine. This semi-crystalline nature of this hydrogel enhances the thermal stability that is confirmed through the TGA (Figure S3.2.4a) and DSC analysis (Figure S3.2.4b). From TGA, four stages of mass loss are observed, such as in stage 1, a 6.99% mass loss at ~ 100 ℃ occurs due to the presence of free moisture. In stage-2, 3, and 4, 21.07%, 31.55% and 36.75% mass losses are respectively observed (Figure S3.2.4a) that occurred due to the degradation of the polymeric chains. To evaluate the thermal phase transition, DSC was recorded from -140 ℃ to 550 ℃ (Figure S3.2.4b). The glass transition (T_g) for p(NAG-Ac-NAE) hydrogel is observed to be - 45.17 ℃ and the first exothermic transition of p(NAG-Ac-NAE) hydrogel occurred at -10.48 ℃ (ΔH_c = 5.08 J g^{-1}), that revealed that at lower temperature hydrogel recrystallized to form a secondary phase (s). Another endothermic transition is observed at 31 ℃ to 69 ℃ with a peak position of 48.22 ℃ (ΔH_f= 2.37 J g^{-1}), due to the formation of a tertiary phase.

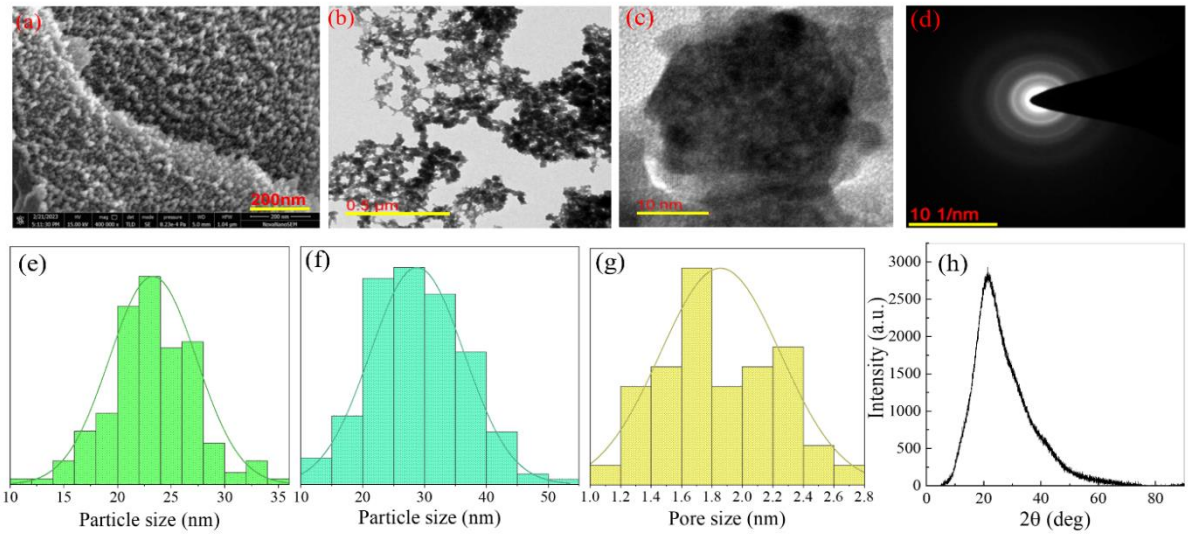

Figure 3.2. 1 Physical properties of poly-[(N-acryloyl-glycine)-co-(acrylamide)-co-(N-acryloyl glutamate)] (p(NAG-Ac-NAE)) hydrogel. (a) FESEM micrograph, (b) and (c) HRTEM micrograph at low and high magnification, respectively. (d) SAED pattern of the particles. (e) and (f) Average particle size distribution obtained from Figure 3.2.1(a) and

(b) respectively. (g) Pore size distribution of the particles obtained from 1c, and (h) XRD pattern of nanohydrogel.

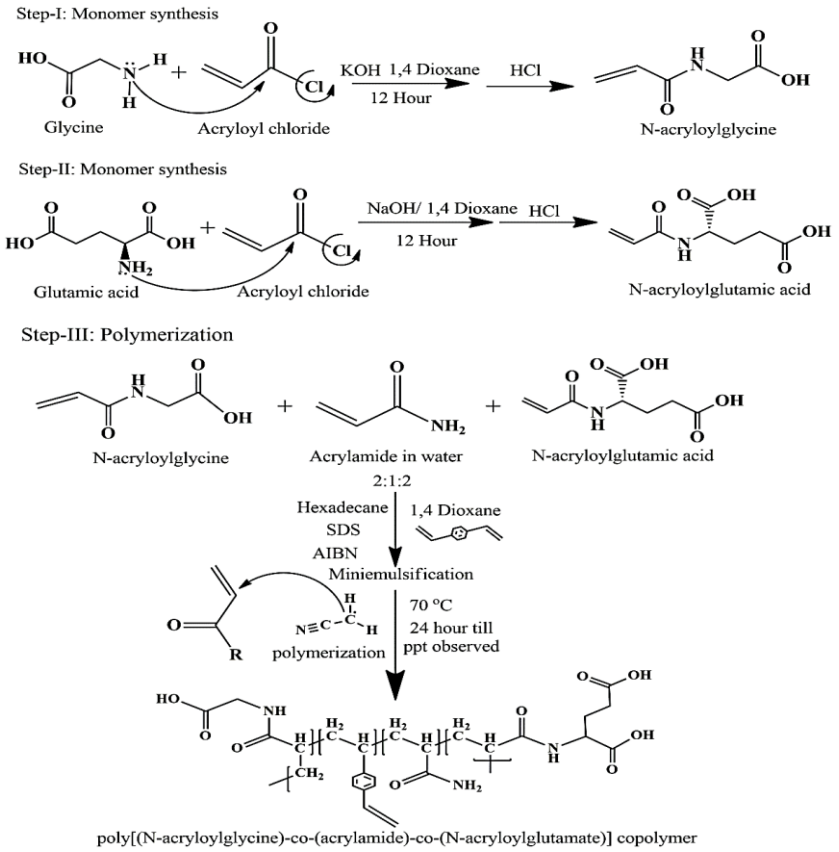

Scheme 3.2. 1 Representative steps of synthesis of poly-[(N-acryloylglycine)-co-(acrylamide)-co-(N-acryloylglutamate)] co-polymeric hydrogel

The third endothermic transition is observed at 238 ℃ which is correlated to the stage-2 mass loss of TGA and it corresponds to the loss of low molecular weight components. The transition phase started at 210 ℃ is due to the evolution of NH containing components.[24] Another exothermic transition that appeared at 305 ℃ is correlated with the TGA plot of hydrogel, is due to the degradation of the alkene and carboxylate groups.[24, 25]

3.2.4.2. Swelling Behavior of p(NAG-Ac-NAE) Hydrogel. The incorporation of a cross-linking agent (DVB) created the porous structure of the particles as shown in HRTEM (Figure 3.2.1c). The swelling behavior was evaluated by immersing and equilibrating the 5 mg of freeze-dried hydrogel in 1 mL of PBS buffer with a different pH range of 3, 5, 6, 7.4, and 8 (Figure 3.2.2a) at room temperature (25oC). From Figure 3.2.2a,

it is observed that the swelling behavior of the hydrogel is pH-dependent. At the pH 3, 5, 6, 7.4, and 8 the MSI were calculated at different time intervals and the values obtained to be within 45 min by 2274 %, 2458 %, 2872 %, 3676 % and 3383%, respectively, within 72 h (Figure 3.2.2a) The MSIs were obtained to be 2645 %, 4280 %, 4144 %, 6188 % and 5660 %, respectively (Figure 3.2.2a). The change in MSI with change in pH is observed due to the presence of a larger extent of ─COOH groups. Protonation of ─COOH makes the tighter and less hydrophilicity at lower pH, while at higher pH, the electrostatic interactions of ─COO─ groups are responsible for more hydration as well as more swelling.[13, 26] This hydrogel consists of an amide functional group. The resonance stabilized carbonyl group in amide makes it stable to over a week at 7.4, but sensitive to hydrolysis at to below pH 5.5. And as per our observed results, the highest swelling was achieved at pH 7.4, while the least at pH 6. Similarly, in basic pH conditions deprotonation generates the carboxylic acid and this carboxylic acid is responsible for the more hydration. As time increases the molecular degradation of p(NAG-Ac-NAE) has occurred due to the presence of an amide bond. And hence, we may observe the increase in swelling at pH-6 and pH-8 after 3000 min.[27, 28] Further, hydrogel was taken in water and the size distribution, zeta potential and conductivity were measured with DLS (Figure S3.2.7). The hydrogel nanoparticle's average hydrodynamic diameter is 1250 ± 6.28 nm with a PDI of 0.695. This increase in the particle size is observed due to the swelling of the hydrogel particle. Average zeta potential value (ζ) is calculated to be ─36.9 (± 6.28) mV at 25 °C. The conductivity of p(NAG-Ac-NAE) hydrogel was also measured to be 7.85 X 10-5 S cm^{-1}, which is in the semiconducting range and can be correlated with the conductivity of the brain tissues. The hydrodynamic diameter obtained from DLS and the particle size results obtained from TEM (Figure 3.2.1c) can be correlated and found that there is ~ 40 times (6400 %) increase in the in the swelling of the hydrogel particles.

3.2.4.3. Biodegradation Behaviours. The biodegradation behaviour of the hydrogel have been studied in terms of swelling behavior in presence of different pH and in presence of different enzymes, *i.e*., lysozyme, proteinase K and collagenase to mimic biological mediums that the MSI varied both with the medium as well as with time and pH. At the pH the degradation was observed as 3>5>6>7.4>8 (Figure 3.2.2b). The maximum MSI observed within 12 h of incubation by 5402 %, 4672 %, 7966 %, and 6067 % for PBS, lysozyme, proteinase K and collagenase, respectively. However, subsequently the swelling index values for hydrogel decreased continuously after 12 h, due to the degradation of the polymer chains in the presence of the enzymes. This biodegradation is observed up to 24 days and then continuously degraded as shown in Figure 3.2.2b during the experiment replacement of enzyme solution with 5 days of interval have been conducted). After 24 h of incubation, the highest degradation is observed in the presence of lysozyme and PBS. However, when the hydrogel was incubated for 40 days in the same solution (without replacing) (Figure S3.2.6), the highest degradation was observed in the presence of lysozyme and PBS. The swelling ratio of the hydrogel has increased after 7 days of incubation with Proteinase K. This increase in the swelling occurred due to the agglomeration and enzymatic degradation followed by the formation of a new complex compound (Figure S3.2.6).

Monomeric unit like N-acryloylglycine and N-acryloyl-glutamate don't show any bioactivity. p(NAG-Ac-NAE) polymer formation was conducted through the free radical polymerization where it formed the chain of N-acryloyl glycine and N-acryloyl glutamate, N-acryloylglycine and acrylamide, N-acryloyl-glutamate and acrylamide and N-acryloylglycine-acrylamide-N-acryloyl-glutamate, etc., which are cross-linked with divinyl benzene (DVB). Furthermore, we have found out through the in silico investigation that instead of a monomeric unit, when it converted into dimeric, trimeric and tetrameric

unit, it shows the high protease inhibitory activity and less enzyme inhibitory activity (See table S3.2.1). Thus, in physiological conditions and in the presence of different biological components, and this degradable hydrogel is advantageous to use in the living body for therapeutic applications.

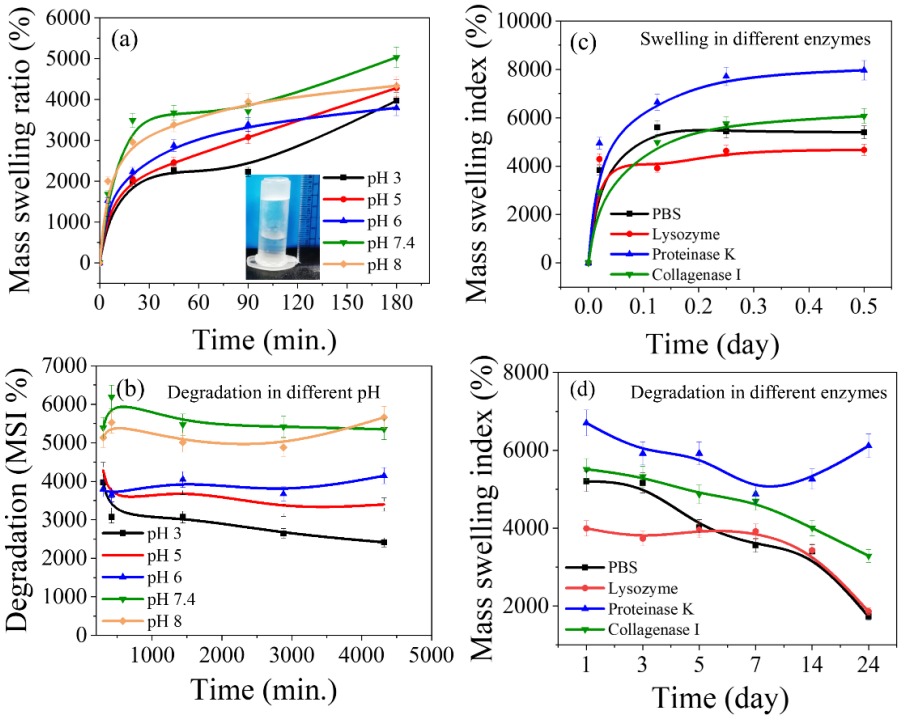

Figure 3.2. 2 . Swelling and degradation behaviour (a) MSI of the hydrogel at different pH of PBS, (b) Degradation of hydrogel in different pH, (c) MSI of hydrogel in different enzymes and (d) Degradation of hydrogel in the presence of different enzymatic solutions: Lysozyme, Proteinase K and collagenase IV with 100 μg mL^{-1} concentration and PBS (with continuous replacement of buffer).

3.2.4.4. Viscoelastic and Rheological flow behaviour. Viscoelastic and rheological flow behavior of p(NAG-Ac-NAE) hydrogel were measured through the frequency sweep measurement and steady shear measurement.

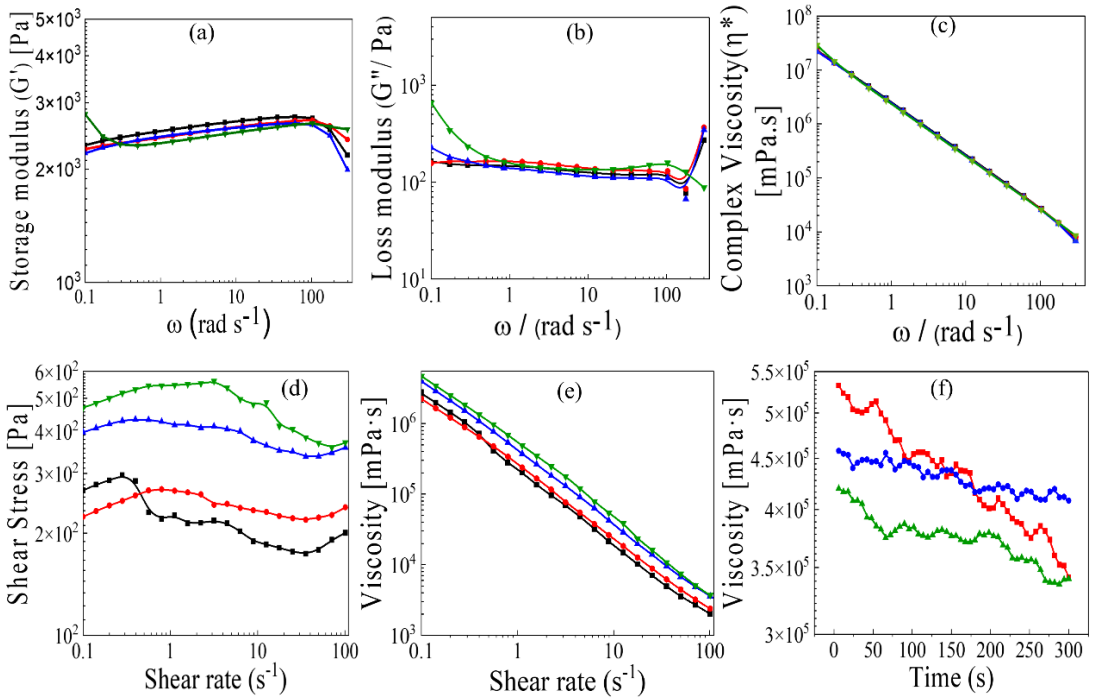

Figure 3.2. 3 (a-f) Rheological properties were measured at different temperatures, 34 ℃, 37 ℃, 40 ℃ and 43 ℃; (a) storage modulus vs. angular frequency, (b) loss modulus vs. angular frequency, and (c) complex viscosity (η) vs. angular frequency. (d) Change in shear stress vs. Shear rate at different temperatures, (e) viscosity (η) flow behavior of p(NAG-Ac-NAE) hydrogel as a function of shear rate (Ɣ) and (f) viscosity (η) as a function of time and temperature.*

Storage modulus (G') values were calculated to be varied from 2.3 kPa to 2.7 kPa at 0.1 to 100 rad sec^{-1} (Figure 3.2.3a) and loss modulus (G") varied from 0.12 kPa─0.16 kPa, at 0.1 to 100 rad sec^{-1}, respectively (Figure 3.2.3b) at the physiological temperature (37 ℃). At higher temperatures such as 40 ℃ and 43 ℃, the G' decreases and G" increases, due to the deformation of the hydrogel at higher angular frequency. This poly(NAG-Ac-NAE) hydrogel exhibits viscoelastic behavior with the increase in the storage modulus as the frequency increases up to 100 rad sec^{-1}. A similar trend is observed for complex viscosity (Figure 3.2.3c), such as with the increase in the frequency in all different temperature ranges which shows non-Newtonian behavior and shear thinning properties of poly(NAG-Ac-NAE) hydrogel.

An increase in the temperature shows higher viscosity and in relation to shear rate (Figure 3.2.3e) and time (Figure 3.2.3f) it decreases due to the shear thinning of the poly(NAG-Ac-

NAE) hydrogel. Shear thinning behavior allows injectability and possesses an advantageous role in drug delivery, cell encapsulation, granular hydrogel formation and in tissue engineering.[29] Shear stress vs. shear rate shows complex viscoelastic behavior of the hydrogel (Figure 3.2.3d) and at higher temperatures it decreases may be due to the deformation of network structure.

3.2.4.5. Cytocompatibility and Hemocompatibility of p(NAG-Ac-NAE).After the evaluation of physicochemical properties, the cytocompatibility of p(NAG-Ac-NAE) hydrogel were assessed by using healthy cell lines (Figure 3.2.4a), HUVEC cells (human umbilical vein endothelial cells), neural crest originated catecholamine cell line PC12, and using the different cancer cell lines such as MDA-MB-231, MCF7 and LN229 cells with the treatment of different concentrations of hydrogel (e.g., 10, 25, 50, 100, 250, 500 and 1000 μg mL^{-1}) for 24 h. At the dose of 200 μg mL^{-1} of p(NAG-Ac-NAE) hydrogel (Figure 3.2.4a) HUVEC cells are 100% viable while at a lower concentration of 5 μg mL^{-1} increased cell proliferation was observed to be 114 ± 0.07 %. In PC12 cells, the significant increase in cellular proliferation is found in response to the different concentrations of hydrogel with highest proliferation at the concentration of 250 μg mL^{-1} (152.7±13.7 %) ($p \sim 0.0024$) (Figure 3.2.4a). While with the treatment of p(NAE-Ac-NAG) hydrogel, minor decreased in cell viability with increase in concentration is in aggressive type cancer cells in the order of LN229>MDA-MB-231>MCF7 cells was observed and shown in Figure 3.2.4a. Furthermore, live-dead assays performed using acridine orange (AO) (green) and propidium iodide (PI) (red) on PC12 cells on day 5^{th}. The macroscopic images revealed the prolonged cell viability in treatment of p(NAE-Ac-NAG) hydrogel while normal apoptotic death was observed in some populations of reference control, as shown in Figure 3.2.4b. This, occurred due to the prolonged effect of p(NAE-Ac-NAG) on cell cycle stages. This cytotoxicity towards cancer cells revealed the non-tumorigenic activity of hydrogel,

while upto 20% the cytotoxicity is observed. On the other hand, this hydrogel favors cellular proliferation in PC12 cells. Furthermore, hemolysis studies were performed for its biologically safe use, with the hydrogel taking five different concentrations (62.5, 125, 250, 500, and 1000 μg mL^{-1}), the hemolysis percentages were observed for 8 hours are 0.36±0.13, 0.15±0.05, 0.96±0.7, 7.00±1.04 and 4.33±0.53, respectively and for 24 hrs. are found to be 1.90±0.21, 0.32±0.17, 4.68±0.14, 3.03±0.64 and 8.17±3.68 (Figure 3.2.4c). Above the concentration of 250 μg mL^{-1}, this hydrogel acts as a hemolytic material, while below this concentration it acts as a nonhemolytic material. Hence for future biological application p(NAG-Ac-NAE) hydrogel is limited to use at lower concentration. However, the observance of highest cell proliferation at 250 μg mL^{-1} revealed this material as hemocompatible and safe to use for therapeutic applications at lower concentrations. Then to evaluate the neurogenic potential of (NAE-Ac-NAG) hydrogel, primary neurons were cultured in the presence of p(NAE-Ac-NAG) and grew comparably healthy with mature neuronal structure. It was scrutinized on day 3^{rd} and 7^{th} which showed high cytocompatibility of p(NAE-Ac-NAG) towards the primary neuronal cells (Figure 3.2.4d, e). Furthermore, rhodamine phalloidin selectively labeled the F-actin of primary culture neurons as shown in Figure 3.2.4d, and revealed that the p(NAG-Ac-NAE) hydrogel promotes the cellular proliferation with the healthy network formation of actin filament,

which further confirmed very high stability of cytoskeleton network compared to the control group (on the Day 10th).

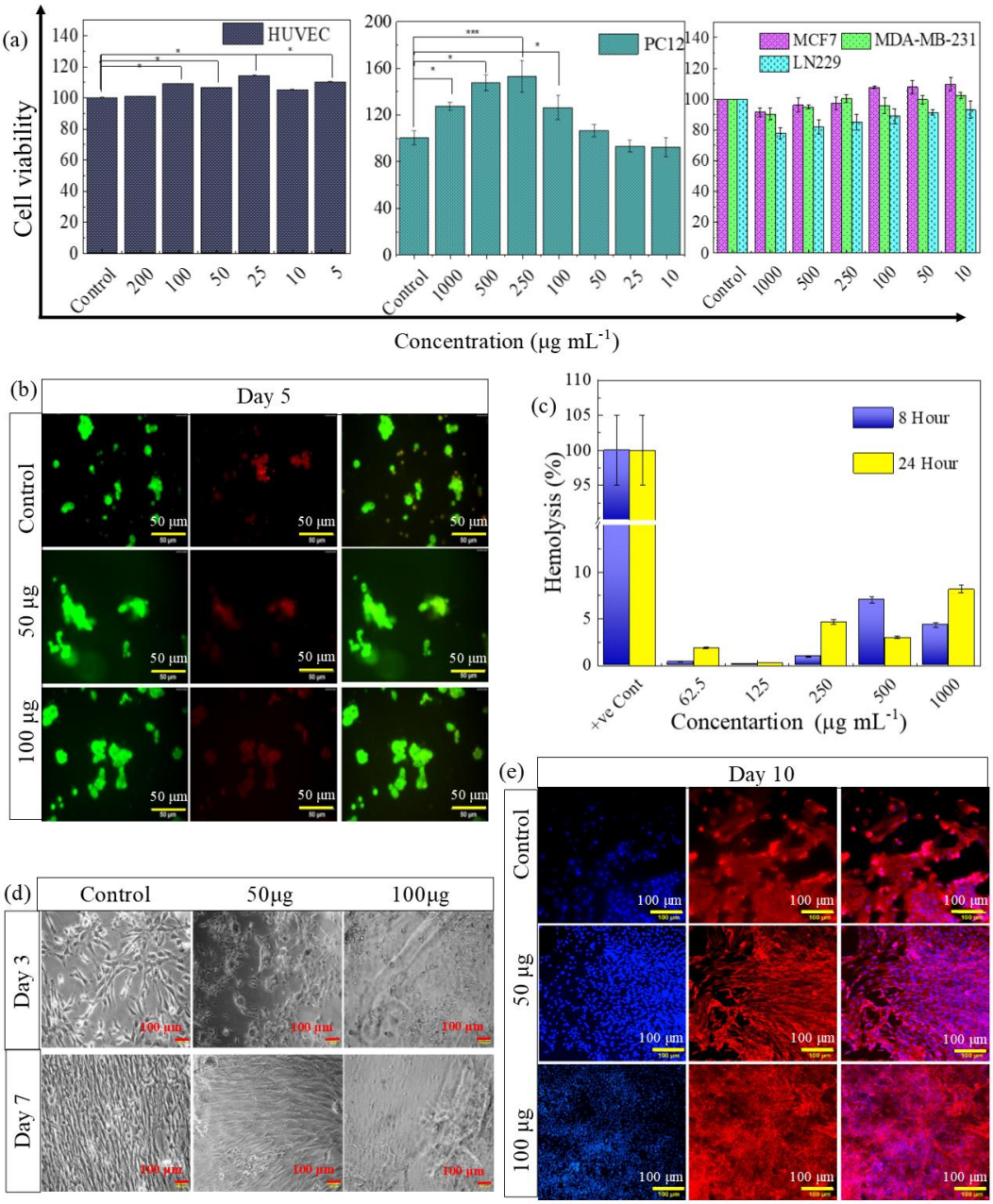

Figure 3.2. 4 Cytocompatibility and hemocompatibility of poly(NAG-Ac-NAE) co-polymeric hydrogel. (a) cell viability in HUVEC, PC12 and of cancer cell line LN229, MDA-MB-231 and MCF7 in presence of p(NAG-Ac-NAE) hydrogel. (b) Live/Dead (AO/PI stained) macroscopic images PC12 cells in treatment of p(NAG-Ac-NAE) hydrogel at concentration of 100 µg mL^{-1} and 250 µg mL^{-1} on day 5, (c) % hemolysis at different concentrations hydrogel (1000, 500, 250, 125 and 62.5 µg mL^{-1}) (d) Microscopy images of primary neuronal cells in treatment of p(NAG-Ac-NAE) hydrogel (50 and 100 µg mL^{-1}), and (e) cytoskeleton framework of primary neuron in presence of p(NAG-Ac-NAE) hydrogel of concentration 100 µg mL^{-1} and 250 µg mL^{-1}, (red–F-actin and blue- nucleus) only

3.2.4.6. p(NAG-Ac-NAE) hydrogel induced primary neurite outgrowth. The neurite outgrowth, substantial stability of cytoskeleton, and microtubule dynamics in-vitro study were performed on primary rat cortical neurons for different time intervals of 2, 7, 14, and 21 days. Through the confocal microscopy study, it is evident that at the concentration of 250 μg mL^{-1} of hydrogel (Figure 3.2.5a, on day 2, β-tubulin panel) initial differentiation of neuronal cells started along with the adhesion, while in the control group, only the cell adhesion is achieved. Furthermore, there is a significant increase in the cell population on treatment with 250 μg coated hydrogel within 2 days ($p \sim 0.00188$) compared to the control group (on day 2^{nd} and day 7^{th}) and p(NAG-Ac-NAE) hydrogel slice group ($p \sim 0.00349$) observed. The decrease in cell populations with an increase in differentiation, and the extent of neurite outgrowth is confirmed through the obtained increase in the green signal. β-Tubulin III expression from day 2^{nd} to 21^{st} is found to be continuously increased for p(NAG-Ac-NAE) hydrogel (in both hydrogel slice sample and 250 μg mL^{-1} coated hydrogel) compared to the control group, which confirmed the increase in Axonal path length with increase in time period. Among the three groups under study, the relative growth order of axonal path length is found to be: p(NAG-Ac-NAE) hydrogel (250μg coating) > p(NAG-Ac-NAE) hydrogel > control (Figure 3.2.5f) within 21 days.

From Figure 3.2.5g, a significant difference in the number of junctions is observed between day 2^{nd} and day 14^{th}. In p(NAG-Ac-NAE) hydrogel (250 μg coating slide), a maximum growth of neuron junction is calculated within day 7^{th} ($p \sim 0.00197$), compared to the control group and p(NAG-Ac-NAE)hydrogel. In the p(NAG-Ac-NAE) hydrogel slice, the highest number of junctions are formed on day 14 ($p \sim 0.0001$) and day 21^{st} ($p \sim 0.04$) compared to the control (Figure 3.2.5g). Thus, the increase in the number of junctions refers to the increase in the number of branches and synapses. Furthermore, a continuous increase in the

signal of F-actin from day 2nd – 21st is observed, signifying the growth and very high stability of the neuronal structure in hydrogel (Figure 3.2.5a-d).

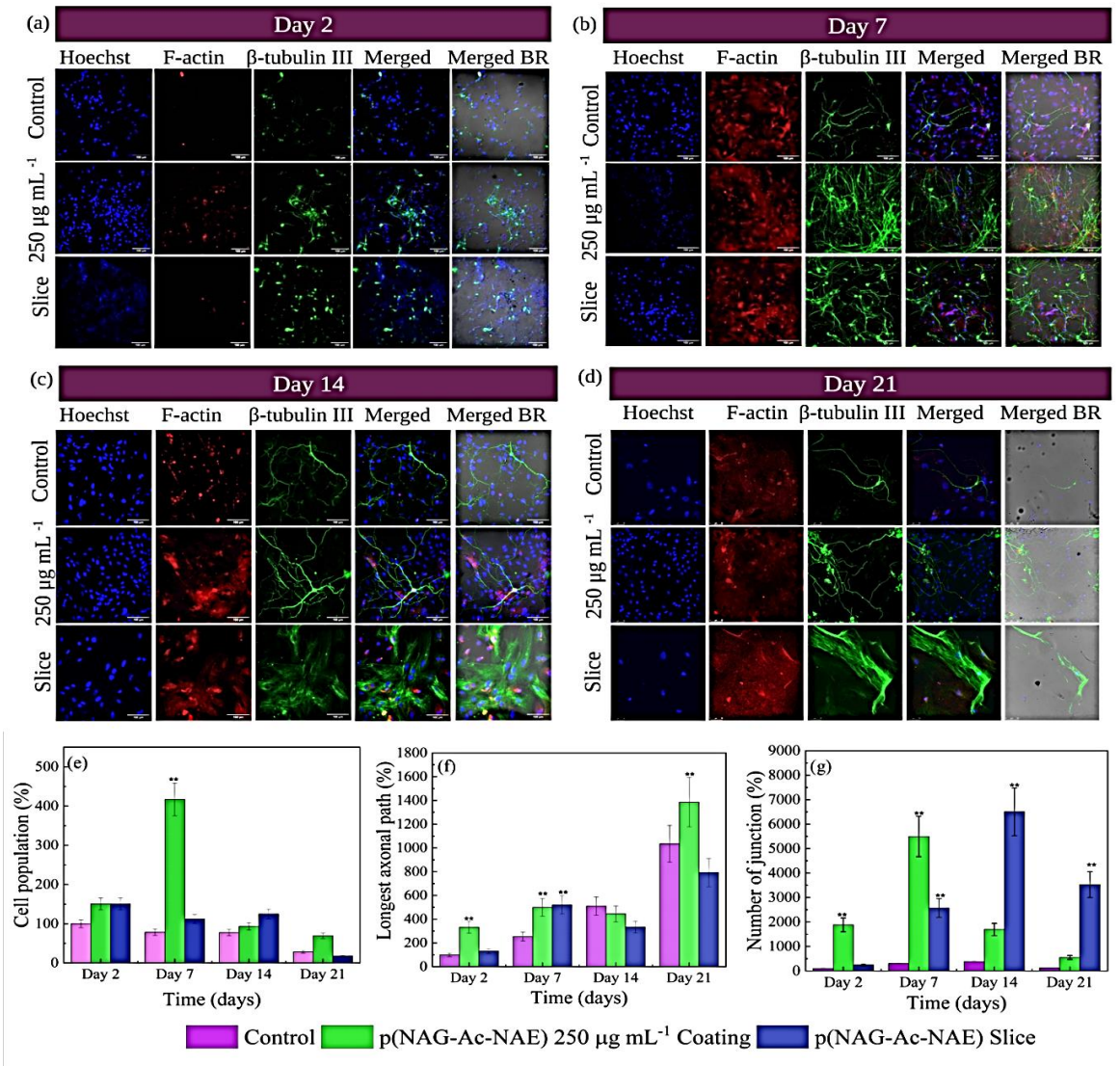

Figure 3.2. 5. Confocal microscopy images of neuron growth on 250 µg mL-1 nanohydrogel coated slide and a thin slice of poly(NAG-Ac-NAE) co-polymeric hydrogel. (a) Nature of cellular adhesion and growth on day 2nd. (b) Cellular differentiation and neurite extension on day 7th and (c) and (d) cellular differentiation and neurite extension on day 14th and day 21st, respectively on control, p(NAG-Ac-NAE) coated slide (250 µg mL-1) and sliced p(NAG-Ac-NAE) polymeric hydrogel. (e) Estimated increase in cell population at different intervals of culture (f) longest axonal path varied at different periods and (g) increased number of junctions (branching in neuron) changed at different periods. Hoechst 33258 (blue) stain represents the nucleus, immune-labelled β-tubulin III (green) shows neurite extension, and immune labelled with phalloidin (red) shows the F-actin.

Interestingly, in our previous report the highest growth was observed at 14th day[16] while in the present study, increased signal of axonal growth was observed within 7 days. This could be due the associated excitatory signal of glutamate. Thus, this finding confirms that the new hydrogel assists to increase in the neuronal growth in short period.

3.2.4.7. Neuroprotective role of p(NAG-Ac-NAE) hydrogel. Higher oxygen consumption in brain and presence of high polyunsaturated fatty acid content in neuronal membranes, leads the neuronal cells to become vulnerable to oxidative damage. Oxidative stress results in the accumulation of reactive oxygen species (ROS) that lead to lipid peroxidation, mitochondrial dysfunction, enhanced production, and migration of oxidized forms of α-synuclein as a consequence of neuronal cell death.[30, 31] H_2O_2 induced oxidative stress shows dose-dependent effect in various cells, like at 0.8-6 μM concentration cells remain healthy[31] at the intermediate concentration of 30 μM while membrane babbling occurred within 3 h of treatment[32] and at 24 h of treatment 50% of cells could survive, whereas at 50 μM concentration of H_2O_2, almost all the cells get lethal.[33] Hence, to mimic and analyze the probable outcome of p(NAG-Ac-NAE)hydrogel in pathological conditions, H_2O_2-induced stress was generated on PC12 cells by using different concentrations of 5 μM –160 μM of H_2O_2. In the previously report we have already shown the neuro-protective role of p(NAG-b-Ac) hydrogel, which was only glycine based hydrogel.[16] Furthermore, after modulation of p(NAG-b-Ac) hydrogel with glutamate, herein we have investigated the neuroprotective activity. Hence, we studied the p(NAG-Ac-NAE) hydrogel neuroprotective assay at lower concentration. Treatment with 250 μg mL^{-1} and 100 μg mL^{-1} of p(NAG-Ac-NAE) hydrogel in presence of oxidative stress (H_2O_2) shows the protective role. Similarly, with primary exposure to oxidative stress for 12 hrs. and removal of stress followed by the treatment with 250 μg mL^{-1} and 100 μg mL^{-1} of p(NAG-Ac-NAE) hydrogel reveled the recovery potential. It is noticed that almost

80-90 % of the cells become lethal at 80-160 µM concentration of H_2O_2, whereas 40-60 % of the cells are viable at 40 µM concentration of H_2O_2 (Figure 3.2.6a, b). It is also found that 250 µg mL^{-1} concentration of p(NAG-Ac-NAE) hydrogel, shows a substantial protective role (Figure 3.2.6a) up to 40 µM concentration of H_2O_2-induced oxidative stress (OS), whereas at lower stress conditions (40-20 µM H_2O_2 induced OS) the cell viability increased.

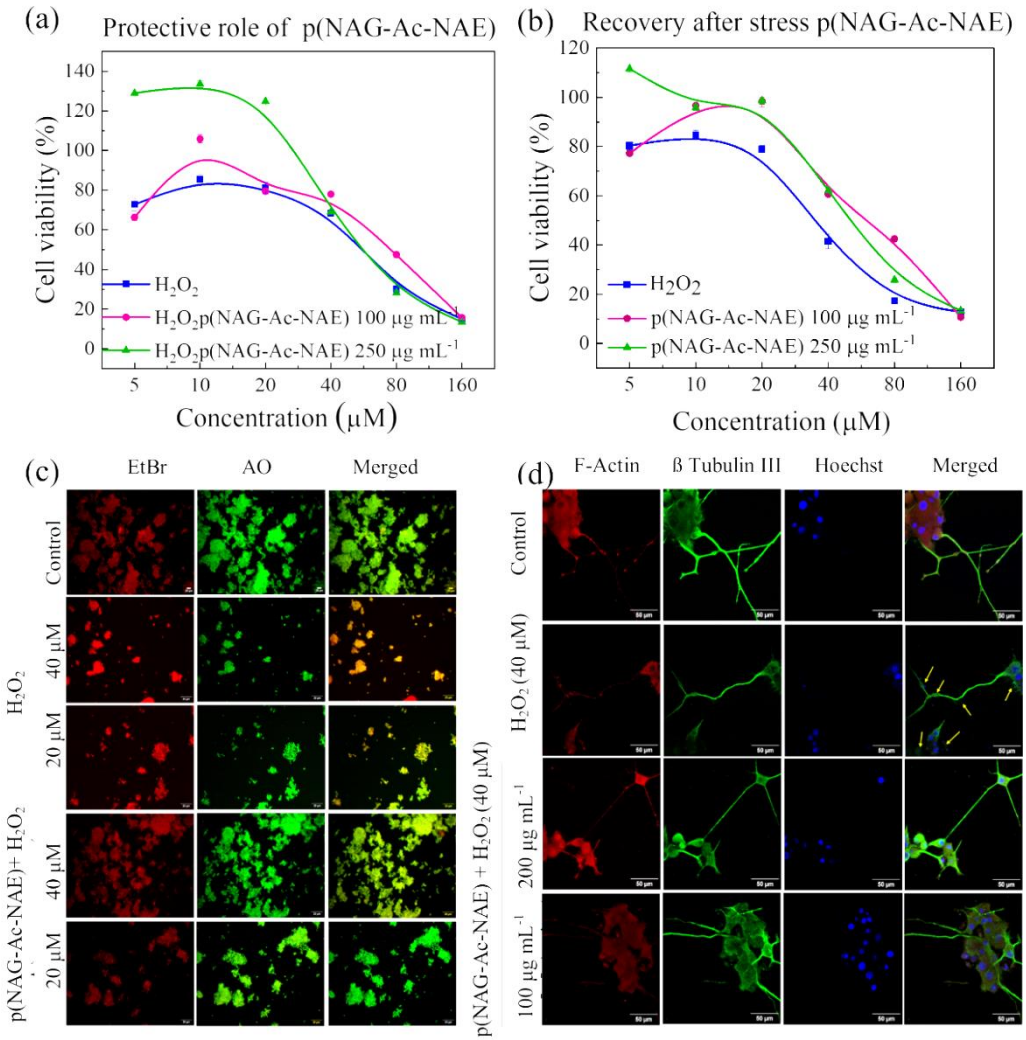

Figure 3.2. 6 Neuroprotective role of p(NAG-Ac-NAE) hydrogel. (a) Protective role of p(NAG-Ac-NAE) hydrogel in presence of different concentrations of H_2O_2, (c-d) stress-induced recovery status of PC12 cells using p(NAG-Ac-NAE)hydrogel after H_2O_2– induce stress, (e) Fluorescent microscopy images for the AO/EtBr stained PC12 cells at different conditions: untreated control, treated with H_2O_2 40 µM mL^{-1} and H_2O_2 20 µM in p(NAG-Ac-NAE) hydrogel in H_2O_2 40 µM., p(NAG-Ac-NAE) hydrogel in H_2O_2 20 µM and (f) cytoskeleton network stabilization by p(NAG-Ac-NAE) hydrogel and in the presence of 40 µM mL^{-1} H_2O_2 induced OS at highest proliferative concentration of 250 µg mL^{-1} hydrogel, respectively which further confirmed by cell cycle analysis.

Furthermore, this finding can be corroborated with the acridine orange (AO) and ethidium bromide (EtBr) staining of PC12 cells after 12 h of incubation in control, in a (20 µM and 40 µM) H_2O_2 induced oxidative stress condition and in presence of 100 µg mL^{-1} of p(NAG-Ac-NAE)hydrogel, (Figure 3.2.6c, d). It is noticed that the maximum cells are passing through the apoptotic cell death in order of 40 µM > 20 µM concentration of H_2O_2-induced OS conditions. Differentiated PC12 cells in OS condition cause the arrest of neurite outgrowth, damage in axonal terminals, shortening of neurite, nuclear damage and decrease in F-actin (Figure 3.2.6d) compared to the standard control. While p(NAG-Ac-NAE) neutralizes the OS, promotes intact neuronal structure with thicker neurite, prominent axonal terminal, and increased signal for F-actin along with intact nucleus. Effect of p(NAG-Ac-NAE) in Cell Cycle. In control, 55.01% cells are in G0/G1 phase, 10.18% in S phase and 10.59% in G2/M phase and 22.80% are in sub-G1 phase when cells are cultured for 24 h. Sub-G1 phase shows the degraded DNA fragments as evidence of apoptosis[34] Figure 3.2.7.

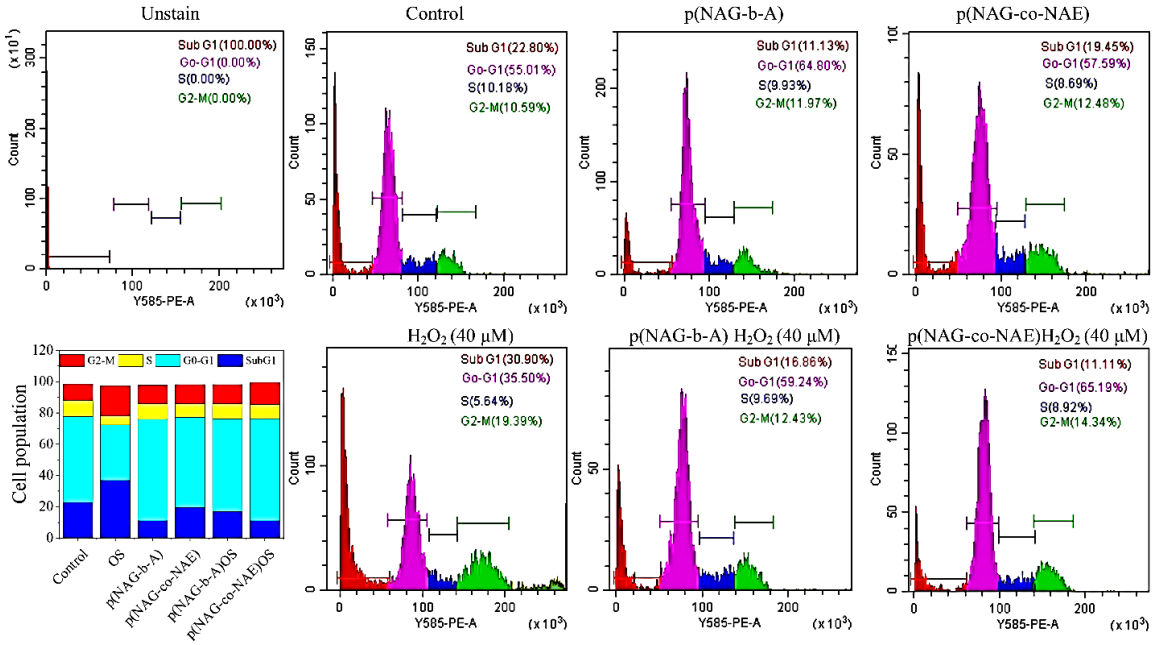

Figure 3.2. 7 Stress mitigating effect analysis through cell cycle analysis. DNA content detected by flow cytometry in treatment of p(NAG-b-Ac), p(NAG-Ac-NAE), H_2O_2, H_2O_2 along with p(NAG-b-Ac) and H_2O_2 along p(NAG-Ac-NAE) hydrogel.

In previous study we have reported about neuroprotective activity[16]. Furthermore, in this work we have revealed that the p(NAG-b-Ac) increases in G0/G1and G2/M phase to a higher extent with a 50% decrease in sub-G1 phase in contrast to control Figure 3.2.7. However, p(NAG-Ac-NAE) hydrogel only increase the G0/G1and G2/M slightly decrease in sub-G1 phase. 40 μM of H_2O_2 treatment induced the sub-G1 phase (30.9%) and reduction G0/G1 phase represents the induced apoptosis. In treatment with p(NAG-Ac-NAE) and p(NAG-b-Ac), they reduced the cell population of sub-G1 phase and also in presence of H_2O_2 stress, and cellular proliferation were revealed with increase in the cell numbers at G0/G1 phase. This results revealed the stress mitigating effect of p(NAG-Ac-NAE) and p(NAG-b-Ac) hydrogel.

3.2.4.8. Comparative ROS Mitigating Effect of p(NAG-Ac-NAE) and p(NAG-b-Ac) Hydrogel. A critical level of ROS is essential to meet the high demand of ATP for normal physiological response. However, dysfunctioning in mitochondrial machinery, exaggerated ROS production, and alteration in mitochondrial metabolism lead to the neurological condition. Mitochondrial membrane potential (ΔΨM) is a central intermediate in oxidative energy metabolism,[35] and cationic dye Rhodamine 123 accumulates in the mitochondrial inner membrane, decay in fluorescence is proportional to the mitochondrial membrane potential depolarization. Furthermore, to elucidate the exact mechanism in neurogenesis and neuroprotection effect of p(NAG-Ac-NAE), mitochondrial depolarization and ROS generation was evaluated. The treatment of PC 12 with p(NAG-Ac-NAE) doesn't show any affect the mitochondrial polarization, while minimum depolarization is observed with p(NAG-b-Ac) hydrogel. As stated in Figure 3.2.8, H_2O_2 induce apoptosis is observed due to the depolarization of the mitochondria in dose dependent manner (reduces the fluorescence intensity; Figure 3.2.8a). This increase in

depolarization is reduced by the treatment with p(NAG-Ac-NAE) and p(NAG-b-Ac) hydrogel. Interestingly, At the exposure of the 20 μM H_2O_2 then treatment with p(NAG-b-Ac) hydrogel, MMP is almost equal to the control. With exposure of 20 μM and 40 μM H_2O_2 and treatment with p(NAG-Ac-NAE) hydrogel, an increase in fluorescence intensity ratios were observed similar to the 20 μM H_2O_2 treatment group. Earlier, it has been reported that 20 μM H_2O_2 express preconditioning effect and suppress the apoptosis.[36, 37]. This phenomenon is clearly shown by our results where exposure of 20 μM and 40 μM H_2O_2 then treated with p(NAG-Ac-NAE) hydrogel, the fluorescence intensity increased equivalent to 20 μM H_2O_2 treatment. These results are comparable with Figure 3.2.7, where reduction in sub-G1 phase has been observed which corroborated the mitigating effect of p(NAG-Ac-NAE). The percentage of ROS-producing cells in normal control (untreated PC12 cell) is found to be less by 33.72% (Figure 3.2.8b.1), while for treatment with 20 μM (Figure 3.2.8b2) and 40 μM H_2O_2 (Figure 3.2.8b3) was found to be increased in ROS up to 42.33% and 52.49%, respectively. After treatment with p(NAG-Ac-NAE) (Figure 3.2.8b.4) and p(NAG-b-Ac) (Figure 3.2.8b.7) hydrogel, intracellular ROS is found to be equivalent to the control. The PC12 cells were cultured in the presence of p(NAG-Ac-NAE), p(NAG-b-Ac) hydrogel and exposed to 20 μM and 40 μM of H_2O_2 for 24 hrs separately. Intracellular ROS scavenging effects were observed more in treated groups compared to the only OS group. ROS scavenging effect is observed higher in p(NAG-b-Ac) hydrogel compared to the p(NAG-Ac-NAE) hydrogel with the difference in value of 5.67% and 13.88% for p(NAG-b-Ac) hydrogel and 3.49% and 13.38% for p(NAG-Ac-NAE) hydrogel to the respective concentration of 20 μM and 40 μM of H_2O_2, respectively. These results revealed that the p(NAG-Ac-NAE) and p(NAG-b-Ac) hydrogel reduce the depolarization state of PC12 cells in oxidative stress conditions and provide the preconditioning effect for survival, proliferation and differentiation of the PC12 cells.

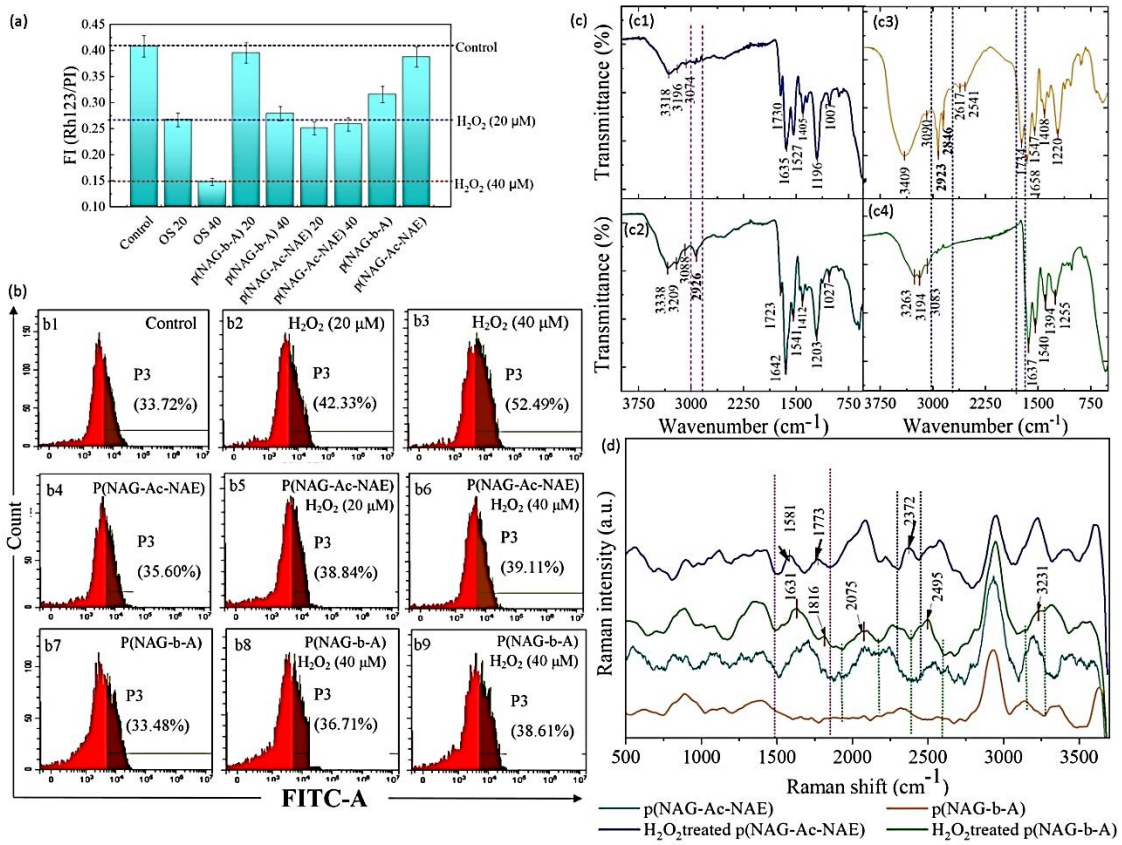

Figure 3.2. 8 Represents the effect of p(NAG-Ac-NAE) hydrogel and p(NAG-b-Ac) hydrogel on mitochondrial membrane potential and on intracellular ROS production in PC12 cells. (a) reduction of mitochondrial membrane potential depolarization observed in H_2O_2 oxidative stress by p(NAG-Ac-NAE)hydrogel and p(NAG-b-Ac) hydrogel, (b) Flow cytometry detection of intracellular ROS in PC12 cells: (b1) untreated control, (b2) exposure of H_2O_2 20 μM (b3) exposure of H_2O_2 40 μM, (b4) treatment with p(NAG-Ac-NAE)hydrogel, (b5) exposure of H_2O_2 20 μM treatment with p(NAG-Ac-NAE)hydrogel, (b6) exposure of H_2O_2 40 μM treatment with p(NAG-Ac-NAE)hydrogel, (b7) treatment with p(NAG-b-Ac) hydrogel, (b8) exposure of H_2O_2 20 μM and treatment with p(NAG-b-Ac) hydrogel and (b9) exposure of H_2O_2 40 μM and treatment with p(NAG-b-Ac) hydrogel. (c) FTIR spectrum of (c1 and c2) H_2O_2 treated and without treated p(NAG-Ac-NAE) hydrogel, (b) H_2O_2 without treated and treated p(NAG-b-Ac) hydrogel, and (c) Raman spectrum at different treatment conditions.

Furthermore, to elucidate the mechanism involved behind the protective role of p(NAG-Ac-NAE)and p(NAG-b-Ac) hydrogels, we have immersed treated hydrogel with 40 μM of H_2O_2 for 24 hours followed for Raman spectroscopy and FTIR analysis (Figure 3.2.8c). FTIR spectrum of H_2O_2 treated p(NAG-Ac-NAE) (Figure 3.2.8c1) and H_2O_2 treated p(NAG-b-Ac) (Figure 3.2.8c4) hydrogel revealed that the alkane (2923 cm^{-1}) has been

disappeared in both the groups. While in H_2O_2 treated p(NAG-b-Ac) hydrogel additional C═O (1734 cm^{-1}) bands are disappeared. Furthermore, from the Raman spectroscopic analysis (Figure 3.2.8d), the common bands in all H_2O_2 treated and untreated p(NAG-b-Ac) and p(NAG-Ac-NAE) hydrogel have appeared as 2946 cm^{-1} for CH_2 stretching, and 3139 cm^{-1} of NH of p(NAG-b-Ac) shifted to 3224 cm^{-1} (NH) in p(NAG-Ac-NAE). However, in H_2O_2-treated p(NAG-b-Ac) hydrogel, an additional Raman band is observed at 1622 cm^{-1} due to the presence of amide bonds. While in H_2O_2 treated p(NAG-Ac-NAE), a band at 2364 cm^{-1} is observed due to the formation of C≡C. This observation shows that when hydrogel comes in contact with H_2O_2, it triggers the release of CO_2 and H_2O molecules as by-products and degradation of polymer chains occurred. Same have been confirmed as a few bands are disappeared and few of them are shifted.

3.2.4.9. Angiogenesis stimulatory effect of p(NAG-Ac-NAE) hydrogel. Angiogenesis plays an important role in the functional recovery of neurovascular units in traumatic, ischemic and pathological conditions of the brain. Neuronal progenitor cells (NPCs) are present in close proximity with blood vessels, which provide guidance to NPCs[38] for neurogenesis. With the aim to develop dual properties bearing angiogenesis/ neurogenesis imprinted hydrogel both previously reported p(NAG-b-Ac)[16] and presently synthesized p(NAG-Ac-NAE)hydrogels were examined for angiogenic potential. p(NAG-Ac-NAE) hydrogel is composed of a combination of glycine (inhibitory) and glutamate (excitatory) units, while p(NAG-b-Ac) hydrogel is an only inhibitory glycine-containing polymer, both polymers are cytocompatible and increased the cell proliferation of HUVEC cells at low concentration of treatment (Figure SS3.2.8a)). Furthermore, a chick embryo assay was performed for p(NAG-Ac-NAE) hydrogel and p(NAG-b-Ac) hydrogel to analyze vascular sprouting. The chick embryo was incubated with 1 μg mL^{-1}, 25 μg mL^{-1} and 100 μg mL^{-1} of p(NAG-Ac-NAE) hydrogel for 0 h and 8 h, which showed the mature

prominent blood vessel formation (Figure 3.2.9a, the mature blood vessels represented by arrow). Furthermore, the acquired images were analyzed for vessel area, junction density, total number of junctions and total vessel length by using the Angiotool software and the results are shown in Figure 3.2.9b-e. Vessel area (Figure 3.2.9b) significantly increased by 18% ($p \sim 0.03$) and 20% ($p \sim 0.047$) within 2 h for 25 μg mL^{-1} of dose and total vessel length (Figure 3.2.9d) by 39% ($p \sim 0.006$) and 7.5% ($p \sim 0.044$)) within 8 h in response to 1 μg mL^{-1} of the dose applied, respectively. A total number of junctions significantly increased from 10.2% ($p \sim 0.024$) to 46.2% ($p \sim 0.005$) within 2 h to 8h as μg mL^{-1} hydrogel dose was used, respectively. Thus, the total number of junctions (Figure 3.2.9e) and junction density (Figure 3.2.9c) are significantly increased as the hydrogel dose increased from 1 μg mL^{-1} ($p \sim 0.005$ and 0.01, respectively) to 25 μg mL^{-1} ($p \sim 0.02$ and 0.006, respectively). In conclusion, p(NAG-Ac-NAE) hydrogel shows pro-angiogenic behavior at low doses such as 1 μg mL^{-1} and 25 μg mL^{-1} of hydrogel. Further, a similar CEA assay was performed using p(NAG-b-Ac) hydrogel at the lowest dose of 1 μg mL-1 for 0 h, 2 h, 4 h and 8 h. As per the quantitative assessment, significant decreases in vessel area, total number of junctions, junction density and total vessel length have been observed within 4 and 8 hours as shown in Figure S3.2.8 (a-d). The vessel area (Figure S3.2.8a) significantly is found to be decreased by 36.74% ($p \sim 0.02$) and 38.61% ($p \sim 0.02$); total number of junctions (Figure S3.2.8b) decreased by 65.88% ($p \sim 0.004$) and 70.87% ($p \sim 0.006$), junction density (Figure S3.2.8c) decreased by 64.56% ($p \sim 0.003$) and 63.12%($p \sim 0.005$), and total vessel length increased by (Figure S3.2.8d) by 30.24 % ($p \sim 0.01$) and 31.37 % ($p \sim 0.02$); at 4 and 8 hrs., respectively. These results are clear shreds of evidence that the p(NAG-Ac-NAE) hydrogel is angiogenic, while p(NAG-b-Ac) hydrogel is anti-angiogenic in nature. These results indicate that the angiogenic potential could arise due to the presence of excitatory

neurotransmitter glutamate imprinting. Therefore, the cytocompatibility and neurogenic potential were analyzed for only p(NAG-Ac-NAE) hydrogel.

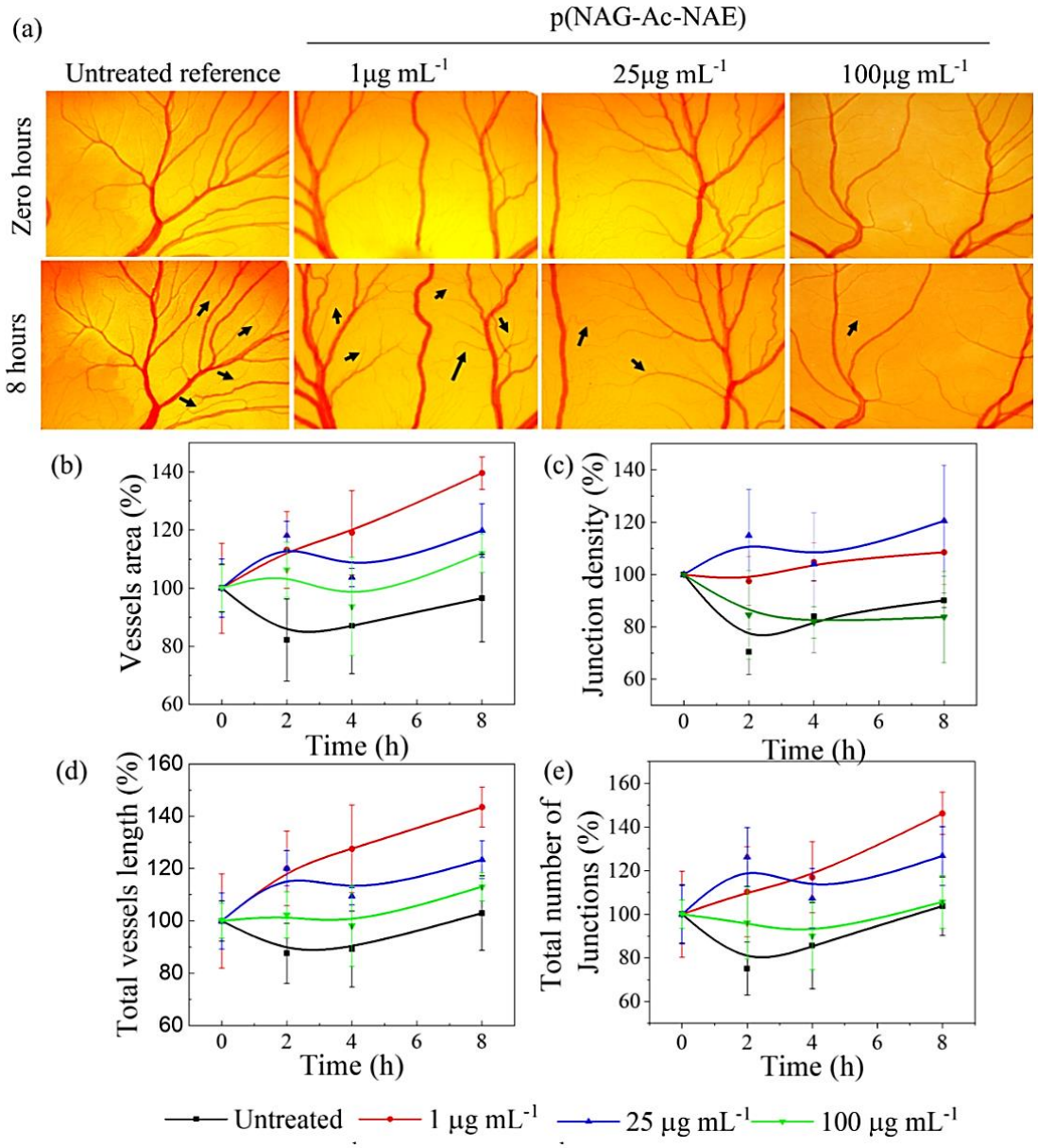

*Figure 3.2. 9 Angiogenic stimulatory effect of p(NAG-Ac-NAE) hydrogel. (a) In ovo CEA assay in the presence of p(NAG-Ac-NAE) enhanced the vascular sprouting (marked as a black arrow) in dose dependent manner. (b-e) show the change in several angiogenic parameters, such as blood vessel area, the total number of junctions, junctions density and total vessel length obtained in time-dependent (statistical significance level of *p<0.05).*

3.2.4.10. Effect of Hydrogel on Gene Expression Analysis. Furthermore, in the current study, we leveraged a p(NAG-Ac-NAE) hydrogel effect on molecular events of neurogenesis and angiogenesis under oxidative conditions. The first finding in the discovery of the hypoxia-inducible factor that indicated the formation of new neurons. Hypoxia-induced factor -1α (HIF1α) expression affects the several downstream target genes like VEGF, nitric oxide synthase, IGF. While HIF1α negative effect by triggering the expression of endothelin-1 (ET-1) and brain natriuretic peptide (BNP) in controlled manner to exercise preconditioning effect in ischemia.[39] Low dose of H_2O_2 10-20 μM concentration can up regulate the HIF1α expression thereby mediate the preconditioning protection in ischemic brain[40] and also protect PC12 cell against dopamine induce apoptosis.[41] Our results corroborated with this finding as H_2O_2 treatment with 20 μM induce the expression of HIF1α, while at the 40 μM the HIF1α expression is diminished. With treatment using both the p(NAG-Ac-NAE) and p(NAG-b-Ac) hydrogels, induced expression of HIF1α is observed. Interestingly, as alone 40 μM H_2O_2, complete diminish expression of HIF1α is observed, while the induced expression is observed with treatment of p(NAG-Ac-NAE) and p(NAG-b-Ac) along with 40 μM H_2O_2, which confirm the HIF1α mediated precondition effect of both the hydrogel even in higher oxidative stress (Figure10). And this could be the wherein cell cycle we observed the decreased sub-G0 phase (Figure7). It is known that HIF 1α cross talk with the VEGF and induce the expression of VEGF by interaction HIF 1α to HRE the promoter region of VEGF gene. Furthermore, VEGF guides neuronal migration in the embryonic brain and supports axonal and arterial co-patterning and formation of micro vessels. In PC12 cells we observed almost similar expression in presence/absence of both the hydrogel in oxidative stress or normal condition. However, the increase expression for VEGF isoform observed in treatment of p(NAG-Ac-NAE) hydrogel at concentrations of 25 and 250 μg mL^{-1}, even in presence of

oxidative stress. However, p(NAG-b-Ac) hydrogel induce the expression of VEGF isoform at only concentration of 25μg mL^{-1} of hydrogel but not at the 250 μg mL^{-1} of hydrogel, even in the presence of oxidative stress (Figure10) and KDR has high affinity towards the VEGF isoforms. Increased KDR expression is related with recurrent depressive disorder.[42] We observed the increased expression of KDR in presence of H_2O_2 with the increase in the concentration from 20μM to 40 μM. Treatment with p(NAG-b-Ac) doesn't affect KDR expression. However, while treated with p(NAG-Ac-NAE), it slightly decreases the expression of KDR. However, the increased expression of hydrogel along with H_2O_2 treatment increase the expression of KDR equivalent to the expression induced by 20 μM of H_2O_2. The overexpressed KDR in treatment with 40 μM of H_2O_2 revealed excessively stressed condition of PC12 and requirement of external supplied growth factor to reduce the oxidative stress. With the decreased expression of KDR even in oxidative stress, we can consider that p(NAG-Ac-NAE) hydrogel could prevent the neuronal cell from further damage and may also prevent the recurrent depressive disorder. Furthermore, to validate the VEGF stimulatory effect of p(NAG-Ac-NAE) and p(NAG-b-Ac) hydrogel, RAW264.7 cell was treated with both the hydrogel. We observed in treatment with p(NAG-b-Ac) hydrogel at 25 μg concentration 0.2-fold increase in expression while treatment with 250 μg mL^{-1} concentration 0.4 folds decreased in expression is observed. However, with the treatment with p(NAG-Ac-NAE) hydrogel, 00.3 and 0.6 folds increased in VEGF expression is observed at 25 and 250μg mL^{-1} of hydrogel (Figure 3.2.5). p(NAG-b-Ac) hydrogel induce the overexpression of TNFα, 7 folds at 25 and 3.5 folds at 250 μg mL^{-1} while p(NAG-Ac-NAE) hydrogel shows on 1-fold increase in TNFα at 25 μg mL^{-1}, while decrease in expression at 250 μg mL^{-1} is observed. TNFα is a pro-inflammatory cytokine which regulates the homeostatic function in neurogenesis, myelination and in synaptic plasticity. [43]

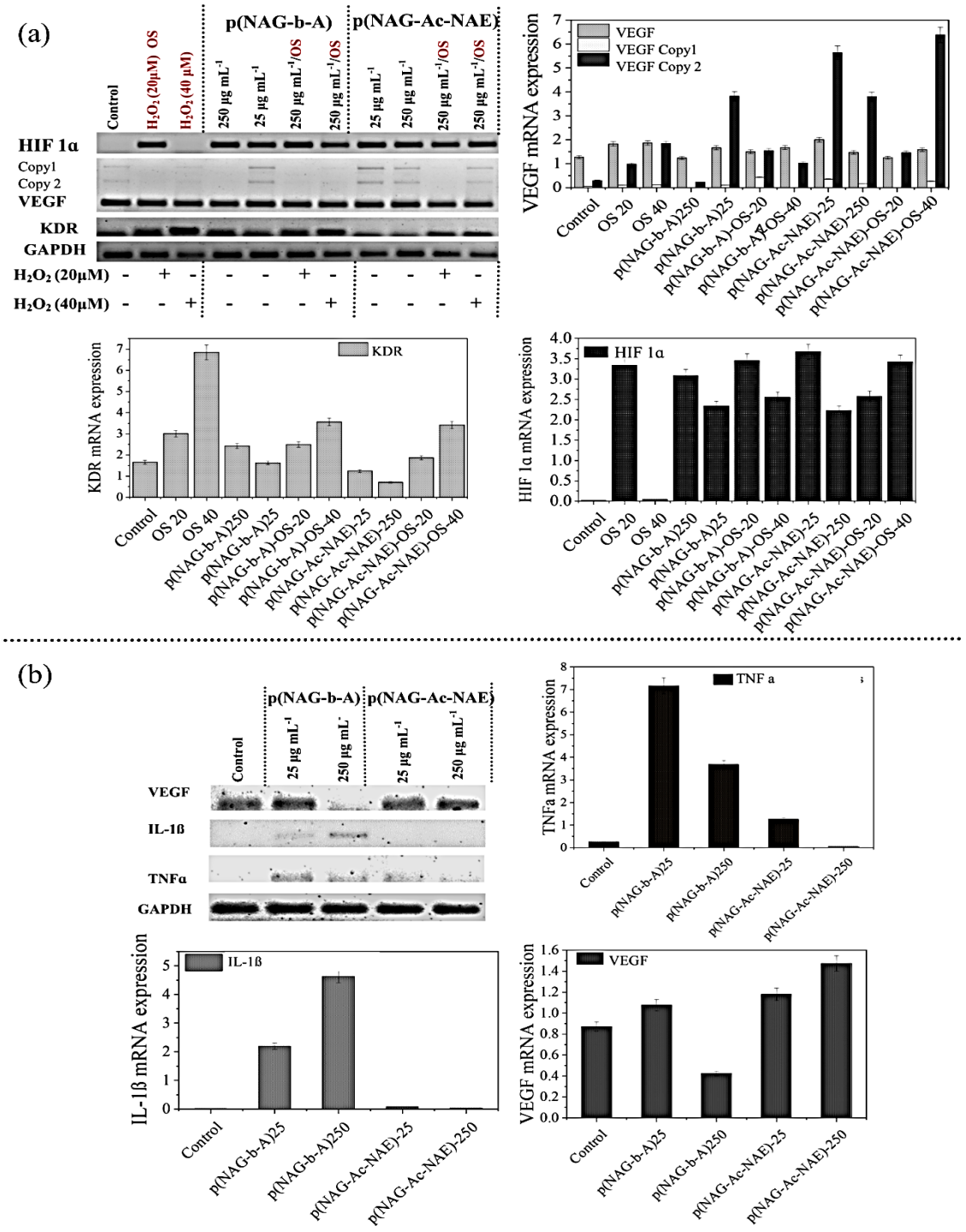

Figure 3.2. 10 Figure 3.2.10. Figure 3.2.9 (a) Change in HIF 1a, VEGF and KDR mRNA expression in treatment of p(NAG-b-A) and p(NAG-Ac-NAE) in presence and in absence of H2O2 induce oxidative stress at 20μM and 40μM concentrations against PC12 cells. After sqRT-PCR, the amplicon was separated on 2% agarose gel. Densitometry analysis were performed using FIJI software represented in graph. Figure (b). Change in VEGFa, IL1-ß, and TNFa mRNA expression in treatment of p(NAG-b-A) and p(NAG-Ac-NAE) at 25 and 250 μg mL-1 in RAW264.7 cells. After sqRT-PCR, the amplicon was separated on 2% agarose gel. Densitometry analysis was performed using FIJI software and represented in graphs.

However, its expression also correlated with initiation of degenerative cascades after peripheral nerve injury. In our previous study we have not investigated the effect of p(NAG-b-Ac) hydrogel on neurogenesis. As per present investigation p(NAG-b-Ac) hydrogel shows the induction of pro-inflammatory cascades, which raises the question of how p(NAG-b-Ac) hydrogel induces the neurogenesis. With the current fold expression of TNFα, we can conclude that the p(NAG-b-Ac) hydrogel shows the dose dependent inflammatory activity, i.e., with increase in hydrogel concentration, one-fold decrease in expression is observed. In the previous study, we majorly used 500 μg mL^{-1} of p(NAG-b-Ac) hydrogel[16] and that could be the region for neurogenesis and astrocytes like morphology was observed. In present study, we can consider that the p(NAG-Ac-NAE) hydrogel is more effective even in a lower concentration, only one fold TNFα expression is observed, while with increase in concentration a diminished TNFα expression is observed. Furthermore, p(NAG-b-Ac) hydrogel induces the IL1ß expression while p(NAG-Ac-NAE) hydrogel does not show any effect on IL1ß. From these results we can conclude that the p(NAG-b-Ac) hydrogel is pro-inflammatory while the p(NAG-Ac-NAE) hydrogel doesn't effect on the pro-inflammatory cascade. Further, p(NAG-Ac-NAE) hydrogel induces the angiogenic, neurogenic and neuroprotective effect via HIF1α/VEGF/KDR cascade.

3.2.5. **DISCUSSION.**

Understanding the role of glutamic acid and glycine in neurogenesis reveals the development of CNS regenerative medicine. The wide distribution of excitatory glutamate and inhibitory glycine neurotransmitters was observed in the nerve cells, astrocytes, as well as in glial cells and disruptions of balance are responsible for the pathophysiology. [44]Glycine influences cellular events[45] and plays a ubiquitous role in neuronal stem cell survival and neuroprotection.[46, 47] The most abundant

excitatory glutamate neurotransmitter maintains neuronal homeostasis and is involved in synaptic plasticity, in learning and memory. [48] Deregulation in glutamate, spreading depolarization and glutamatergic signaling can relate to neurological and psychiatric disorders, especially epilepsy. [49] [50] targeting glutamatergic signalling is useful in promoting regeneration/repair and pain management. [51] Existing antidepressant drugs work on the release of glutamate as it blocks the N-methyl-D-aspartate (NMDA) and bursts glutamate release. Hence, Glutamate neurotransmitter-based treatment reverses the stress-induced behaviour, molecular and structural discrepancies of MD. As per the mechanism, the burst release of glutamate induces depolarization of cell and depolarized cells release the brain-derived neurotrophic factor (BDNF). [52] This BDNF, induces the synthesis of synaptic proteins, maintains the synaptic functions via activating the mTORC1 and influences the neuroprotective pathways and neurogenesis (Figure 10). [53] With the aim of development of pro-angiogenic and neurogenic properties the imprinted p(NAG-Ac-NAE) hydrogel was synthesized via free radical, mini-emulsion polymerization (see Scheme 1 and Figure 3.2.1) technique. Ultra sonication process was applied for the formation of mini-emulsion as well as to achieve nanosized particles. Polyalkene functionalized monomers serve the role of the formation of stable polymer particles. [54] In the polymerization process AIBN acts as an initiator and DVB is used as a cross-linker which helps stabilize the polymer particles. Incorporation of amino acids inside the chains serves an important role in the formation of narrower molecular weight distributed polymer which has several beneficial properties like hydrophilicity, biocompatibility, stimuli responsiveness and chiral recognition. This hydrogel is mechanically soft and stable (Figure 3a-f), with high swelling properties (Figure 3.2.2a), biodegradable (Figure

3.2.2b) and cytocompatible in nature (Figure 3.2.4). High swelling capacities and higher branched have been induced by incorporating the DVB, which creates micropores of size 2 ± 0.5 nm in diameter (Figure 3.2.1c, g). The high swelling behaviour of this hydrogel further provides the capability of this hydrogel to improve the microenvironment to favor the neuronal cells for cellular adhesion and viability. Further, pH-responsive behaviour of p(NAG-Ac-NAE) hydrogel (Figure 3.2.2a) can be an advantage for drug delivery and for the treatment of neurodegenerative diseases, since the pH is a biomarker of neurodegenerative diseases as the cerebral pH is significantly higher in disease condition. [55] Conductive polymers, either with or without external electrical stimulation direct the electrochemical stimulation to the cells, enhance the cellular functions and also activate the gene expression of nerve growth factor in comparison to the nonconductive materials. [56] Compared to the non-conducting collagen films, semiconducting ($7.00 \pm 1.10 \times 10{-}5$ S cm^{-1}) (Figure S3.2.7) melanin thin film enhanced the Schwann cell growth and neurite extension. [57] The p(NAG-Ac-NAE) hydrogel used in this work shows semiconducting behaviour like melanin thin film (Figure S3.2.7) which shows the one advantageous feature of this hydrogel over the existing hydrogel. The p(NAG-Ac-NAE) hydrogel used in this work has elastic modulus values of 2.3 kPa to 2.7 kPa (Figure 3.2.3a). Soft biomaterial having a modulus value below 1 kPa favours neuronal differentiation, 1 kPa - 3 kPa favours astrocyte differentiation, [58] and modulus of 2 kPa can increase the differentiation of immature to mature neurons. [59] The major focus of the work is to develop angiogenic potential possessing material as it is mentioned earlier. Not only p(NAG-Ac-NAE) hydrogel have shown pro-angiogenic activity at a lower concentration of 2.5-25 μg mL^{-1} (Figure 3.2.10) compared to the only glycine-containing p(NAG-b-A) hydrogel (Figure S3.2.8) but

also increased cellular proliferation of PC12 cells (Figure 3.2.4a). These enhanced cellular proliferation and differentiation occurred due to the influence of chiral amino acid (L-glutamic acid). As reported by Dou et al., cellular differentiation depends on chirality, such as L-amino acid can influence cellular proliferation, spreading and differentiation whereas, D-amino acid suppresses this behavior. [60] Intracellular ROS generation increases the Bcl-2/Bax ratio which leads to the apoptosis in a dose-dependent manner. Low concentration of H_2O_2, decreases the level of Bcl-2/Bax ratio and provides the preconditioning effect to MSCs. this preconditioned MSCs upregulates the phosphorylated Akt-1 expression followed by increasing the HIF1α expression. This increase in HIF-1α upregulates the VEGF expression followed by the angiogenesis (Figure 10). [36] [37] [37] Furthermore, in the present study, stress generated using H_2O_2 (at 5 μM) doesn't show any cytoprotection as shown in Fig 6a and Fig. 5d. The use of 10-20 μM H_2O_2, influences the ROS generation (Figure 3.2.8b.2 and b.3) and increase in the HIF 1α expression is observed (Figure 3.2.10). However, at the higher concentration of H_2O_2 (at 40 μM), it induces cytotoxicity in PC12 cells and it is observed as completely diminished HIF-1α expression with high level of ROS and induced apoptosis, which corroborates the increased sub-G0 phase of the cell cycle. [61] Similarly, in the presence of 5-20 μM H_2O_2 along with p(NAG-Ac-NAE) hydrogel, it shows a 45% increase in cell viability compared to the used H_2O_2 oxidative stress only, while at 40 μM H_2O_2 exposure under treatment with p(NAG-Ac-NAE) hydrogel has significantly higher cell survival (Figure 3.2.7a). This increase in cellular viability is observed due to the influence of both the hydrogel in cell cycle, where it reduced the sub-G1 phase and induction in G0/G1 (Figure 3.2.7) occurred followed by reduction in apoptosis. This is one of the crucial points in diseased conditions where most of

the cells undergo death. Thus, the p(NAG-Ac-NAE) hydrogel not only influences the apoptosis but also due to the induced G0/G1 phase, it is responsible for the recovery of PC12 H_2O_2 pre-treated cells. Therefore, we can accelerate the recovery status of PC12 cells assisted by the p(NAG-Ac-NAE) hydrogel even after sufficient oxidative stress was applied as shown in Figure 3.2.6b. Similar conclusions can also be drawn based on the results obtained by studying the change in the mitochondrial membrane potential (Figure 3.2.8a). Primarily, with the exposure of 20 μM and 40 μM of H_2O_2, membrane depolarization was increased more compared to the untreated control, which could induce apoptosis and cellular death. (Figure 3.2.6e). However, at the exposure of 20 and 40 μM H_2O_2 and treatment with p(NAG-Ac-NAE) hydrogel, it exhibited an increase in the fluorescence activity in support of the protective/HIf1α induced preconditioning role of p(NAG-Ac-NAE) hydrogel towards the mitochondria. Intracellular ROS generation was higher in 20 μM and 40 μM H_2O_2 exposure. However, while it was treated with both p(NAG-Ac-NAE) and p(NAG-b-A) hydrogel in the presence of H_2O_2, a decrease in ROS production is observed (Figure 3.2.8b). ROS production is highly inhibited in p(NAG-co-Ac) hydrogel then the p(NAG-Ac-NAE) hydrogel. This could be due to the presence of glycine moiety because glycine uptake can activate the AKT/NF-Ƙβ65/Hif1α signalling pathway. In differentiated cells, the 40 μM H_2O_2 treatment restricts neurite extension, disturbs the terminals as well as dendrites and exhibits nuclear damage. While neuroprotective role of p(NAG-Ac-NAE) hydrogel prevents the H_2O_2 oxidative stress-induced damage and promotes neurite extension with healthy dendrites, axon, and axonal terminal and also protects the nuclear damage (Figure 3.2.6c). The mechanism behind the protection is the interaction between the NH and NH_2 group of p(NAG-Ac-NAE) with OḢ free radicals that have been identified from

the Raman study (Figure 3.2.8d), that down-regulates the ROS level of intracellular concentration up to the physiological ROS condition and assist the neurogenesis. It can also be noted that the physiological level of ROS supports the crucial cellular processes, acting as a second messenger that can regulate the intrinsic signalling pathways, contribute to the neurogenesis, polarization, maturation of neurons and help in discriminating between 'oxidative distress' and 'oxidative eustress'. [62]

In physiological conditions, glutamine is metabolized into glutamate by glutaminase-I and inhibition of glutaminase-I or glutamine deprives endothelial cells causing the vessel sprouting defect, [63] [64] [65] which shows the potential role of glutamate in angiogenesis. The phenomenon corroborated our CMA results as shown in Figure 3.2.9. The vessel sprouting is induced by p(NAG-Ac-NAE) hydrogel with an increase in vessel area, total vessel length, junction density and total number of junctions with increased expression of VEGF isoforms (Figure 3.2.11) even in stress conditions. However, the treatment with p(NAG-b-A) hydrogel at the lower concentration induces the expression of VEGF. From all these results, we can propose that the p(NAG-Ac-NAE) hydrogel can exhibit the VEGF stimulatory action via PI3K/Akt/mTOR signalling pathway as mTOR signalling regulates the gene expression of vascular endothelial growth factor (VEGF). [64] *However*, extensive research needs to be done in this direction to understand the biological mechanism of the pro-angiogenic activity, and *in vivo* based study which is out of the scope of this work. Angiogenesis is a major issue in brain cancer and glioma-derived neurotransmitter glutamate has a crucial role in tumor angiogenesis. [65] Interestingly, our p(NAG-Ac-NAE) hydrogel shows pro-angiogenic activity (Figure 3.2.10) and it shows non-tumorigenic activity against the aggressive cancer cell lines such as LN229 and MDA-MB-231 (Figure 3.2.4).

Overall p(NAG-Ac-NAE) hydrogel possess key advantages over the existing hydrogel for the neuroregeneration.

1. It is earlier reported that for the preconditioning activity and for ROS elimination, the hydrogels were encapsulated with the antioxidant drugs like curcumin, [66] gallic acid[67] and tannic acid[68] etc. However, interestingly p(NAG-Ac-NAE) hydrogel itself gives the preconditioning effects and ROS-eliminating activity via triggering the Hif1α expression and thus no need to load with any drugs.
2. Use of the neurotrophic factor plays a crucial role in enhancing neurogenesis. However, the delivery of neurotrophic factor is challenging due to the requirement of trophic factor at a specific concentration, as the excessive dose may create other consequences. Therefore, number of nanoparticles and hydrogels require to use for the delivery of neurotrophic factors is very important to achieve effective therapeutic efficiency. On the other hand our hydrogel is effective without any additional neurotrophic factors and gives the stimulatory effect for neurotrophic factor like VEGF.[69, 70].
3. Excitingly, to the best of our knowledge the novel hydrogel p(NAG-Ac-NAE) is the only one which possess the dual characteristics of angiogenesis and neurogenesis. [71]
4. For the development of conductive hydrogel there is a need of doping with conductive material, however synthesized hydrogel fall in the category of semi-

conductive material Thus, the p(NAG-Ac-NAE) hydrogel has the potential for angiogenesis, neurogenesis and could be helpful in the management of

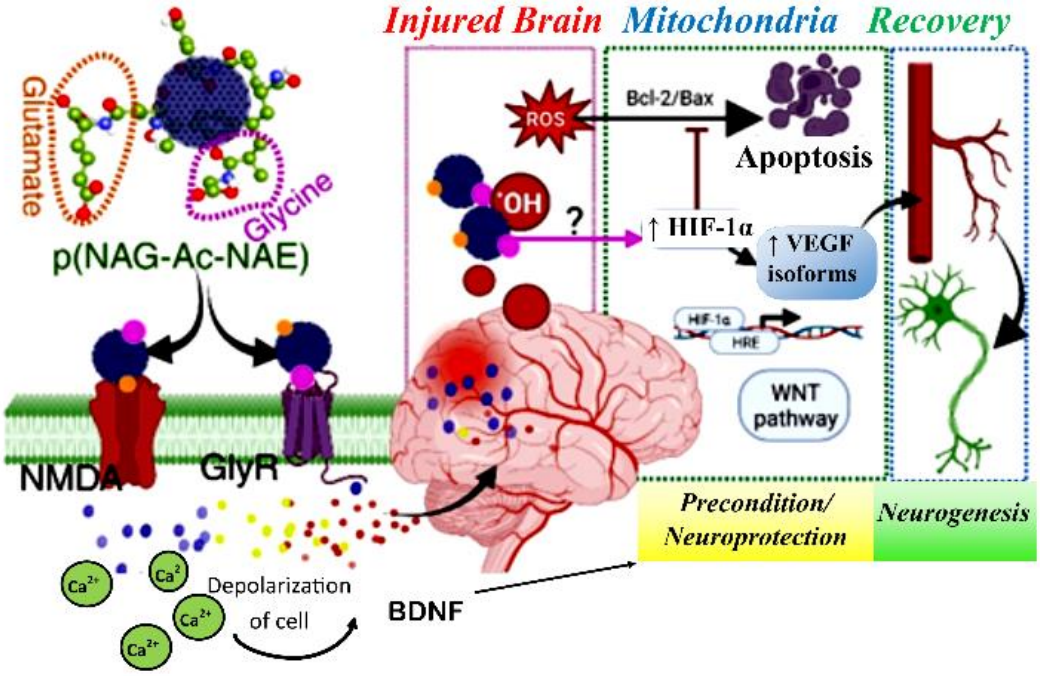

neurodegenerative diseases

Figure 10. Mechanism of p(NAG-Ac-NAE) induced neuroprotection and neurogenesis. Side chains of p(NAG-Ac-NAE) interact with the NMDA and glycine receptor which depolarized the cells and induce the BDNF secretion leads the neuroprotection. This hydrogel interacts with the free radicals and in the neuronal cell increases the expression of HIF-1α which delayed the apoptosis. This increased HIF-1α promotes the VEGF expression and increased the angiogenesis. Increased angiogenesis leads the neuronal stem cell migration and promotes the neurogenesis

3.2.6. ***CONCLUSIONS.***

In this work p(NAG-Ac-NAE) hydrogel has been synthesized. The free radical polymerization technique and the presence of acryloyl glutamate and acryloyl glycine yield the highest water retenting, pH-responsive, semi-conductive (7 $x10^{-5}$ S cm^{-1}) and biodegradable polymeric hydrogel. The viscoelastic behavior of this hydrogel such as elastic modulus of 2.3 kPa to 2.7 kPa provides a suitable macro-environment to the neuronal stem cell for outer growth. The presence of glycine derivatives moiety and glutamate derivative moiety provides the physical cue and vasculogenesis-assisted neurite outgrowth along with maintaining the microtubule integrity of the neuronal cells. The

p(NAG-Ac-NAE) hydrogel having the free functional groups of glycine and glutamate which involve in neuronal homeostasis and angiogenesis as it shown the HIF1α induced, VEGF expression stimulatory effect. Furthermore, this hydrogel possesses protective roles and preconditioning effect via scavenging the ROS generation and the mitochondrial membrane depolarization in oxidative stress conditions along with increased expression of HIF1α. Thus, this hydrogel has the potential in the treatment of neurodegenerative diseases and for the delivery of neuronal stem cells and growth factors for regenerative applications as it doesn't show the pro-inflammatory effect. Studying the complete molecular level mechanisms can be considered as the future scope of this work.

3.2.7. *REFERENCE*

1. Grimaudo, M.A., et al., *Bioactive injectable hydrogels for on demand molecule/cell delivery and for tissue regeneration in the central nervous system.* Acta Biomater, 2022. **140**: p. 88-101.
2. Chen, Y., J. Lin, and W. Yan, *A Prosperous Application of Hydrogels With Extracellular Vesicles Release for Traumatic Brain Injury.* Front Neurol, 2022. **13**: p. 908468.
3. Feigin, V.L., et al., *The global burden of neurological disorders: translating evidence into policy.* The Lancet Neurology, 2020. **19**(3): p. 255-265.
4. Collaborators, G.B.D.N., *Global, regional, and national burden of neurological disorders, 1990-2016: a systematic analysis for the Global Burden of Disease Study 2016.* Lancet Neurol, 2019. **18**(5): p. 459-480.
5. Kim, G., et al., *The role of oxidative stress in neurodegenerative diseases, Exp.* Neurobiology, 2015. **24**: p. 325.
6. Kim, G.H., et al., *The Role of Oxidative Stress in Neurodegenerative Diseases.* Exp Neurobiol, 2015. **24**(4): p. 325-40.
7. Nih, L.R., et al., *Dual-function injectable angiogenic biomaterial for the repair of brain tissue following stroke.* Nat Mater, 2018. **17**(7): p. 642-651.
8. Boni, R., et al., *Current and novel polymeric biomaterials for neural tissue engineering.* J Biomed Sci, 2018. **25**(1): p. 90.

9. Ma, X., et al., *Design and Fabrication of Polymeric Hydrogel Carrier for Nerve Repair.* Polymers (Basel), 2022. **14**(8).
10. Akhtar, A., et al., *Emerging polymeric biomaterials and manufacturing-based tissue engineering approaches for neuro regeneration-A critical review on recent effective approaches.* Smart Materials in Medicine, 2023. **4**: p. 337-355.
11. Li, G., et al., *Precise synthesis of poly(N-acryloyl amino acid) through photoinduced living polymerization.* Polymer Chemistry, 2018. **9**(20): p. 2733-2745.
12. Park, S.-B., et al., *Poly(glutamic acid): Production, composites, and medical applications of the next-generation biopolymer.* Progress in Polymer Science, 2021. **113**: p. 101341.
13. Wei, M., et al., *Preparation of pH-Responsive Poly(gamma-glutamic acid) Hydrogels by Enzymatic Cross-Linking.* ACS Biomater Sci Eng, 2022. **8**(2): p. 551-559.
14. Kim, M.H., et al., *Enzymatically Cross-Linked Poly(gamma-glutamic acid) Hydrogel with Enhanced Tissue Adhesive Property.* ACS Biomater Sci Eng, 2020. **6**(5): p. 3103-3113.
15. Zhang, W., et al., *A tough and self-healing poly(l-glutamic acid)-based composite hydrogel for tissue engineering.* Journal of Materials Chemistry B, 2018. **6**(42): p. 6865-6876.
16. Wasnik, K., et al., *Poly(N-acryloylglycine-acrylamide) Hydrogel Mimics the Cellular Microenvironment and Promotes Neurite Growth with Protection from Oxidative Stress.* ACS Applied Bio Materials, 2023.
17. Eric Samarut1, A.B.a.P.D., *Transcriptomic Analysis of Purified Embryonic Neural Stem Cells from Zebrafish Embryos Reveals Signaling Pathways Involved in Glycine-Dependent Neurogenesis.* Frontiers in Molecular Neuroscience, 2016. **9** (22).
18. Edna Brustein, S.b.C., Julien Ghislain, Pierre Drapeau, *Spontaneous Glycine-Induced Calcium Transients in Spinal Cord Progenitors Promote Neurogenesis.* Calcium Transients in Neurogenesis, 2012.
19. Wang, L., et al., *A biomimetic piezoelectric scaffold with sustained Mg2+ release promotes neurogenic and angiogenic differentiation for enhanced bone regeneration.* Bioactive Materials, 2023. **25**: p. 399-414.

20. Yu, S., et al., *Angiogenic microspheres promote neural regeneration and motor function recovery after spinal cord injury in rats.* Scientific Reports, 2016. **6**(1): p. 33428.
21. González-Pérez, F., et al., *Protease-Sensitive, VEGF-Mimetic Peptide, and IKVAV Laminin-Derived Peptide Sequences within Elastin-Like Recombinamer Scaffolds Provide Spatiotemporally Synchronized Guidance of Angiogenesis and Neurogenesis.* Adv Healthc Mater, 2022. **11**(22): p. e2201646.
22. Park, S.Y., et al., *Syntheses of biodegradable polymer networks based on polycaprolactone and glutamic acid.* Polymers for Advanced Technologies, 2019. **30**(4): p. 872-878.
23. *MALDI MASS SPECTROMETRY FOR SYNTHETIC POLYMER ANALYSIS*. CHEMICAL ANALYSIS

A SERIES OF MONOGRAPHS ON ANALYTICAL CHEMISTRY AND ITS APPLICATIONS, ed. J.D. WINEFORDNER. Vol. 175. A JOHN WILEY & SONS, INC., PUBLICATION.

24. Van Dyke, J.D. and K.L. Kasperski, *Thermogravimetric study of polyacrylamide with evolved gas analysis.* Journal of Polymer Science Part A: Polymer Chemistry, 1993. **31**(7): p. 1807-1823.
25. Dassanayake, N.L. and R.W. Phillips, *Determination of the composition of acrylamide/acrylate copolymers using thermogravimetric analysis.* Analytical Chemistry, 1984. **56**(9): p. 1753-1755.
26. Peres, L.B., et al., *pH-responsive physically and chemically cross-linked glutamic-acid-based hydrogels and nanogels.* European Polymer Journal, 2018. **101**: p. 341-349.
27. Kim, A., et al., *Intracellular Delivery of Charge-Converted Monoclonal Antibodies by Combinatorial Design of Block/Homo Polyion Complex Micelles.* Biomacromolecules, 2016. **17**(2): p. 446-453.
28. Melodia, D., et al., *Traceless pH-Sensitive Antibody Conjugation Inspired by Citraconic Anhydride.* Biomacromolecules, 2022. **23**(12): p. 5322-5329.
29. Uman, S., A. Dhand, and J.A. Burdick, *Recent advances in shear-thinning and self-healing hydrogels for biomedical applications.* Journal of Applied Polymer Science, 2020. **137**(25): p. 48668.

30. Musgrove, R.E., et al., *Oxidative stress in vagal neurons promotes parkinsonian pathology and intercellular α-synuclein transfer.* The Journal of Clinical Investigation, 2019. **129**(9): p. 3738-3753.
31. Forman, H.J., A. Bernardo, and K.J.A. Davies, *What is the concentration of hydrogen peroxide in blood and plasma?* Archives of Biochemistry and Biophysics, 2016. **603**: p. 48-53.
32. Whittemore, E.R., et al., *A detailed analysis of hydrogen peroxide-induced cell death in primary neuronal culture.* Neuroscience, 1995. **67**(4): p. 921-932.
33. Zenin, V., et al., *Resistance to H(2)O(2)-induced oxidative stress in human cells of different phenotypes.* Redox Biol, 2022. **50**: p. 102245.
34. Kämmerer, P.W., et al., *Continuous electrical stimulation affects initial growth and proliferation of adipose-derived stem cells.* Biomedicines, 2020. **8**(11): p. 482.
35. Gerencser, A.A., et al., *Quantitative measurement of mitochondrial membrane potential in cultured cells: calcium-induced de- and hyperpolarization of neuronal mitochondria.* J Physiol, 2012. **590**(12): p. 2845-71.
36. Nouri, F., S.N. Nematollahi-Mahani, and A.M. Sharifi, *Preconditioning of Mesenchymal Stem Cells with Non-Toxic Concentration of Hydrogen Peroxide Against Oxidative Stress Induced Cell Death: The Role of Hypoxia-Inducible Factor-1.* Adv Pharm Bull, 2019. **9**(1): p. 76-83.
37. Tang, X.-Q., et al., *Protection of oxidative preconditioning against apoptosis induced by H2O2 in PC12 cells: mechanisms via MMP, ROS, and Bcl-2.* Brain research, 2005. **1057**(1-2): p. 57-64.
38. Font, M.A., A. Arboix, and J. Krupinski, *Angiogenesis, neurogenesis and neuroplasticity in ischemic stroke.* Curr Cardiol Rev, 2010. **6**(3): p. 238-44.
39. Wang, H., et al., *Modulating effects of preconditioning exercise in the expression of ET-1 and BNP via HIF-1α in ischemically injured brain.* Metabolic Brain Disease, 2019. **34**(5): p. 1299-1311.
40. Chang, S., et al., *Exogenous low dose hydrogen peroxide increases hypoxia-inducible factor-1alpha protein expression and induces preconditioning protection against ischemia in primary cortical neurons.* Neuroscience Letters, 2008. **441**(1): p. 134-138.
41. Xiao-qing, T., et al., *Hydrogen peroxide preconditioning protects PC12 cells against apoptosis induced by dopamine.* Life Sciences, 2005. **78**(1): p. 61-66.

42. Gałecki, P., et al., *Vascular endothelial growth factor receptor 2 gene (KDR) polymorphisms and expression levels in depressive disorder.* Journal of Affective Disorders, 2013. **147**(1): p. 144-149.
43. Leung, L. and C.M. Cahill, *TNF-α and neuropathic pain - a review.* Journal of Neuroinflammation, 2010. **7**(1): p. 27.
44. Patel, A.J. and A. Hunt, *Concentration of free amino acids in primary cultures of neurones and astrocytes.* Journal of neurochemistry, 1985. **44**(6): p. 1816-1821.
45. Hansen, J.Y., et al., *Mapping neurotransmitter systems to the structural and functional organization of the human neocortex.* Nature Neuroscience, 2022. **25**(11): p. 1569-1581.
46. Liu, R., et al., *Glycine Exhibits Neuroprotective Effects in Ischemic Stroke in Rats through the Inhibition of M1 Microglial Polarization via the NF-kappaB p65/Hif-1alpha Signaling Pathway.* J Immunol, 2019. **202**(6): p. 1704-1714.
47. Abdelhamid Bekri1, Meijiang Liao1 and Pierre Drapeau, *Glycine Regulates Neural Stem Cell Proliferation During Development via Lnx1-Dependent Notch Signaling.* Frontiers in Molecular Neuroscience, 2019. **12**(44): p. 1-7.
48. Brodsky, V.Y., et al., *Glutamic Acid Signal Synchronizes Protein Synthesis Kinetics in Hepatocytes from Old Rats for the Following Several Days. Cell Metabolism Memory.* Biochemistry (Moscow), 2018. **83**(3): p. 294-298.
49. Chen, T.S., et al., *The Role of Glutamate Receptors in Epilepsy.* Biomedicines, 2023. **11**(3).
50. Hubel, N., et al., *The role of glutamate in neuronal ion homeostasis: A case study of spreading depolarization.* PLoS Comput Biol, 2017. **13**(10): p. e1005804.
51. Chen, T.J. and M. Kukley, *Glutamate receptors and glutamatergic signalling in the peripheral nerves.* Neural Regen Res, 2020. **15**(3): p. 438-447.
52. Gerhard, D.M., E.S. Wohleb, and R.S. Duman, *Emerging treatment mechanisms for depression: focus on glutamate and synaptic plasticity.* Drug Discov Today, 2016. **21**(3): p. 454-64.
53. Numakawa, T., H. Odaka, and N. Adachi, *Actions of Brain-Derived Neurotrophin Factor in the Neurogenesis and Neuronal Function, and Its Involvement in the Pathophysiology of Brain Diseases.* Int J Mol Sci, 2018. **19**(11).
54. Yamala, A.K., et al., *Poly-N-acryloyl-(L-phenylalanine methyl ester) hollow core nanocapsules facilitate sustained delivery of immunomodulatory drugs and exhibit adjuvant properties.* Nanoscale, 2017. **9**(37): p. 14006-14014.

55. Chaumeil, M.M., et al., *pH as a biomarker of neurodegeneration in Huntington's disease: a translational rodent-human MRS study*. J Cereb Blood Flow Metab, 2012. **32**(5): p. 771-9.
56. Saberi, A., et al., *Electrically Conductive Materials: Opportunities and Challenges in Tissue Engineering.* Biomolecules, 2019. **9**(9).
57. Bettinger, C.J., et al., *Biocompatibility of biodegradable semiconducting melanin films for nerve tissue engineering.* Biomaterials, 2009. **30**(17): p. 3050-7.
58. Leipzig, N.D. and M.S. Shoichet, *The effect of substrate stiffness on adult neural stem cell behavior*. Biomaterials, 2009. **30**(36): p. 6867-78.
59. Ali, S., et al., *The effect of Young's modulus on the neuronal differentiation of mouse embryonic stem cells.* Acta Biomater, 2015. **25**: p. 253-267.
60. Dou, X., et al., *Effect of Chirality on Cell Spreading and Differentiation: From Chiral Molecules to Chiral Self-Assembly.* ACS Appl Mater Interfaces, 2019. **11**(42): p. 38568-38577.
61. Tang, X.-Q., et al., *Protection of oxidative preconditioning against apoptosis induced by H2O2 in PC12 cells: Mechanisms via MMP, ROS, and Bcl-2*. Brain Research, 2005. **1057**(1): p. 57-64.
62. Wilson, C., E. Muñoz-Palma, and C. González-Billault, *From birth to death: A role for reactive oxygen species in neuronal development.* Seminars in Cell & Developmental Biology, 2018. **80**: p. 43-49.
63. Huang, H., et al., *Role of glutamine and interlinked asparagine metabolism in vessel formation.* EMBO J, 2017. **36**(16): p. 2334-2352.
64. Tsuji-Tamura, K., et al., *The role of PI3K/Akt/mTOR signaling in dose-dependent biphasic effects of glycine on vascular development.* Biochemical and biophysical research communications, 2020. **529**(3): p. 596-602.
65. Zheng, F., et al., *Targeting xCT-mediated glutamate release normalizes tumor angiogenesis in the brain.* bioRxiv, 2017: p. 134924.
66. Li, Q., et al., *Recent trends in the development of hydrogel therapeutics for the treatment of central nervous system disorders.* NPG Asia Materials, 2022. **14**(1): p. 14.
67. Zhang, D., et al., *In situ forming and biocompatible hyaluronic acid hydrogel with reactive oxygen species-scavenging activity to improve traumatic brain injury repair by suppressing oxidative stress and neuroinflammation.* Materials Today Bio, 2022. **15**: p. 100278.

68. Xu, J., et al., *Bioactive self-healing hydrogel based on tannic acid modified gold nano-crosslinker as an injectable brain implant for treating Parkinson's disease.* Biomaterials Research, 2023. **27**(1): p. 8.
69. Madhusudanan, P., G. Raju, and S. Shankarappa, *Hydrogel systems and their role in neural tissue engineering.* J R Soc Interface, 2020. **17**(162): p. 20190505.
70. El Ouaamari, Y., et al., *Neurotrophic Factors as Regenerative Therapy for Neurodegenerative Diseases: Current Status, Challenges and Future Perspectives.* Int J Mol Sci, 2023. **24**(4).
71. Lu, J., et al., *Enhanced angiogenesis by the hyaluronic acid hydrogels immobilized with a VEGF mimetic peptide in a traumatic brain injury model in rats.* Regenerative Biomaterials, 2019. **6**(6): p. 325-334.

CHAPTER 3: Results and Discussion (Part-III)

Objective III. Comparative assessment of glycine, n-acryloyl glycine and glycine based Anti-cancer poly (N-acryloyl glycine-b-acrylamide) hydrogel for its geometric properties and induce cell killing in poor prognosis heparanase driven malignancies through *in silico* and *in vitro* approach.

3.3.1. **ABSTRACT.**

In the present work, The geometrical/electronic properties of Glycine, N-acryloylglycine monomer (NAG), and polymeric units of poly [(N-acryloylglycine)-co-(acrylamide)] p(NAG-b-A) are rationalized by density functional theory (DFT) and experimental evidences have been provided for their uses in poor prognostic cancer therapy. Glycine plays a pivotal role in cell survival, and Most of the anti-cancer agents alter the glycine metabolomics and suppress the cell proliferation. Herein, The Frontier Molecular Orbital theory (FMO) reveals that the introduction of acrylamide/ divinyl benzene in the glycine based polymer has increased the biological activities by lowering the band gap energy. Furthermore, Heparanase and proteases is an important are implicated in an invasive tumor progression and worsening the prognosis. Linear and cross-linked co-polymeric rearrangements p(NAG-b-A) polymer show the protease inhibitory activities. Cross-linked homo-polymeric and cross-linked-hetro-polymeric tetrameric arrangements inhibits the heparanase activity via interacting at heparanase binding domain II (HBDII) with dock score of ~-11.08 kcal mol^{-1} (Ki=nm) and at heparanase binding

domain III (HBD III)., p(NAG-b-Ac) hydrogel shown the heparanase inhibitory activity comparable with heparin. The synthesized p(NAG-b-A) hydrogel is heamatocompatible, anti-proliferative and migratory inhibitor against the cancer cells and favors the to the programmed cell death. Additionally, the p(NAG-b-A) hydrogel exhibited anti-angiogenic behavior in the *in-ovo* system. In conclusion, p(NAG-b-A) with anti-angiogenic and anti-tumorigenic capabilities has made it as a future potential anticancer polymer for heparanase-driven invasive malignancies and synergistic delivery system which further could improve the prognosis.

3.3.2. INTRODUCTION

Aggressive phenotype, vast heterogeneity, unique pathophysiology of solid tumors, the emergence of resistance, negative expression of receptors, and invasive and metastasis cancer are the second leading major causes forof death. due to cancer [1] [2]. As per the global fact sheet, cancer is the second leading cause followed by cardiovascular diseases and about 1 in every 6 deaths worldwide [3]. Chemo-resistance and radiation resistance contribute to the treatment failure for the cancer treatment [4]. Irradiation subsequently alters the invasion and migration of cancer stem cells, and thus local recurrence and metastases remain a therapeutic challenge [5]. Therefore, protease inhibitor based anticancer therapy is considered an exciting option in cancer therapy. Another hallmark of the aggressive cancer is the overexpression of heparanase, which is an endo-β-D-glucuronidase enzyme that cleaves the constituent of fundamental extracellular matrix (ECM), i.e., heparan sulfate proteoglycan and releases heparan sulfate and affects the ECM integrity. Thus, over activity of heparanase facilitates metastasis, neo-angiogenesis and cancer stem cell migration. Further, heparanase has the pleiotropic effects in tumor cells and is widely overexpressed in glioblastoma [6], TNBC [7], hepatocellular carcinoma, oral cancer [8] and melanoma [9], which are the aggressive types of

cancer with poor prognosis and demonstrate the worsed outcome with low survival rate. Heparanase mediated cell invasion is enhanced in hypoxic condition along with induced angiogenesis and metastasis. It also regulates the CD24 (surface biomarker of tumor stem cell) expression as overexpressed heparanase consistently up-regulated the CD24 and significantly shortened survival life found heparanase induced high grade and low grade glioma [10]. Hence, designing the effective heparanase inhibitor and treatment using heparanase inhibitor could be considered the future potential for cancer therapy. Till date none of the heparanase inhibitor has been clinically approved and hence there is a lot of scope is there to improve the therapeutic efficiency.

On the other hand for the cancer therapy, biopolymers of their variable structures aided the advantages like improved bioavailability, stability and target specificity, and co-delivery of multiple therapeutic agents [11]. The limitations of the conventional chemo-therapy drugs are limited aqueous solubility, severe toxicity, multidrug resistance, restricted bioavailability, inappropriate bio-distribution and pharmacokinetic [12]. Among the various synthetic polymeric systems, amino acid based polymeric systems are considered as future green materials for therapeutic applications. Poly(amino acid) polymers, β-sheet crystal structure formation spreads the stabilized structure and side chain cationic pendent structure facilitates the development of reactive oxygen species (ROS) that triggered the release behavior in response to H_2O_2 and shows the significant *in vitro / in vivo* tumor inhibition and the antimicrobial activity[13] . Conventional 'drug free macromolecule' for 'anticancer activity' is one of the interesting concept in cancer therapy. For this purposes, polymer-peptide conjugates, polymer-oligonucleotide and glycopolymers are used as drug free macromolecules.[12] The amino acid based polymer used various therapeutic purposes,

however, a few of them are reported as drug free macromolecules having anticancer properties. Such as, the dual acid-responsive polymeric micelle-forming cinnamaldehyde prodrugs exert the synergistic anticancer effect in colon tumor bearing model [14]. Sulphur and methacrylate based co-polymer synthesized by RAFT controlled radical polymerization is also reported as an anticancer cell membrane [15]. However, till date none of the polymers is reported which exerts the heparanase inhibitory property and anticancer activity.

On the above line, in the present work polymers of acrylate glycine have been designed and the anticancer and anti-angiogenic potential have been evaluated in the *in vitro* and *in-ovo* system. Firstly, we have evaluated the different biological activities of the acrylate glycine and varyied the polymeric units of acrylate glycine, in interaction with acrylamide through molinspiration software. Further, density functional theory (DFT) calculation was performed and the electronic as well as solvation parameters for the monomeric unit of glycine and different polymeric units of acrylate glycine interacted with the acrylamide and the cross linker (divinylbenzene) were investigated by applying B3LYP/6-311g* combination to assess the biological activities of this polymer. In order to provide the extent of reactivity and anticancer potential of the polymeric system, the energy band gap (HOMO/LUMO), chemical hardness and electrophilicity were calculated. Further, molecular-docking was performed to investigate the heparanase inhibitory activity of acrylate co-polymer. Finally, based on the computational results a series of experiments have been performed and correlated the efficiency of treatment of cancer using the synthesized polymers against the invasive aggressive cancer such as triple negative breast cancer (TNBC), glioblastoma and lung cancer. However, before doing this cell based study this polymer has been characterized and cytotoxicity has been tested against a number of normal health and cancer cell lines. The migratory inhibitory activity was assessed

through the wound scratch assay. Finally, the cell death mechanism was investigated through flow cytometry assay and the anticancer activity of the polymer without using conventional drugs has been established. Overall study assesses the potent of this anticancer polymer as a future synergistic drug free macromolecule in cancer therapy.

3.3.3. METHODOLOGY

3.3.3.1.**Theoretical computational methodology.** For the evaluation of physicochemical properties and bioactivity, random arrangements were designed using ChemDraw Ultra 8.0 software and categorized into: (1) Linear homopolymer (polymer of N-acryloylglycine (G) arranged in G, G2……G_n), (2) Linear hetropolymer (polymer of G and acrylamide (A), GA (GA1), G-A-G……..(GA_n)), (3) cross-linked homopolymer (polymer of G cross-linked by using divinylbenzene (DVB), D1, D2……D6) and (4) arranged cross-linked hetropolymer (polymer of G and A is cross-linked by DVB, and series structure labeled as D1, D2…..Dn) and finally synthesized cross linked polymer termed as p(NAG-b-A) hydrogel. Firstly, bioactivities of all these structures were evaluated using molinspration software (https://www.molinspiration.com/). The predicted structures were determined using Avogadro software (version1.2.0) [17] and then optimized using the Merck molecular force field (MMFF 94) at molecular mechanic level. Further, Density functional theory (DFT) calculations were carried out using ORCA 5.3.2 computational package [18]. The computing efficiency was accelerated by using the resolution of identity approximation with basis sets B3LYP/6-311g*/def2-SVP level. Further, CPCM continuum solvation model was applied at water, ethanol, hexane and chloroform level ($\varepsilon = 80.4$).

3.3.3.2.**Molecular docking simulation.** The crystal structure of the human heparanase complex with CB678 inhibitor was retrieved from the RCSB protein data bank with PDBID-

7PRT (https://www.rcsb.org/structure/1Q5K) having the resolution of 1.70Å with the 100 steepest descent steps. The macromolecular preparation and energy minimization were conducted on UCSF Chimera by applying AMBER ff14SB and polar hydrogen atoms and Kollman charges were added. Reference ligand molecules such as *Cyclophellitol, Roneparstat and* 2-acetamido-2-deoxy-beta-D-glucopyranose were retrieved from the PubChem and energy minimization was conducted using PyrX interface by applying MMff94 force field in Autodock 4.2 tool [19]. Simulation was performed by generating the grid box, setting the genetic algorithms of 30 run and Lamarckian parameter. Furthermore, the analysis of the data was performed by using AutoDock and Discovery studio [20].

3.3.3.3.**Biodegradation assessment of p(NAG –co-Ac) hydrogel.** p(NAG-b-A) hydrogel was synthesized through the free radical miniemulsion polymerization technique and conformed through FTIR and NMR, as per previously reported literature. After the synthesis, structural and surface morphology was studied using field-emission scanning electron microscopy (FESEM) (Model; Nova Nano SEM 450) with an accelerating voltage of 10 kV. Further, dynamic swelling behaviour and enzymatic degradation were obtained at pH 7.4 using phosphate saline buffer (PBS), 100 µg mL^{-1} lysozyme in PBS solution, 100 µg mL^{-1} proteinase K in PBS, and 100 µg mL^{-1} collagenase by immersing the nearly 10 mg of p(NAG-b-A) hydrogel in 1 mL of respective solutions. The swelling indexes were calculated using eqn.(1)

$$MSI = \frac{(Ws-Wi)}{Wi} \times 100 \quad \text{.....(1)}$$

3.3.3.4.I**n vitro cytotoxicity assessment in normal and in cancer cell lines.** MTT colorimetric assay was used to investigate the cell viability of the novel material. MDA-MB-231, MCF7, LN229, L929, HEK 293, HepG2 and A549 cell lines were obtained from NCCS-Pune repository, India. All the cell lines were maintained in 10 % of Fetal bovine serum (FBS)

supplemented with Dulbecco's modified Eagle medium with 100 U of penicillin-streptomycin antibiotic in a humidified CO_2 incubator at 37 ℃. 1 X 10^4 cells were cultured for 24 hs in 96 well plate supplemented with complete medium followed by the treatment of glycine, N-acryloyl glycine monomer and p(NAG-b-A) with different concentration (from 2.5 mg mL^{-1} to 10 mL^{-1}) for another 24 hrs. After the incubation hydrogel was removed and incubated with 5 μg mL^{-1} of MTT reagent in fresh media and incubated for 4 hrs. Absorbance of dissolved formazan crystals/DMSO was measured at λ_{max} = 570 nm using microplate reader (Bioteck).

3.3.3.5.**Haemocompatibility of hydrogel.** Fresh RBCs were isolated from whole blood samples obtained from Wister rat and homogenous suspension was obtained in 5% dextrose solution (pH 7.4). For the evaluation of hemolytic impact of p(NAG-b-A) hydrogel and N-acryloyl glycine monomer, RBCs were exposed with different concentrations (1000, 500, 250, 125 and 62.5 μg mL^{-1}) of p(NAG-b-A) hydrogel for 8 and 24 hrs at 37 °C (with 100 RPM). Treatment with 5% dextrose solution was considered negative control, while treatment with 0.1-1% Triton-X was considered positive control. Percent haemolysis was calculated through spectrophotometrically by taking the absorbance maxima at λ = 540 nm for each sample.

3.3.3.6.**Wound scratch assay.** Cell migration ability was analyzed by performing wound scratch tests on LN229, MDA-MB-231 and L929 cell lines. The cells were seeded in 12 well plates and cultured till to get 80-90% confluent monolayer. Then scratches were made by using 200μL micropipette tips and then cells were washed two times using PBS. Further, three different concentrations of hydrogel, monomer and glycine were added separately and untreated as the control and cultured in complete media for 48 hrs. Then the images were acquired using inverted microscope at 24^{th} h and 48^{th} h. Then ImageJ analytical tool was used to estimate the percentage wound closer area at different time intervals.

3.3.3.7.**Live and dead assay.** MDA-MB-231 cells were incubated with glycine, NAG, and p(NAG-b-A) for 3 days to examine the comparative cellular death after the treatment. After 24 hrs and 72 hrs the cells were stained with acridine orange and ethidium bromide (100μg mL^{-1}) for 30 min. Afterward, the fluorescent macroscopic images were acquired at 20 X magnification.

3.3.3.8.**Apoptosis and necrotic assay.** After 24 hrs of treatment with glycine, NAG, and p(NAG-b-A) hydrogel, the percentage viable apoptotic and necrotic cell death of LN229 cells ($1X10^5$ cells) were quantified by flow cytometry. After 24 hrs of treatment, cells were detached by using 1mM EDTA solution and collected after washing with PBS followed by staining with Annexin V/PI as per the manufacture's protocol (BD Biosciences FITC Annexin-V apoptosis detection kit).

3.3.3.9.**ROS assay.** Flow cytometry analysis was conducted to evaluate the intracellular ROS level. After the treatment for 24 hours with glycine, NAG, and p(NAG-b-A) hydrogel, H_2O_2 treatment as positive control and untreated reference control, the adhered cells were collected (1200 RPM/5min) and washed with PBS for 3 times. Then the cells were stained with 50 μM solution of 2',7'–dichlorofluorescin diacetate DCFDA and incubated at 37 ℃ for 30 min. The intracellular ROS production and peak shift were analyzed by using flow cytometer (Beckman coulter).

3.3.3.10. **Chicken embryo angiogenesis (CEA) assay.** Vascular sprouting inhibitory potential of N-acryloyl glycine monomer and p(NAG-b-A) polymer were evaluated in *in ovo* system. Certified purchased (Ramana Hatchery, Varanasi, Uttar Pradesh, India) fertilized eggs were incubated in a humid environment at 37℃ for 4 days. Further, a little circular examination window was generated and 1-2 mL of albumen was removed for the detachment of developing

chick embryo chorioallantoic membrane. Further three different concentrations (2.5 μg mL^{-1}, 25 μg mL^{-1}, 100 μg mL^{-1}) of monomer and p(NAG-b-A) hydrogel were applied through pipetting. Change in vasculature was examined for 0, 2, 4, and 8 hrs by accruing the images using stereo zoom microscope-mounted Magnus camera (Magcam DC plus 10, Magnus Opto Systems India Pvt. Ltd., New Delhi, India). Images were analysed through the Image J angio tool software.

3.3.3.11. **Fondaparinux heparanase inhibitory assay.** To determine the heparanase inhibitory activity of glycine, n-acryloylglycine and p(NAG-b-Ac) hydrogel colorimetric fondaparinux heparanase inhibitory assay was performed using heparin as positive control for heparanase inhibition. The 100 μl of reaction were setup on 4%BSA in TBST pre-treated plate which contain 200 ng mL^{-1} of heparanase, 100 μM of Fondaparinux sodium in 40mM sodium acetate (pH 5) with/without inhibitor were incubated for 18 h. at 37◦C. Afterwards, the reaction was quenched with 100 μl of 0.1M NaOH with 30μM of resazurin by incubation at 45˚C for one hour. The change in fluorescence were recorded at 560 nm of excitation and 590nm emission wavelength.

3.3.3.12. **Statistical Analysis.** Herein, all the data are presented as mean ± 1 standard deviation (SD). One-way ANOVA with Tukey's test was used to evaluate the statistical significance of the comparison groups by considering $p<0.05$ is a significant difference. All analysis was performed using Origin software.

3.3.4. RESULTS AND DISCUSSION

3.3.4.1.**Theoretical bioactivity assessment of p(NAG-b-A).** Synthesized polymers have wide applications in various medical fields. Any molecule that interacts with the native protein gives therapeutic effects. Therefore, to predict the biological activity of p(NAG-b-A), before synthesizing the polymer, bioactivity score calculation was conducted using Molinspiration software and the obtained values have been listed in Table S3.3. 1. Activity scores more than 0.00 have been considered as the bioactive molecules. Scores 0.50 to 0.00 have been considered as moderately active and more than -0.50 have been presumed as inactive molecules. Designed 58 were categorized into four groups: (1) Linear homopolymer (LH)(G1 to G11), (2) Linear Hetropolymer (LE)(GA series), (3) Cross-linked homopolymer(CH) (D1 to D6) and (4) Cross-linked hetropolymer (CE)(D7 to D25). All these polymeric structures show negative scores for kinase inhibitors, ion channel modulators and nuclear receptor ligands, and 55% of polymeric structures show positive scores for GPCR ligands (lower) and protease inhibitors (higher) (Table S3.3. 2). Among the several random structures, most of the compounds act as potent protease inhibitors with highest score for LE, CH and CE with highest for GA2, GA3, GA4 and D22 of 0.5

3.3.4.2.**DFT Calculation of randomized structure of p(NAG-b-A) polymeric unit.** DFT offers a high level of accuracy with reduced time-consuming empirical process. It is a computationally inexpensive approach than the ab initio approach, which provides information about the geometric and electronic characteristics and subsequently gives the idea of the selected polymer as a drug delivery system [21]. Through the auto dock all structures were analyszed for acceptable torson angle, and among 58 random arrangements of NAG, acrylamide and DVB, geometry optimization and water solvation parameters were calculated

for 38 random arrangements. Dipole moment and intermolecular/intermolecular hydrogen bonding in the presence of different solvents provide a correlation between stability, polarity, reactivity and swelling behavior of the polymers [22]. The DFT calculation was performed by relaxing the selected polymeric molecular structures in vacuum and polar/nonpolar solvents,

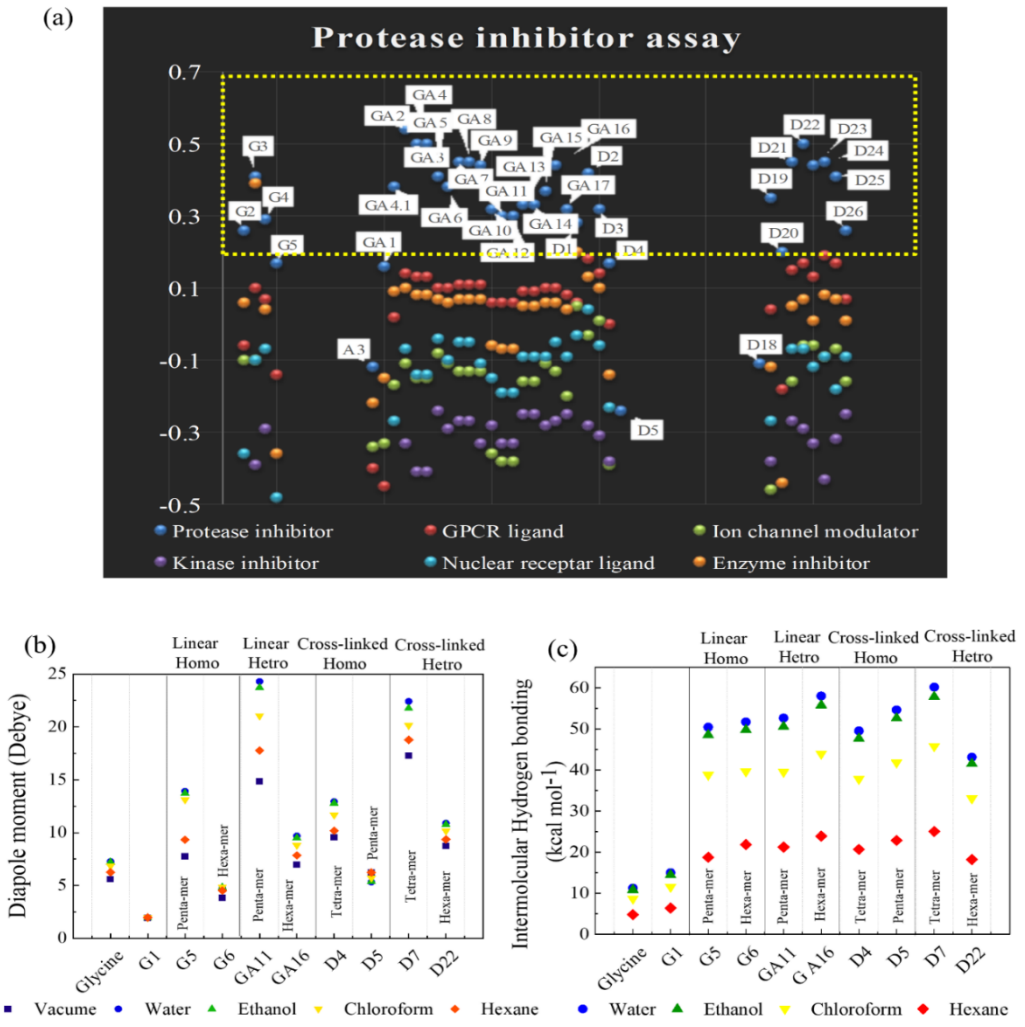

Figure 3.3. 1 Theoretical bioactivity scores of random arrangements of N-acryloyl glycine, acrylamide and cross linked structures categorized into: (1) linear homopolymer (G1 to G11), (2) linear hetropolymer (GA series), (3) cross-linked homopolymer (D1 to D6), and (4) cross-linked hetropolymer (D7 to D25). Series 1: protease inhibitor, Series 2: GPCR ligand, Series: Ion channel modulator, Series 4: Kinase inhibitor, Series 5: Nuclear receptor ligand, and Series 6- enzyme inhibitor.

The calculated intermolecular hydrogen bonding, dipole moment and free energy (in HF) are listed in Table 2. Highest dipole moment values in glycine (5.58, 7.27 , 7.2 , 6.85 and 6.24

Debye in vacuum, water ethanol, $CHCl_3$ and hexane, respectively) are obtained. The conversion of glycine to N-acryloylglycin shows a significantly decreased dipole moment to 1.93 Debye (Figure 3.3.1b). With an increase in N-acryloyl glycine units up to pentamers (i.e. homopolymer(G5)), an increase in the dipole moment is observed, where a sudden decrease in the dipole moment in hexamer unit(G6)is observed. The similar phenomenon have been observed in all LH, LE and in CH. The introduction of acrylamide to form hetropolymers showed significant increase in the dipole moment up to the pentamer unit (GA11), while the incorporation of cross-linkers slightly decreased the dipole moment. The highest dipole observed for cross linked For the hetro-hexamer (D7) (Figure 1b).. From the results, this variation in dipole moment is well suited with the polar (acrylamide) or nonpolar nature of the acrylamide/DVB in the polymeric unit. In all the cases the highest dipole moment observed in order of water> ethanol> CHCl3> hexane> vacuum.

The decrease in the number of hydrogen bonds refers to increase in swelling ratio of the polymers due to the reduction in intermolecular interactions. Conductor-like polarizable continuum model (CPCM) was used to calculate the intermolecular energy for hydrogen binding for all structures in both polar (water and ethanol) and nonpolar (chloroform and hexane) solvents. The intermolecular energy was found to be in the order of CE>CH=LE>LH i n water, as the polarity has been decreased from water to hexane, the intermolecular hydrogen bonding also decreased (see Table S3.3. 3 and Figure 3.3.2). The highest intermolecular hydrogen bonding energy was observed for D7 and GA16 with 60.18 kcal mol^{-1} and 58.02 kcal mol^{-1} in water, and 57.85 kcal mol^{-1} and 55.77 kcal mol^{-1} in ethanol, respectively.

Furthermore, the Koopmans theorem was useful in the identification of molecular reactivity in terms of ionization potential (I), chemical hardness (η), softness (σ), electronegativity (μ) and

electrophilicity [23]. Molecular kinetic stability is indicated in terms of HOMO and LUMO energy gap (ΔE) as higher value attributes to the chemical stability, while the lower value shows more polarizability with higher biological activities [21, 23]. Glycine molecules contribute to the chemical stability, while acrylate glycine exhibits the chemical reactivity. The energy band gap for acryloyl glycine, acrylamide, GA1 and D1 are calculated to be 6.006 eV, 5.99 eV, 6.95 eV and 5.018 eV, respectively (Table S3.3. 3 and Figure 3.3.2). Almost in all cross-linked structures the energy band gap is comparatively lower in value than the LH and LE polymer. The well suited HOMO - LUMO energy band gap values of monomer and cross-linked polymer with molecular docking results are represented in Figure 3.3.2. Higher electrophilicity shows the higher antimicrobial and anticancer properties It was reported that ω >1.5eV shows good biological activity[23]. In our case, for all the structures, ω was in a range of 1.6 eV–2.6 eV and for GA17 sudden increase in ω is calculated to be 9.4 eV.

3.3.4.3 Comparative heparanase inhibitory activity of p(NAG-b-A) polymeric units: molecular docking based investigation. Energy band gap and electrophilicity of cross-linked p(NAG-b-A) polymeric units provide the idea about therapeutic activity. Further, molecular interaction studies between 38 random arrangements and human heparanase (PDBID 7PRT) were performed using the geometrically optimized structures obtained after DFT calculation in vacuum. The remaining structures were excluded for DFT calculation and for molecular docking due to higher number of monomers (more than 6 units) showing the higher torsion angle such as θ = 32° (as Autodock tool works best for ligands with 32° torsion angles). Increased expression level of heparanase is a biomarker level of multiple aggressive cancers and poor prognosis. However, none of the heparanase inhibitors are approved in clinical trials. For the evaluation of potential application of p(NAG-b-A) in cancer treatment, we have

performed molecular docking study and the results were compared with the available reference inhibitor.

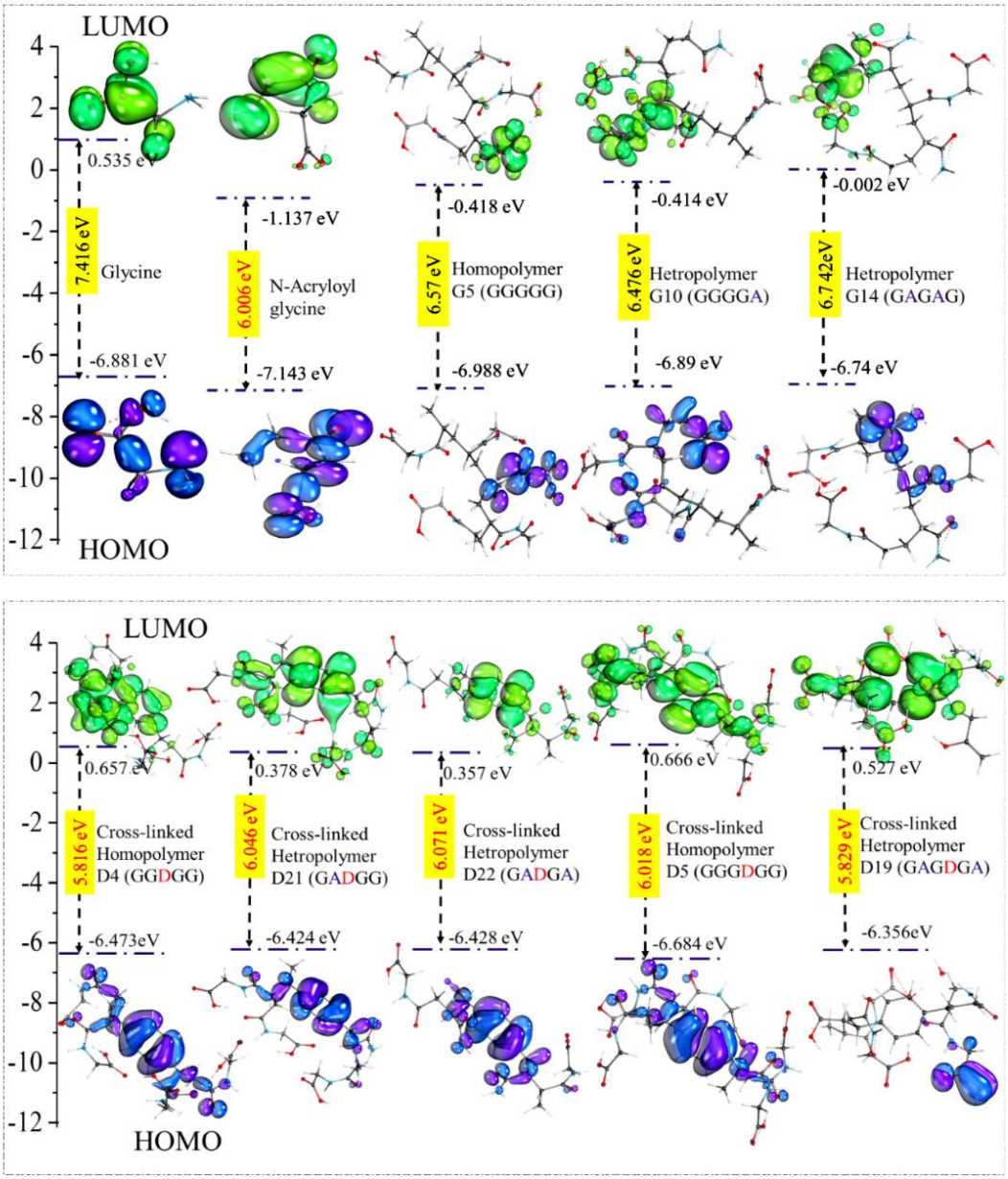

Figure 3.3. 2 Ground state HOMO, and excited state LUMO and energy band gap of (a) homopolymer of n-acryloyl glycine, (b) Linear hetro-polymer of N-acryloylglycine and acrylamide and (c) cross-linked monomeric to hexameric unit of p(NAG-b-A) polymer. (d) molecular orbital of glycine in HOMO to LUMO energy transfer, (e) molecular orbital of N-acryloyl glycine in HOMO to LUMO energy transfer, and (f) D4 and D22, D6 and D7

At molecular level, negative binding energy and H-bonding conformed to the strong protein ligand interaction, while the inhibition constant measures the therapeutic activity of the drug. PDBID-7PRT is a crystallographic structure of human heparanase, which was extracted from the PDB data source. The active form of heparanase is composed of non-covalently linked 50 kDa and 8 kDa subunits, enzymatic site near to Glu343, Arg 272 and two heparin binding domains such as I (Lys 159-Val 170) and II (Gln270-Lys280) as shown in Figure 3.3.3(a) [23]. Further, the molecular docking was performed with available potent inhibitor roneparstat, which is under Phase II trial and cyclophellitol is a natural glycosidase inhibitor and its derivative with heparanase 7PRT using Autodock tool (Figure 3.3.3). Similarly, Glycine, N-acryloylglycine and homo polymer of N-acryloylglycine and cross-linked hetro polymer of N-acryloylglycine and acrylamide were docked with heparanase (Figure 3.3.4 and Figure 3.3.5). Interacting binding energies for the reference molecules and 38 interacting residues are listed in Table 4. The inhibition constant (K_i) for cyclophellitol was calculated to be 823.53 µM and the five hydrogen bonds with Ser 422, Gln 424, Arg 465 were formed with the binding energy of -4.2 kcal mol^{-1} (Figure 3.3.3b). Roneparstat interacted with the binding energy value of -1.36 kcal mol^{-1} at 100.76 mM of K_i by forming the two hydrogen bonds with Asp 183 and Arg 382 residues (Figure 3.3.3c). Glycine interacted by forming only one hydrogen bond (Lys 232 residue) with -4.09 kcal mol^{-1} at K_i = 1 mM (Figure 3.3.4i) and N-acryloylglycine (Figure 3.3.4ii) interact at K_i = 166.36 µM lower than the shown reference value (Table 4) and by forming the four hydrogen bonds with higher binding affinity value –of 5.16 kcal mol^{-1} (Figure 3.3.5). By conversion of N-acryloylglycine monomer to homo polymer of six units the binding affinity increases from -5.16 kcal mol^{-1} to -7.62 kcal mol^{-1} and for cross-linked homo polymer of six mer units, the binding affinity increases from -6.83 kcal mol^{-1} to -10.45 kcal mol^{-1} along

with the increase in the number of hydrogen bonds. Linear homopolmer and cross-linked homopolymer mostly formed the hydrogen bonds at HBD II, with most common interacting residue Lys 280 for linear homopolmer and Arg 272 for cross-linked homopolymer (Figure 3.3.4 and 3.3.5, Table 3.3.4). Homopolmer G6 formed the 8 hydrogen bonds with binding affinity of 6.76 kcal mol^{-1} (K_i =11.16 µM) (Figure 3.3.5-xiii) and similarly cross-linked homopolmer formed 7 hydrogen bonds with binding affinity of -10.72 kcal mol^{-1} (K_i = 13.87 nM) (Figure 3.3.4b (xv)). Addition of acrylamide in linear polymer yielded the hetro-polymer, where the position and change in the number of acrylamide moieties affected the binding affinity and interacting residue sides as it is shown in Figure 3.3.4 and Table 4. When interactive sites were compared for dimer of acryloylglycine (G2) it is observed that it has interacted with HBDII by forming four hydrogen bonds, however, on introduction of acrylamide (GA) it interacted at HBDIII by forming 5 hydrogen bonds. Similarly, as shown in supporting Figure S3.3.1, with the introduction of acrylamide, the interactive sites are found more random and more than two units of acrylamide binding scores get decreased. Most of the copolymers with increasing the acrylamide units, interacted at the residue Ser 422, along with other residues such as GA1 (Figure 3.3.4(iv)), GA9, (Figure S3.3.1a), GA14 (Figure S3.3.1c) and GA15 (Figure S3.3.1b). This alteration mainly occurred due to the acrylamide units as AA dimer that interacted at HBDIII sites and random sites. As shown in Figure 3.3.4(vi-viii), in GA4 replacement of central unit A with DVB (D), the docking scores increased, whereas for hetropolymer of ADG the docking sores decreased with relatively higher extent than the GA4 (D2>D24>GA4). All the cross-linked hetropolymers majorly interacted at the heparin binding domain III with the interacting residues of Lys280, Lys231, Arg272, Arg273, Gln328 and Lys227 at lowest inhibitory constant at nano molar to micro molar concentrations (nM-µM).

This is also largely interacted at HBD III by forming H-bonds with Ser422, which is the evidence in support of the heparanase inhibitory activity of p(NAG-b-A) polymer. It is further observed that with the increase in acrylamide, the dock scores decrease as shown in Figure 3.3.4b (D4>D21>D22). We have considered the four units of glycine, one unit of acrylamide and one unit of cross linker with an optimum ratio for designing the polymer as D20. This shows dock sores equivalent to the homolinear polymer G6 (Figure 3.3.5xiii). The linear homopolymer above then G3 does not show any positive protease binding score. The linear hetro-polymer maximally shows the protease binding.

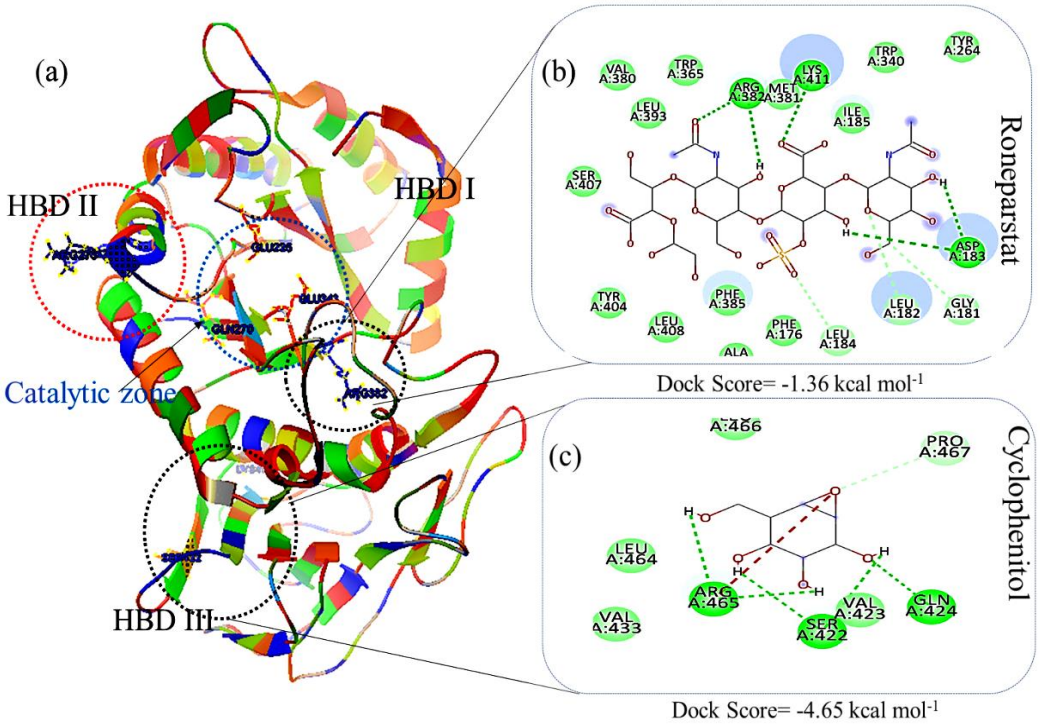

Figure 3.3. 33D protein structure of heparanase (7PRT) depicting the catalytic domains and heparin binding domains HBDI, HBDII and HBDIII. Docking poses a complex of (b) Cyclophellitol, and (c) Roneparstat with 7PRT.

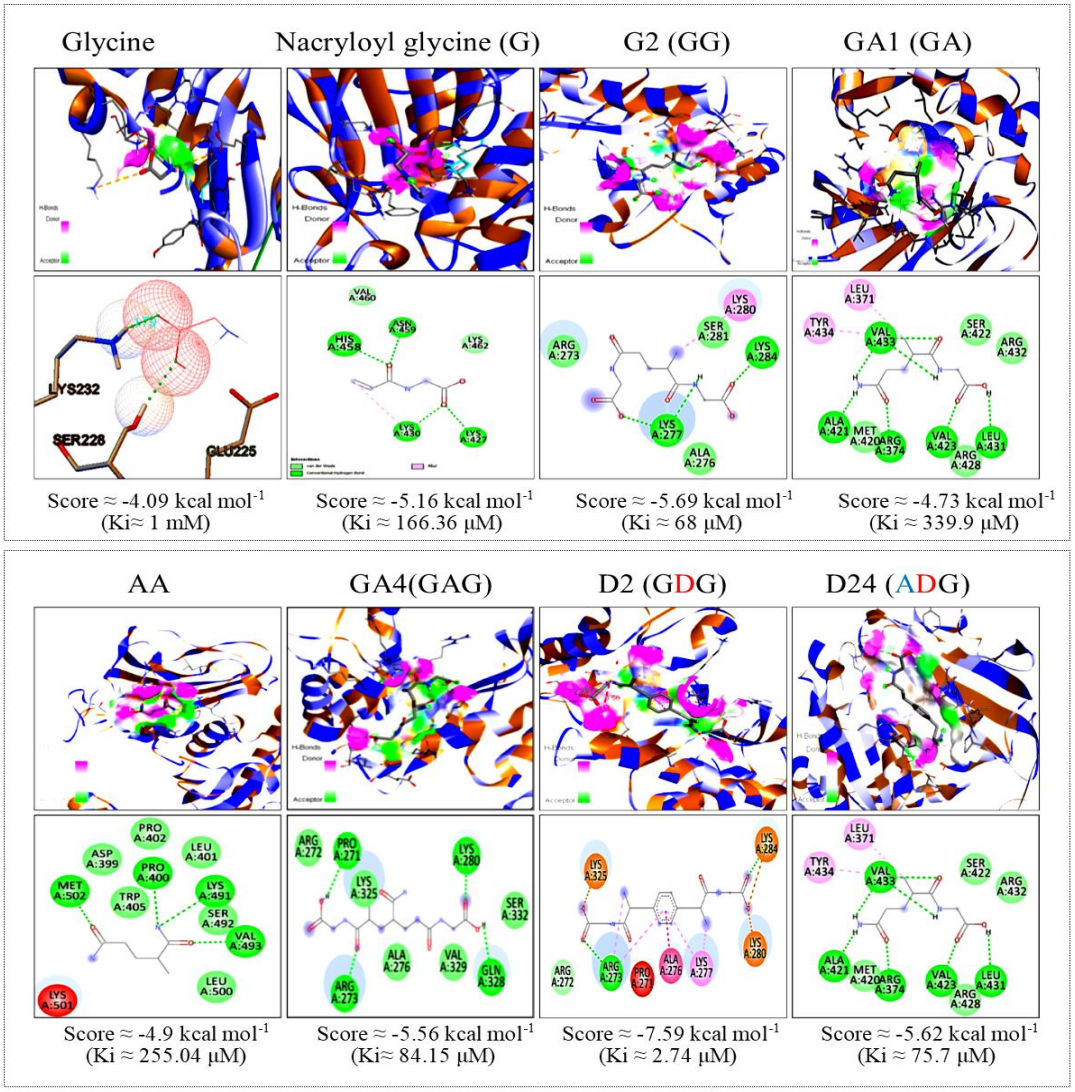

Figure 3.3. 4 Docking poses for complex of (i) Glycine, (ii) N-acryloylglycine, (iii) G2, (iv) GA1, (v) AA, (vi)GA4, (vii)D2 and (viii) D24 with 7PRT

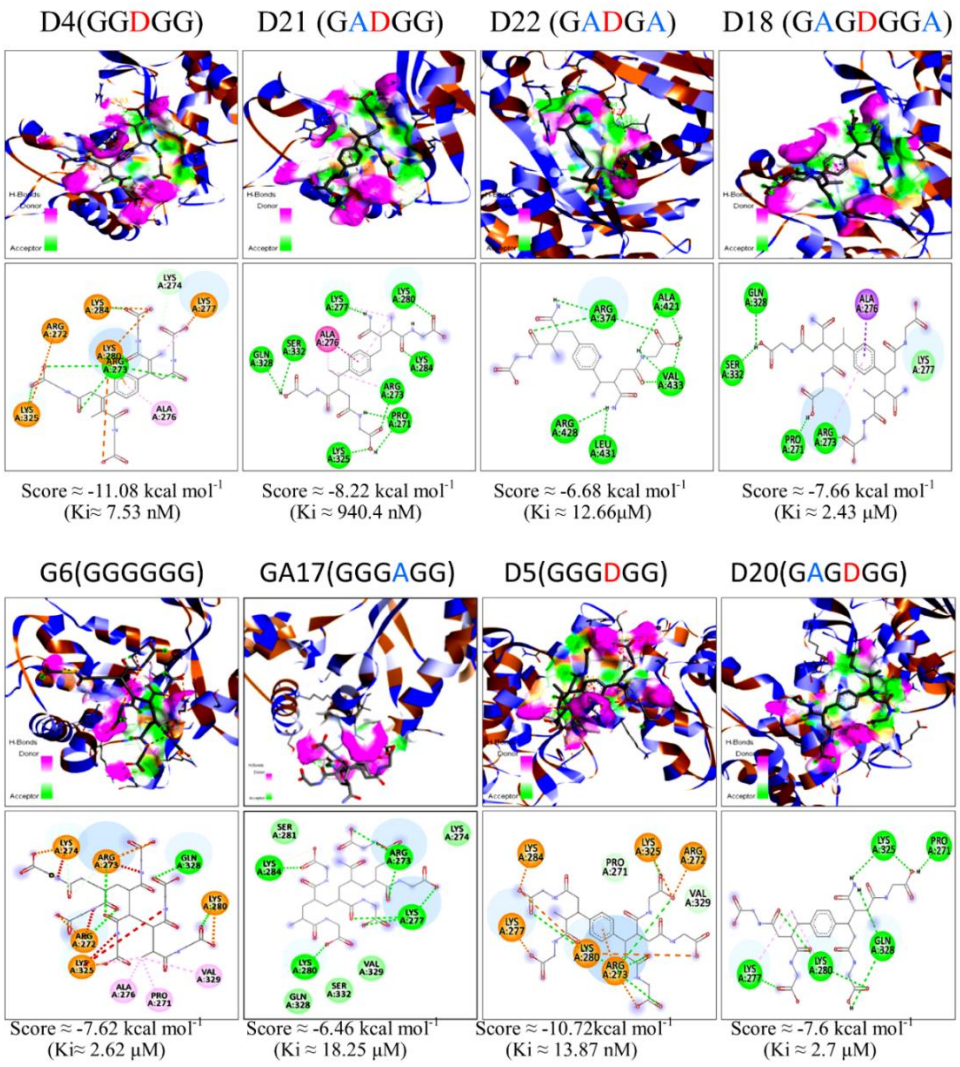

Figure 3.3. 5 Docking poses for complex for (ix) D4, (x) D21, (xi) D22, (xii) D18, (xiii) G6, (xiv) GA17, (xv) D5 and (xvi) D20 with 7PRT

However, the random interactions with heparanase may limit the heparanase activity. Furthermore, in cross-linked homopolymer upto D4 (Figure 3.3.5xi) exhibited a positive protease binding score, while above this shows negative protease binding score (Figure 3.3.1). Whereas for D20 shows both protease inhibitory and heparanase inhibitory activities (Figure 3.3.1 and Figure 3.3.5xvi).

3.3.4.4 Swelling index and biodegradation investigation of p(NAG-b-A). As reported in our previous studies, p(NAG-b-A) hydrogel was synthesized using a miniemulsion approach with the mechanism of free radical cross-linked polymerization (under publication).

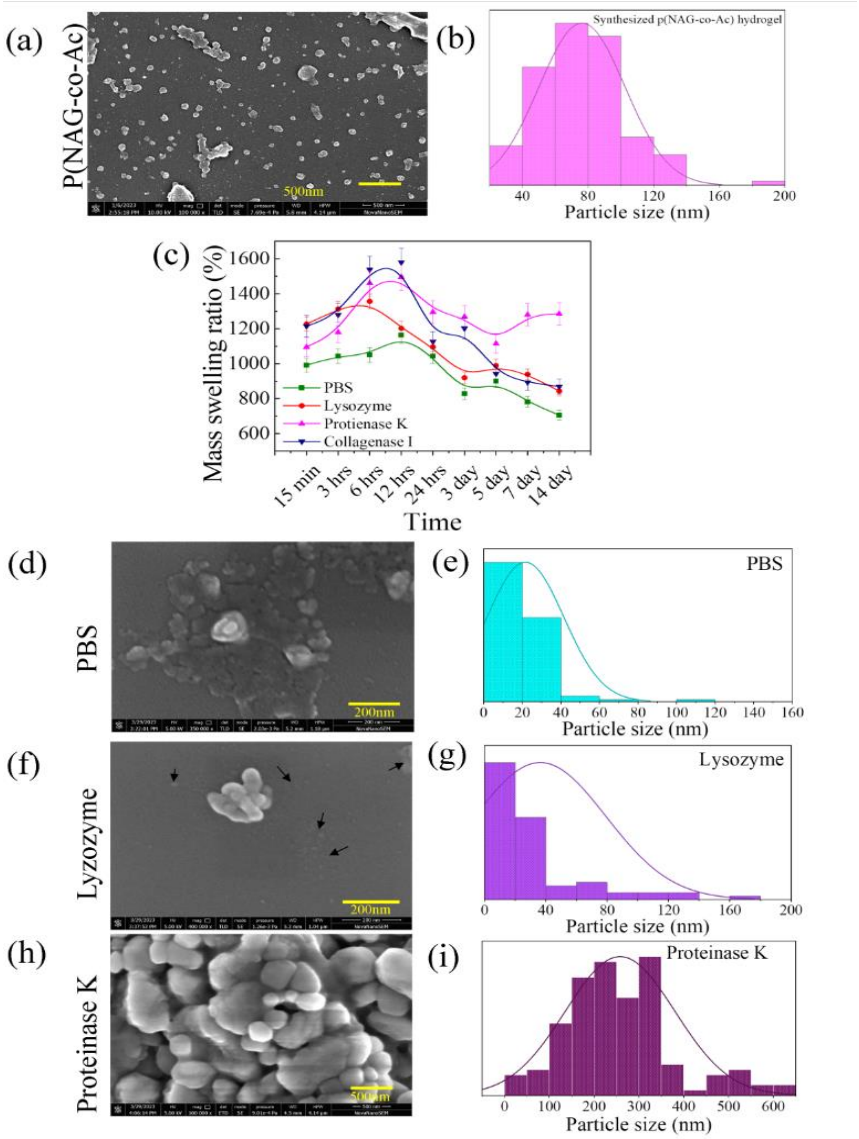

Figure 3.3. 6 Morphology, mass swelling ratio and degradation behavior of poly-[(N-acryloylglycine)-co-(acrylamide)] hydrogel in different enzymatic solutions. (a) FESEM micrograph of p(NAG-b-A), (b) particle size distribution obtained from Figure 3.3.1(a). (c) Mass swelling ratio of p(NAG-b-A) in PBS and different enzymatic solution lysozyme, proteinase K and collagenase I at the concentration 100 μg mL^{-1} of enzyme, (d-i) FESEM micrograph of degraded p(NAG-b-A) at 15^{th} day and particle size distribution using respective micrograph (d-e) p(NAG-b-A) in PBS, (f-g). p(NAG-b-A) in 100 μg mL^{-1} lysozyme, (h-i) p(NAG-b-A) in 100 μg mL^{-1} proteinase K.

Figure 3.3.1a depicts the FESEM micrograph of p(NAG-b-A) hydrogel, showing the spherical nanohydrogel with the particle size of 20-140 nm (Figure 3.3.6b) in diameter with an average particle size of 80 nm in diameter. Incorporation of DVB cross linker and acrylamide yield the high swelling behavior of the p(NAG-b-A) hydrogel particles (Figure 3.3.6c).

It is clearly evident that the swelling behavior of p(NAG-b-A) varied with different solution medium used, such as 1063.26 ± 46.53 % in PBS, 1202.17 ± 42.53 % in lysozyme, 1495.55 ± 74.77% in proteinase K, and 1579.59 ± 78.97% in collagenase I within 12 hrs of incubation, respectively. Decrease in mass swelling ratio can be corelated with degradation of p(NAG-b-A) as mass swelling ratio is found to be 706.12 ± 28.24% in PBS, 843.49±28.24% in lysozyme and 893.87 ± 43.46% in collagenase I at day 14^{th}. While the lowest degradation ~1280 ± 64.25% is observed in the solution of proteinase K solution at 5 min (see Figure 3.3.1c). On day 15^{th}, after re-lyophilization of degraded p(NAG-b-A) hydrogel, FESEM macrograph is obtained and the result is shown in Figure 3.3.6d, f and h and the distribution of the particle sizes are shown in Figure 3.3.6e, g and i. Decrease in size is clearly shown in Figure 3.3.6d and 6f of degraded p(NAG-b-A) hydrogel in PBS and lysozyme with reduction of particle size to 40 nm (Figure 3.3.6e) and 80 nm (Figure 3.3.6g) in diameter, respectively. However, in the presence of proteinase K, the size of p(NAG-b-A) hydrogel particles agglomerated into larger particles of size 100 nm – 400 nm in diameter, which is also one of the evidence for the protease inhibition activity. The protease inhibition activity further has been confirmed in the subsequent section in *in silco* results (Table 1).

3.3.4.5 p(NAG-b-A) hydrogel enhances the cytotoxicity in aggressive cancer: a comparative assessment. Glycine, at concentrations from 3 $\mu g\ mL^{-1}$ to 2.5 $mg\ mL^{-1}$, are viable on L929, Hek293, HepG2, A549, MDA-MB-231 and LN229 cell lines compared with

untreated control groups (P>0.05) (Figure 3.3.7). While on breast cancer cell e.g. MCF 7 cells glycine exhibits 80 % cell viability in all the concentrations (P<0.05) (Figure 3.3.7d). N-acryloylglycine has no effect on cell viability of L929, HepG2, and A549 cell lines as shown in Figure 3.3.7(a, c, and e - blue line); however, at the concentration of 1.25 mg mL^{-1}, it shows significant toxicity (P<0.05) in Hek293 (Figure 3.3.7b) and decreased the viability up to 80% in MDA-MB-231 and LN229 cell lines (Figure 3.3.7f and g). However, hydrogel is cell viable on the normal healthy L929, Hek293 and HepG2 cell lines (Figure 3.3.7 green line). However, upto the concentration of 1.5 mg mL^{-1}, p(NAG-b-A) is viable enough with the normal healthy Hek293 and HepG2 cell lines. Further, p(NAG-b-A) hydrogel has no significant toxicity effect on the MCF7 cell line upto 1250 μg mL^{-1} (P<0.05) (Figure 3.3.7b-c). However, P(NAG-b-A) hydrogel possesses a significant cellular toxicity on the aggressive cancer cells such as A549, MDA-MB-231, and LN229 with IC_{50} of 2.5 mg mL^{-1} in MDA-MB-231 cell line (Figure 3.3.7e-g) and IC_{50} of 625 μg mL^{-1} in LN229 cell line (P<0.05 or P<0.01) (Figure 3.3.7g). From the results it is clearly evident that the polymerized hydrogel exhibited a significantly higher cytotoxicity towards cancer cells then the monomer. Acridine orange (AO) and Propidium iodide (PI) staining images were acquired from confocal microscopy (Figure 3.3.8a), which represent the live, apoptotic and death events correspond to the respective emission of fluorescence of green, orange and red color. AO/PI staining was specifically conducted in MDA-MB-231 cell lines (Figure 3.3.8a), whereas on treatment with glycine and N-acryloyl glycine, more cells are alive compared to the untreated control of day 1 and day 3 treatments. Treatment with p(NAG-b-A) hydrogel induced the early apoptotic within day 1 in a dose dependent manner and more cells are dead compared to the untreated control group, glycine group and N-acryloylglycine group. Further, hemolytic activity of the N-acryloylglycine in

different concentrations of monomer is studied and found to be higher as compared to the p(NAG-b-A). The hemolytic percentage for monomer at different concentrations such as 62.5,125, 250, 500 and 1000 µg mL^{-1} are found to be -12.3580 ±0.056, -30.0772± 0.0051, 2.8169 ± 0.014, 17.3130± 0.178, and 14.3116±0.007, respectively (Figure S3.3.2). However, the hemolytic percentage of p(NAG-b-A) at different concentrations such as 62.5, 125, 250, 500 and 1000 µg mL^{-1} are found to be 0.14±0.09, 1.13±0.18, 1.58±0.46, 1.88±0.13 and 13.56±1.04 at 24 hrs, respectively (Figure 3.3.8b).

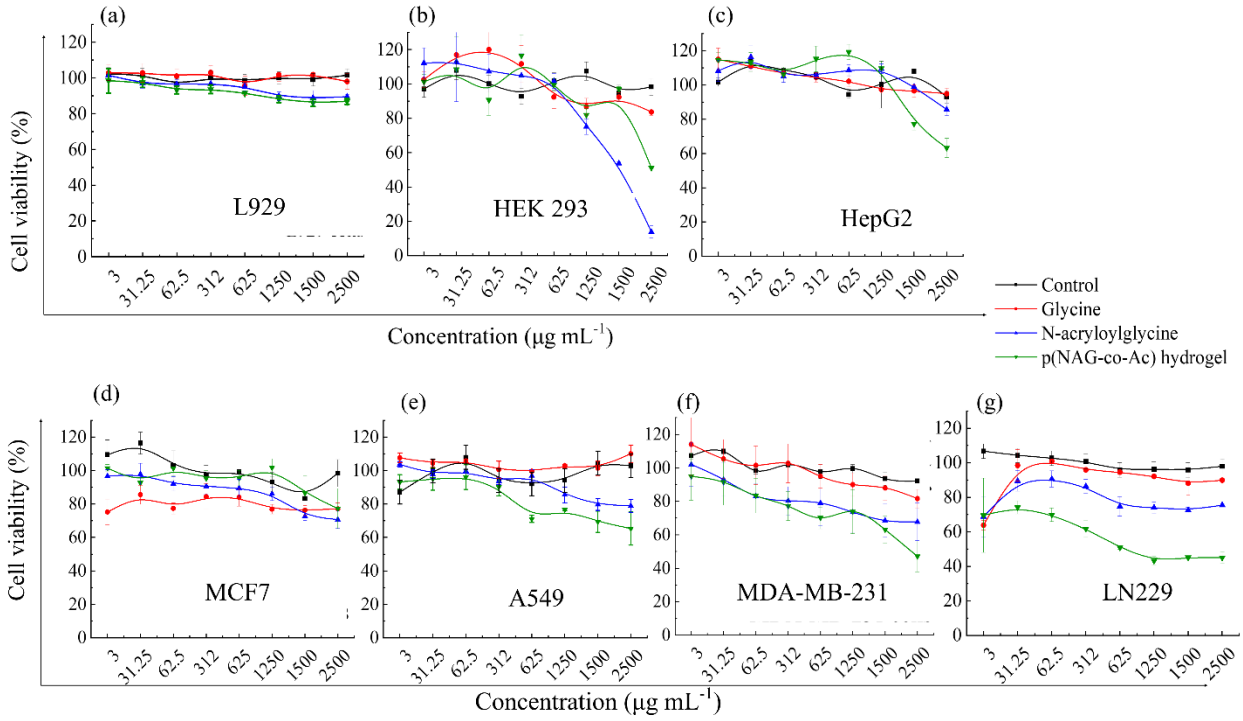

Figure 3.3. 7 MTT assay represents the cell viability results on (a) L929 (b) HEK 293 (c) HepG2 (d) MCF7 (e) A549 (f) MDA-MB-231 and (g) LN229 cell lines treated with different concentrations of glycine (red), N-acryloyl glycine (blue) and p(NAG-b-A) hydrogel (green)

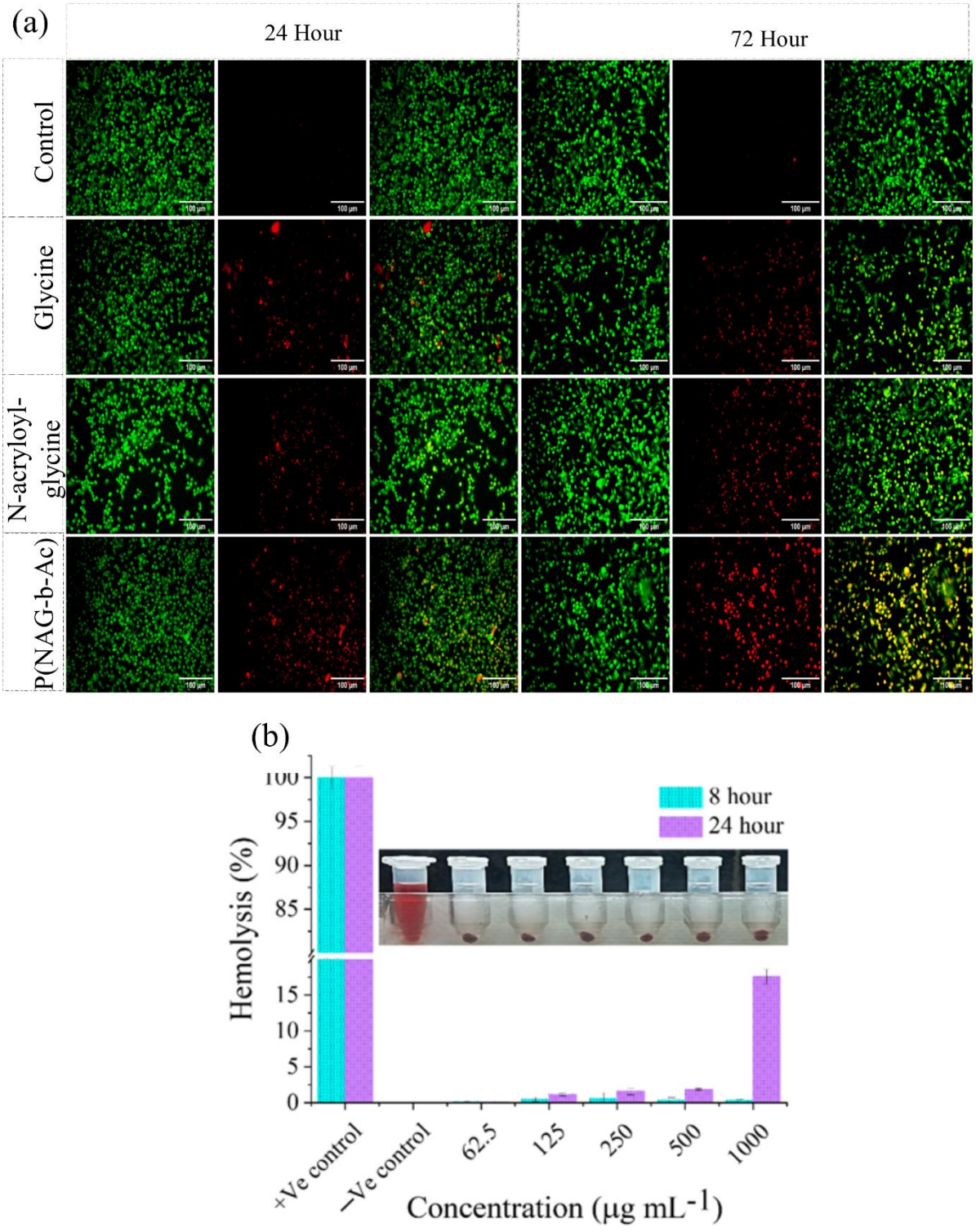

Figure 3.3. 8 (a) Live and dead assay studied via AO/PI staining of MDA-MB-231 cell lines treated with glycine, N-acryloylglycine and p(NAG-b-A) hydrogel, and (b) hemolysis percentage in treatment with p(NAG-b-A) hydrogel

3.3.4.6 **p(NAG-b-A) hydrogel selectively mitigate the cancer cell migration** Prognosis of metastases cancer gets worsened by the migration and invasion of cancer stem cells. Therefore, migratory mitigating effects of p(NAG-b-A) were investigated by the wound scratch assay performed on MDA-MB-231, LN229 cancer cell lines and L929 normal fibroblast cell lines. Glycine and N-acryloylglycine exhibited non-significant effect on migration of MDA-MB-231 and LN229 cancer cell lines; however, p(NAG-b-A) decreased the rate of migration of MDA-MB-231 and LN229 cancer cell lines. Wound closer percentage for untreated LN229 is found to be 29.44 ± 8.68 % and 46.94 ± 8.59 % (Figure 3.3.9), while wound closer percentage for untreated MDA-MB-231 is 8.10 ± % and 41.80±18.44% (Figure 3.3.10), respectively at the 24 and 48 hours of treatment. In LN229, glycine does not affect to wound closure rate, as wound closer percentage of glycine are 30.59 ± 4.76, 43.27±4.87 and 61.93 ± 0.98 % at dose of 50, 100 and 250 μg mL^{-1} and are non-significantly different from untreated control at 48 hr. While N-acryloylglycine and p(NAG-b-A) significantly inhibits the cellular migration of LN229 cell lines ($P<0.001$) (Figure 3.3.9) with wound closer percentage of 15.61±4.26, 5.79 ± 0.01, 7.22 ± 5.67, 11.30 ± 5.56, 12.72 ± 6.87, and 4.22 ± 3.55 % for dose of N-acryloylglycine at 50, 100 and 250 μg mL^{-1} and dose of p(NAG-b-A) hydrogel of 50, 100 and 250 μg mL^{-1}, respectively. Similarly, glycine, N-acryloylglycine and p(NAG-b-A) significantly inhibit the cellular migration of MDA-MB-23 cells at $P<0.001$ (Figure 3.3.10) with wound closer percentages of 15.41 ± 7.53, 19.21 ± 9.45, 3.41 ± 3.28, 2.26 ± 1.78, 2.27 ± 0.62, 6.05 ± 4.80, 7.69 ± 5.96, 2.60 ± 3.12, and -2.47 ± 9.70 % for the respective consequent three dose 50, 100 and 250 μg mL^{-1}, respectively. The wound closer % in L929 untreated control is calculated to be 16.56 ± 1.65 % at 24 h, and show non-significant migratory effect on L929 cells by p(NAG-

b-A) at 50 µg mL^{-1} (38.67 ± 3.86 %), 100 µg mL^{-1} (19.88 ± 12.82 %) and 250 µg mL^{-1} (20.15 ± 2.01 %).

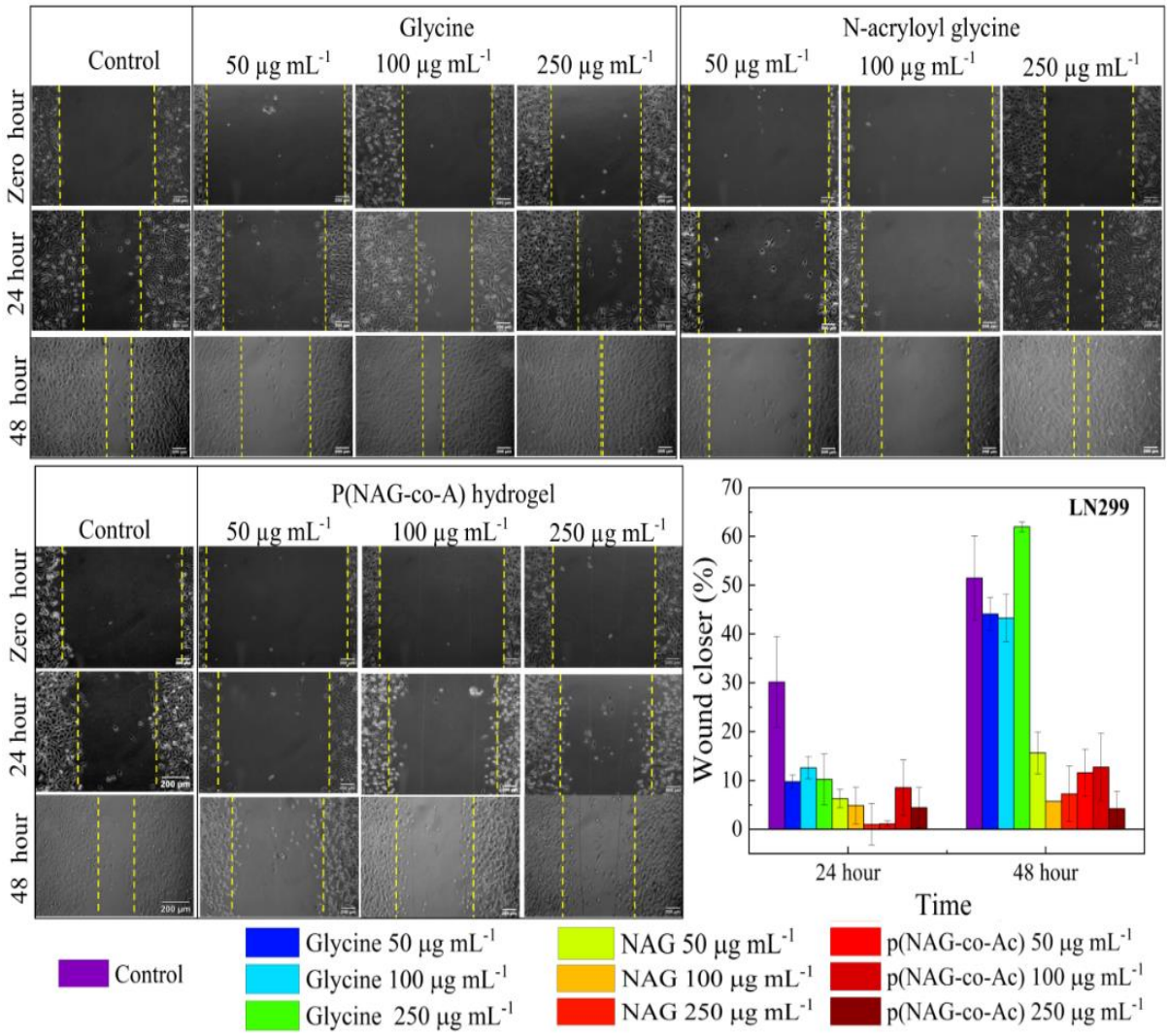

Figure 3.3. 9The in vitro wound scratch assay results obtained using LN229 glioblastoma cells by applying different concentrations (50 µg mL^{-1}, 100 µg mL^{-1} and 250 µg mL^{-1}) of samples. Results obtained for (a) glycine, (b) N-acryloyl glycine, (c) p(NAG-b-A) and (d) migration. The inhibition was measured in terms of wound closer percentage observed at 24 and 48 hrs

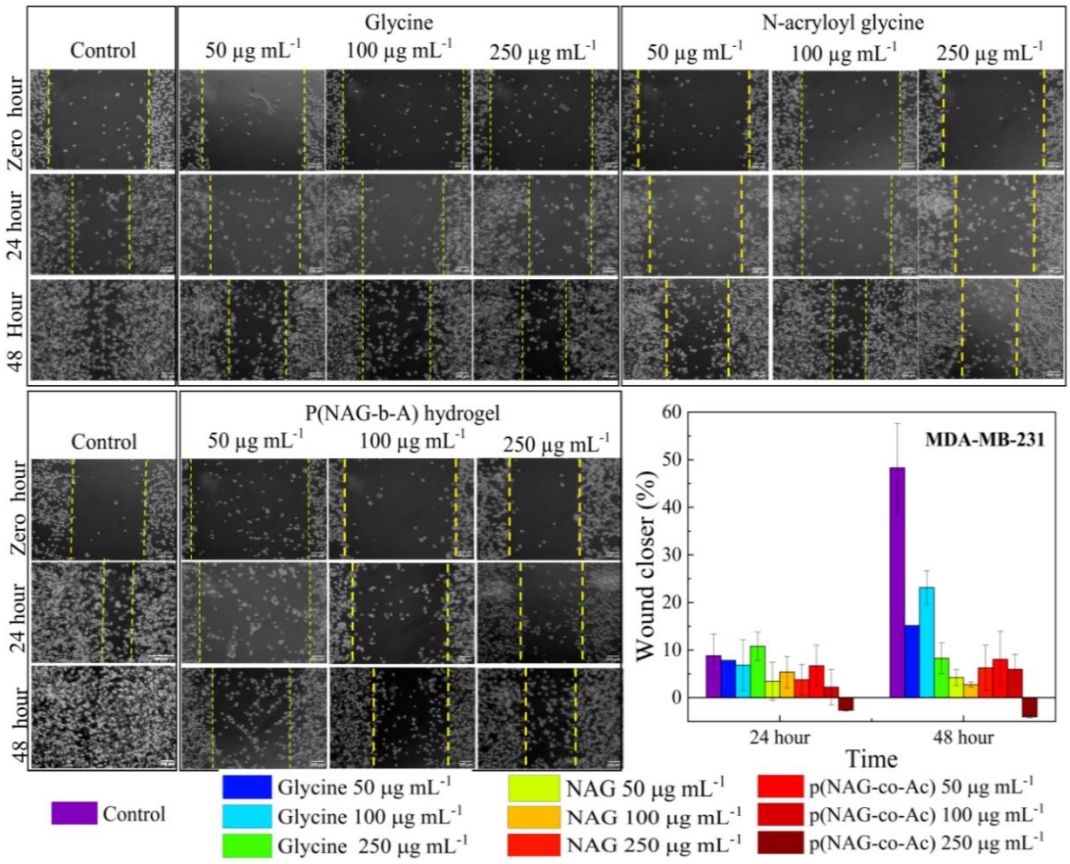

Figure 3.3. 10 The in-vitro wound scratch assay using MDA-MB-231 triple negative breast cancer cell line (TNBC) by applying different concentrations (50 µg mL-1, 100 µg mL-1 and 250 µg mL-1) of (a) glycine, (b) N-acryloylglycine, (c) p(NAG-b-A) and (d) migration. The inhibition was measured in terms of wound closer percentage observed at 24 and 48 hours.

3.3.4.7 p(NAG-b-A) hydrogel elevated the Reactive Oxygen Species (ROS) for apoptotic cell death .The quantitative apoptotic and necrotic death of LN229 cancer cell in response to glycine, N-acryloylglycine and p(NAG-b-A) hydrogel were investigated and the possible mechanism were evaluated using the flow cytometry apoptosis assay (Annexin V-FITC/PI) (Figure 3.3.11a). By considering the untreated sample as control reference and LN299 cell lines were treated with the 500 µg mL^{-1} and 1000 µg mL^{-1} of glycine, N-acryloyl glycine and p(NAG-b-A) hydrogel separately. In untreated control, 80 ± 2.15% cells are alive, 13.42 ±

1.83% are in the early apoptotic phase, 2.92 ± 0.23% are in the late apoptotic phase and 3.45 ± 0.21% are in necrotic phase. In response to the treatment with 500 μg mL^{-1} and 1000 μg mL^{-1} of glycine 58.75 and 52.14 cells are alive while major populations are showing necrotic phase with 21.32 % and 20.79 % at 24 hrs. In contrast to glycine, in treatment with N-acryloylglycine and p(NAG-b-A) hydrogel, the major cell population moved towards the early apoptotic death which shows the induction of apoptosis. At concentration of 500 μg mL^{-1} of N-acryloylglycine and p(NAG-b-A) hydrogel, 24.63 % and 23.12 %, respectively are moved towards the apoptotic death and at 1000 μg mL^{-1} concentration, 42.05 % and 36.88 % cell population remained in the early apoptotic death phase upto 24 h of incubation, respectively. Further to investigate the generation of ROS, dichlorofluorescein diacetate was used. Intracellular ROS was estimated in terms of peak shifting, which was compared with the H_2O_2 treatment as a positive control of ROS generation and untreated reference where ROS generation is found negligible (Figure 3.3.11(b-e)). In treatment with 160 μM H_2O_2, the oxidative stress is generated, these generated radicals that interacted with the dichlorofluorescein diacetate and cell fluoresce, which shown shifting of blue peak (Figure 3.3.11 b, c, and d) towards the left side. Similarly, shifting of peak positions (green and magenta peaks) for glycine (Figure 3.3.9b), N-acryloylglycine (Figure 3.3.9c) and p (NAG –co-Ac) (Figure 3.3.9d) depict that the synthesized p(NAG –co-Ac) which induces the apoptosis in LN229 cell lines by stimulating the generated ROS. However, from Figure 3.3.9e, it can be represented that the generation of ROS is followed in the order of Glycine ≥ N-acryloylglycine ≥ p (NAG –co-Ac) and the apoptosis of LN229 occurred accordingly.

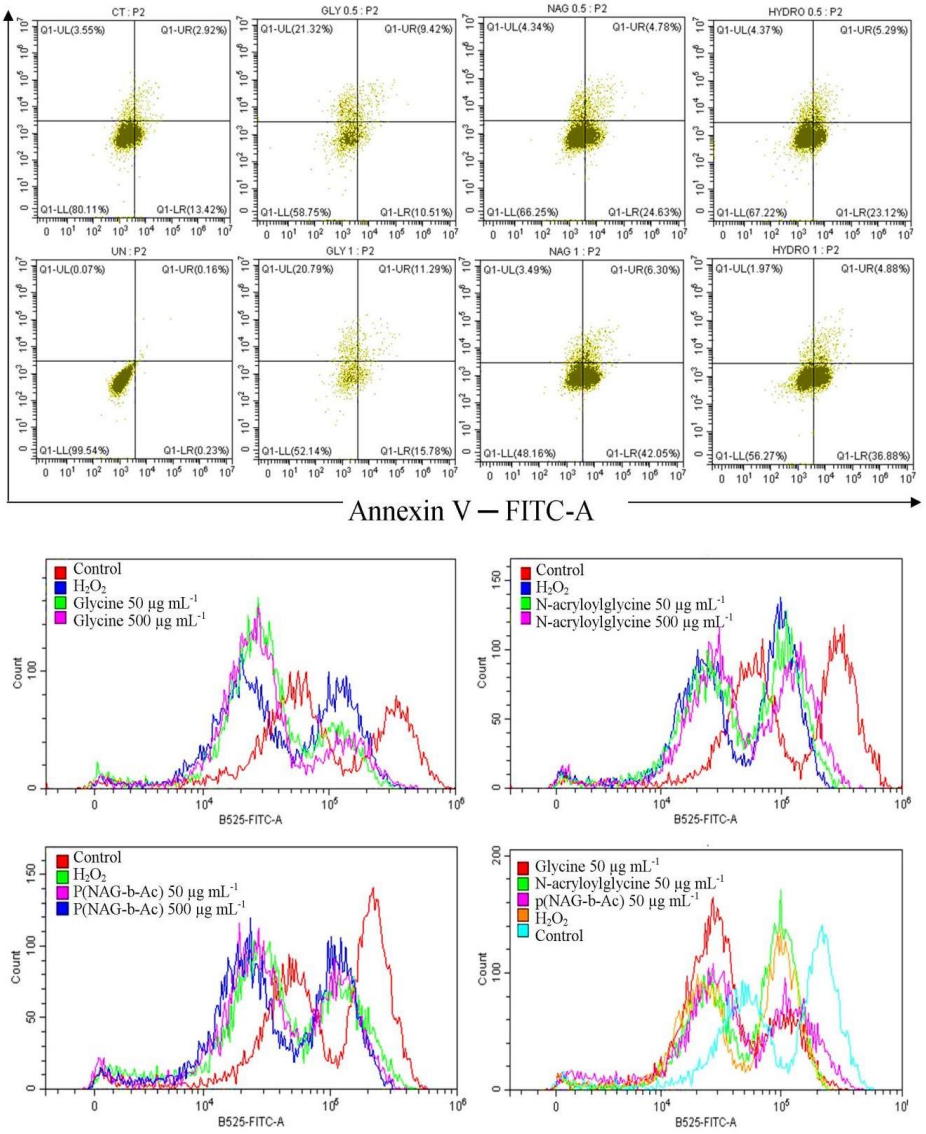

Figure 3.3. 11(a) Flow cytometry based quantitative analysis (using Annexin V/PI assay) of apoptotic and necrotic cell death induced by glycine, N-acryloylglycine and p(NAG-b-A) hydrogel and compared to the untreated reference control. (b-e) Intracellular ROS generation induced by (b) glycine at 50 and 500 µg mL^{-1}, (c) N-acryloylglycine 50 and 500 µg mL^{-1}, (d) p(NAG-b-A) hydrogel 50 and 500 µg mL^{-1}, and (e) comparison of intracellular ROS generation between Figure 3.3.11 b, c, and d.

3.3.4.8 p(NAG-b-A) hydrogel revealed as an anti-angiogenic material. Expression of cell surface heparanase induces angiogenesis and metastasis cancer. Therefore, CAM assay was performed to estimate the anti-angiogenic potential of p(NAG-b-A) hydrogel and compared

with N-acryloyl glycine monomer. Figure 3.3.12 exhibits for the lower doses such as for 2.5 and 25 μg mL^{-1} of N-acryloylglycine, and found there are vessel sprouting, however at the higher dose such as1000 μg mL^{-1}, there is irritation and blockage in mature vessels are observed. While from Figure 3.3.10a, it is evident that there is the reduction in area distributed by the vesseles. Further to evaluate the statistically significant angiogenic or anti-angiogenic effects of N-acryloyl glycine monomer and p(NAG-b-A) hydrogel, the acquired microscopic images were analyzed to check the change in percentage of vessels area, total vessel length, junction's density, total number of junctions and average vessel length using the Angio tool at the level of $p<0.05$. In treatment with different concentration of N-acryloylglycine (at 2.5 μg mL^{-1} and 25 μg mL^{-1}), a slight increase in the vessels area (at 2.5 μg mL^{-1} of 122.42 ± 3.32 %, at 25 μg mL^{-1} of 136.23 ± 21.36 %, for control112.42 ± 95%), total vessel length (at 2.5 μg mL^{-1} of 126.24 ± 0.57 %, at 25 μg mL^{-1} of 139.84 ± 26 %; control-115.71±10%), junction density (at 2.5 μg mL^{-1} of 102.68 ± 2.12 %, at 25 μg mL^{-1} of 136.14 ± 53.21 %; for control of 97.45 ± 8%) and total number of junctions (at 2.5 μg mL^{-1} of 131.94 ± 5.58 %, at 25 μg mL^{-1} of176.23 ± 83%; for control of 111.36 ± 19 %) have been calculated on 8 hour of treatment. Whereas, once it was treated with 1 mg mL^{-1} of monomer, the mentioned parameters were decreased with a negligible extent. However, differences in these values are non-significant at the level of $p<0.05$ compared to the control. Further, it has been identified that in treatment with different concentrations of p(NAG-b-A) hydrogel, the statistical significant decreases in vessel area, total vessel length, junction density, total number of junctions and average vessel length in all concentrations. Such as, the vessel area decreased by 38.4 ± 51 %, 54.03 ± 12.68 % ($p\leq0.001$) and 57.74 ± 27.36 % ($p\leq0.01$), total number of junctions decreased by 75.49 ± 19.48 % ($p\leq0.005$), 71.64 ± 19.09 % ($p<0.01$), and 44.6 ± 19.92 % ($p\leq0.01$), junction density

decreased by 63.12 ± 26.90 ($p \leq 0.005$), 78.46 ± 2.86% ($p < 0.001$), 36.78 ± 25.48 % ($p = 0.05$), total vessel length decreased by 26.24 ± 17.25 % ($p < 0.05$) 36.33 ± 12.87 % ($p \leq 0.005$), 14.71 ± 10.02 ($p > 0.05$) and average vessels length decreased by 81.86 ± 35.68 % ($p < 0.05$) 55.12± 34.72 ($p > 0.05$) and 72.64±48.19 ($P < 0.05$), respectively for the concentrations of 2.5 μg mL^{-1}, 25 μg mL^{-1} and 1 mg mL^{-1} of p(NAG-b-A) hydrogel.

3.3.4.9. **Heparanase inhibitory activity.** Synthetic pentasaccharide Fondaparinux sodium with a relative molecular mass of 1728Da is a commercially available substrate of heparanase. Heparanase hydrolyzes the Fondaparinux and generates the one-reducing terminal of glucuronic acid which were detected by resazurin with generation of fluorescent resofurin. Heparin and their derivative like N-acylated heparin derivative roneparstat are well known heparanase inhibitor which shows the 70% inhibition of heparanase at 1μg mL^{-1} concentration of heparin. Therefore in the present study heparin used as positive control and inhibitory activity of glycine, n-acryloyl glycine and p(NAG-b-A) were tested through Fondaparinux based inhibition assay. Glycine does not shown the heparanase inhibition while conversion of glycine to n-acylylglycine and p(NAG-b-Ac) shown the heparanase inhibition at the concentration of 250 ng mL^{-1}.Above the concentration of 250 ng mL^{-1} of the particle we observed almost equivalent % of heparanase inhibition as shown in figure. Our results corroborated that N-acryloylglycine and p(NAG-b-Ac) hydrogel having the heparanase inhibitory activity

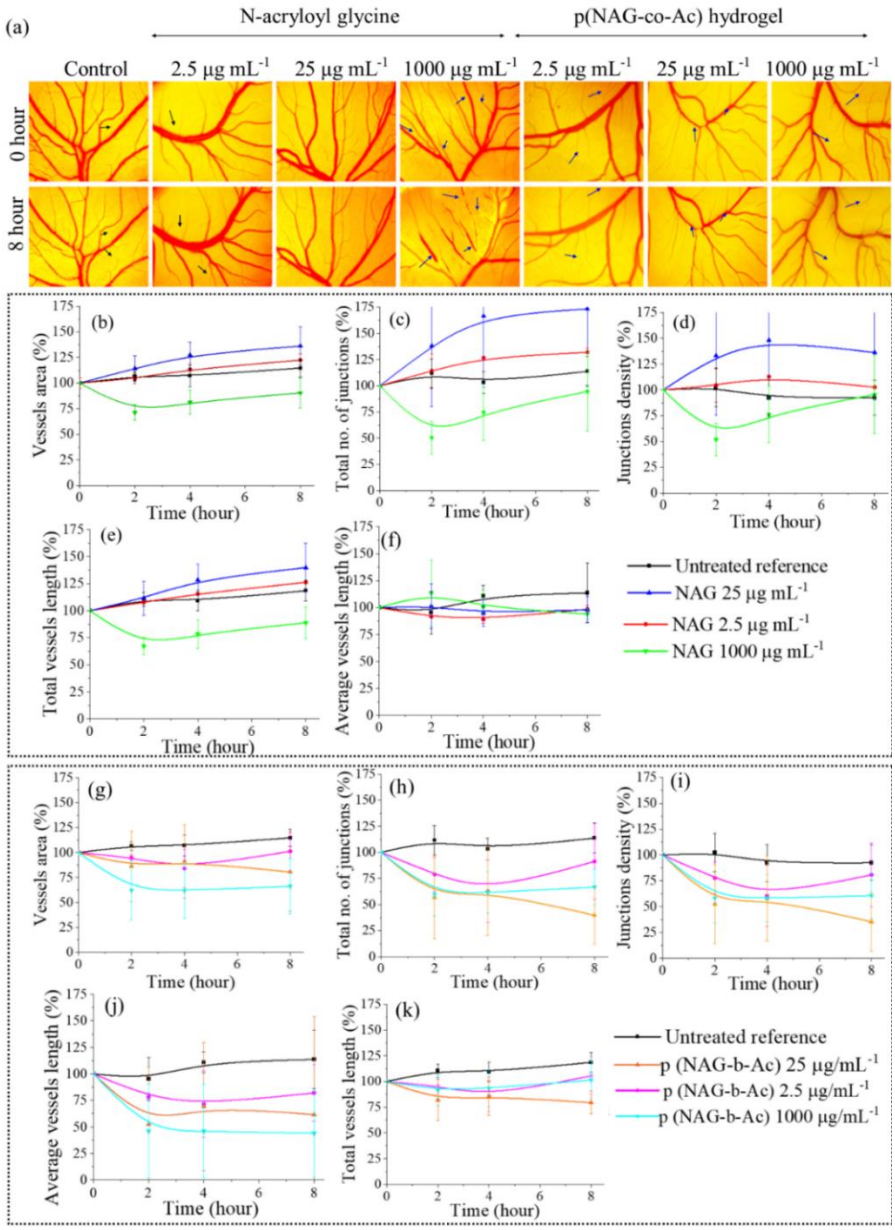

Figure 3.3. 12 Comparison of anti-antigenic effect of N-acryloylglycine and p(NAG-b-A) hydrogel. (a) In ovo CEA assay, in the presence of p(NAG-b-A) restricted the vascular sprouting (marked as black arrow) in dose dependent manner compared to N-acryloyl glycine. The change in vessel area, total number of junctions, junction density, total vessel length and average vessel length changed with dosing of: (b-f) N-acryloylglycine and (g-k) dosing of p(NAG-b-A) hydrogel as shown in time dependent manner with statistical significance level of $p<0.05$.

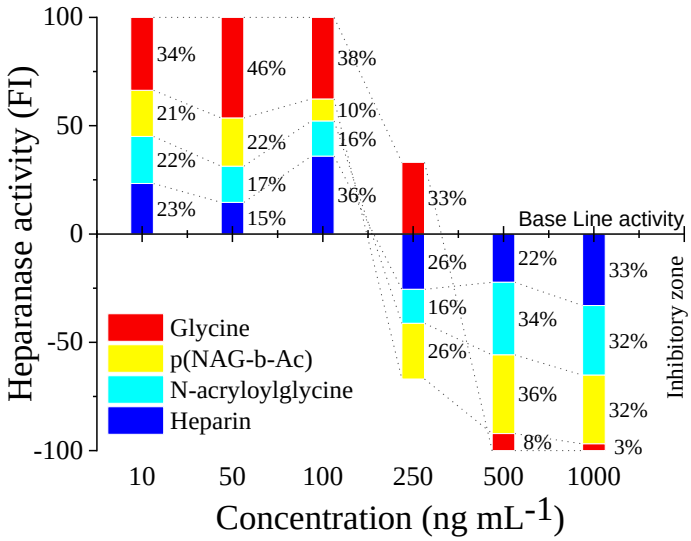

Figure 3.3. 13 Heparanase inhibitory activity of glycine, n-acryloyl and p(NAG-b-Ac)

3.3.5 DISCUSSION.

Herein, we have designed the anti-tumorigenic co-polymer for the heparanase driven malignancies. The major problems faced by researchers are the chemo resistance and heterpgenecity in cancer. Chemotherapy is a primary treatment in conventional cancer therapy but the drawback of this strategy is that chemotherapy induces the higher expression of heparanase [25, 26]. Heparanase promotes the aggressive malignant phenotype by creating the cancer stem cell niche within bone marrow microenvironment, [25] and regulates inflammatory signaling molecules. Therefore, it could be the major reason for the reoccurrence of poor prognosis cancer. For the designing of anticancer polymer for heparanase driven malignancies, we were inspired through the Bentolia research group, who developed the amino acid based polymer possessing the heparanase inhibitory activity. However, they have restricted their study for only homopolymer and the polymer was with M_w of 3000 Da to 60000 Da. Among the various amino acids, glycine was selected for further study due to the

prevention of cellular proliferation by dietary glycine [27], dose dependent biphasic role of glycine at lower concentration shows pro-angiogenic activity, while at higher concentration it possesses anti- angiogenic effect [28], and cardioprotective effect [29] which further takes important role in one-carbon (1C) metabolism. However, the role of glycine in cancer is still contradictory because of the involvement of serine/glycine in the 1C metabolism pathway. Although we did not find any reports till date which have shown glycine activity against heparanase, however benzoxazole is a heparanase inhibitor and functionalization with glycine improved the heparanase inhibitory potency. Therefore, in the present study, the comparative assessment has been done between glycine, N-acryloylglycine, homopolymeric of N-acryloylglycine, hetropolymer of N-acryloyl glycine, N-acrylamide and cross-linkers like homo and hetropolymers. Although computational approach like DFT for the understanding of mechanism of chemical process has a list of short comings, still it is able to reveal many insight knowledge on newly designed polymers' stability, chemical reactivity, biological activity and also gives a brief idea on underlying mechanism on the formation of molecule [24]. Here, the optimization of geometry and electronic properties for all the homo and hetero polymeric structures were performed using the well-established combination of basis set with force field (B3LYP/ 6-311g*). From calculation, it is observed that introducing N-acrylamide into homopolymer of N-acryloylglycine causes increase in the polarity and subsequently increases the dipole moment value, whereas introduction of DVB to homopolymer causes decrease in the dipole moment value. However, introduction of both acrylamide and DVB to the homopolymer causes again decrease in the dipole moment as well as accomplishes the formation of stable structure. These dipole moment values are quite important in accordance with the solvation parameters in selected solvents in a decreasing order of polarity.

Simultaneously, the HOMO and LUMO results for the cross-linked heteropolymers showed the decrease in band gap energy as compared to the homopolymers (Figure 3.3.2 and Table). Further, the introduction of cross-linkers and acrylamide provide an increase in the biological activity of the polymers with a potential role in anticancer activity. Further, synthesized polymers in biological system, most commonly interacted with G coupled protein receptors, nuclear receptors, ion channels, kinase and protease, and express the favorable pharmacological activity. Therefore, the prediction of bioactivity scores by DFT helps in determination of potential applications and pharmacological categorizations. Among all the random arrangements, most of the arrangements fall under the protease inhibitory categories (Figure 3.3.1). In malignant tumor protease production, activation and inhibition often disturb, which further implicate the tumor growth [6, 26] and hence, the inhibitors are considered as potent anticancer agents. In an attempt to establish the heparanase inhibitory potential, blind molecular docking was performed in the present work. Glu225 and Glu343 are critical residues for functional catalytic activity and Gln270–Lys280 residue heparin binding domain II, which is further responsible for the heparin binding, and Lys411–Lys417 and Lys427–Arg43 are the third potential interactive sites (IIIrd interactive sites) [24]. Deletion of Gln270– Lys280 residue results in the inactive enzyme, hence it is one of the potential domains for heparanase inhibitor development. Homopolymer majorly interacts at the heparin binding domain II, whereas with the introduction of acrylamide the hetero-linear polymer interacts at the third potential interactive site. With the introduction of DVB to homopolymer, it doesn't alter binding sites, however it induces the increased binding affinity towards the heparin binding domain II. Further, with the introduction of both DVB and acrylamide, majority of arrangements interact at heparin binding domain II with higher affinity at lower

inhibitory concentration then the homo/hetero-linear polymer and some cross-linked heteropolymers bind at the IIIrd interactive sites, which could be observed due to the formation of stable structure. Further, anticancer properties of p(NAG-b-A) were validated by *in vitro* studies. The synthesized p(NAG-b-A) is in 40 nm – 120 nm in size and showed the very high swelling behavior (1579.59 ±78.97 %) in presence of collagenase and 1063.26 ± 46.53 % in PBS (Figure 3.3.6). The swelling behavior is well correlated with the computational finding and we can consider that highest swelling may have occurred due to the increase in intermolecular hydrogen bonding energy (Table 2). Similarly, *in silico* protease inhibitory activity was validated and depicted in Figure 3.3.1 and Figure 3.3.6(h-i), where the p(NAG-b-A) hydrogel showed the biodegradation in PBS and in lysozyme, however in protease K solution with increase in agglomeration properties. We have also considered that the degradation products may yield the similar arrangements of hetro/homo polymers and may give the heparanase activity.

In vitro cytotoxicity of p(NAG-b-A) hydrogel has been studied and the results were compared with cytotoxicity of glycine and N-acryloyl glycine. The p(NAG-b-A) hydrogel showed higher cytotoxicity towards aggressive cancer cell lines then the normal healthy cell lines. N-acryloylglycine showed higher cell killing efficiency in HEK293 (Figure 3.3.7b), however it reduces by the formation of p(NAG-b-A) hydrogel. We observed the lack of cell killing effect of p(NAG-b-A) hydrogel in MCF7 (Figure 3.3.7d cell lines) which may be due to lowering the level of heparanase expression in MCF7 than the MDA-MB-231 (Figure 3.3.7f) and LN229 (Figure 3.3.7g). The expression data of heparanase in different cancer cell lines and in healthy cell lines have been represented in the supporting Figure S3.3.3 and Figure S3.3.4 was at obtained from the human protein atlas data bank. Further, p(NAG-b-A) hydrogel inhibits the

migration of MDA-MB-231 (Figure 3.3.9) and LN299 (Figure 3.3.10) cells and induces the apoptotic death in both the cell lines. In LN299 cells, the glycine induces the necrotic death which may be due to the excessive ROS generation, while p(NAG-b-A) hydrogel induces the programmed cell death by modulating the ROS production at therapeutic level as shown in Figure 3.3.11. We further observed the reduced vessel area, total number of junctions, junction density and total vessel length which demonstrate the anti-angiogenic behavior of p(NAG-b-A) hydrogel (Figure 3.3.12). This behavior may be observed due to the heparanase inhibitory potency of p(NAG-b-A) and the heparanase is tightly involved in the angiogenesis. As the database shows, the highest expression of heparanase was observed in esophageal cancers, bladder cervical and colorectal cancers etc.. We consider that this p(NAG-b-A) has a huge future scope of use in esophageal, cervical and colorectal cancer therapy due to its heparanase binding capacity.

3.3.6 CONCLUSIONS. In this work, p(NAG-b-A) hydrogel has been successfully synthesized. N-acrylolylglycine and acrylamide consisting of a linear and cross-linked arrangement shows the protease inhibitory positive score depicted by *in silico* investigation. With the increase in the dipole moment of the linear heteropolymer and in cross- linked heteropolymers, a decrease in the energy band gap is observed. Cross-linking induces the heparanase binding scores at lower K_i value in nanomolar concentration at the heparin binding domain II. *In vitro* study revealed that the anti-migratory, anti angiogenic, cancer cell killing potential of p(NAG-b-A) hydrogel in aggressive heparanase over expressive cancer cell lines is extraordinary. By increasing the ROS, p(NAG-b-A) hydrogel promotes programmed cell death in cancer. Revealing the cancer clearing mechanism at the molecular

level, the high swelling and drug loading potential will further elaborate the future scope of this anticancer polymer in esophageal, cervical and colorectal cancer therapy.

3.3.7. REFERENCES:

1. Noch, E.K., R. Ramakrishna, and R. Magge, *Challenges in the Treatment of Glioblastoma: Multisystem Mechanisms of Therapeutic Resistance*. World Neurosurgery, 2018. **116**: p. 505-517.
2. Mahmoud, R., P. Ordóñez-Morán, and C. Allegrucci *Challenges for Triple Negative Breast Cancer Treatment: Defeating Heterogeneity and Cancer Stemness*. Cancers, 2022. **14**, DOI: 10.3390/cancers14174280.
3. Jawalagatti, V., P. Kirthika, and J.H. Lee, *Targeting primary and metastatic tumor growth in an aggressive breast cancer by engineered tryptophan auxotrophic Salmonella Typhimurium.* Mol Ther Oncolytics, 2022. **25**: p. 350-363.
4. Fujita, M., S. Yamada, and T. Imai, *Irradiation induces diverse changes in invasive potential in cancer cell lines.* Semin Cancer Biol, 2015. **35**: p. 45-52.
5. Eatemadi, A., et al., *Role of protease and protease inhibitors in cancer pathogenesis and treatment.* Biomedicine & Pharmacotherapy, 2017. **86**: p. 221-231.
6. Hong, X., et al., *Increased chemotactic migration and growth in heparanase-overexpressing human U251n glioma cells.* Journal of Experimental & Clinical Cancer Research, 2008. **27**(1): p. 23.
7. Zahavi, T., et al., *Heparanase: a potential marker of worse prognosis in estrogen receptor-positive breast cancer.* npj Breast Cancer, 2021. **7**(1): p. 67.
8. Rodrigues, A.A.N., et al., *Heparanase 1 Upregulation Promotes Tumor Progression and Is a Predictor of Low Survival for Oral Cancer.* Front Cell Dev Biol, 2022. **10**: p. 742213.
9. Vornicova, O., et al., *The prognostic significance of heparanase expression in metastatic melanoma.* Oncotarget, 2016. **7**(46): p. 74678-74685.
10. Barash, U., et al., *Heparanase promotes glioma progression via enhancing CD24 expression.* Int J Cancer, 2019. **145**(6): p. 1596-1608.

11. Yousefi Rizi, H.A., D. Hoon Shin, and S. Yousefi Rizi, *Polymeric Nanoparticles in Cancer Chemotherapy: A Narrative Review.* Iran J Public Health, 2022. **51**(2): p. 226-239.
12. Tavares, M.R., et al., *Polymer-Based Drug-Free Therapeutics for Anticancer, Anti-Inflammatory, and Antibacterial Treatment.* Macromolecular Bioscience, 2021. **21**(8): p. 2100135.
13. Mukherjee, I., et al., *Side-Chain Amino Acid-Based Cationic Antibacterial Polymers: Investigating the Morphological Switching of a Polymer-Treated Bacterial Cell.* ACS Omega, 2017. **2**(4): p. 1633-1644.
14. Kim, B., et al., *Dual Acid-Responsive Micelle-Forming Anticancer Polymers as New Anticancer Therapeutics.* Advanced Functional Materials, 2013. **23**(40): p. 5091-5097.
15. Takahashi, H., et al., *Anticancer polymers designed for killing dormant prostate cancer cells.* Scientific Reports, 2019. **9**(1): p. 1096.
16. Hanwell, M.D., et al., *Avogadro: an advanced semantic chemical editor, visualization, and analysis platform.* Journal of Cheminformatics, 2012. **4**(1): p. 17.
17. Neese, F., *Software update: the ORCA program system, version 4.0.* Wiley Interdisciplinary Reviews: Computational Molecular Science, 2018. **8**(1): p. e1327.
18. Morris, G.M., et al., *AutoDock4 and AutoDockTools4: Automated docking with selective receptor flexibility.* Journal of computational chemistry, 2009. **30**(16): p. 2785-2791.
19. Biovia, D.S., *Discovery studio modeling environment*. 2017, Release.
20. Adekoya, O.C., et al. *Application of DFT Calculations in Designing Polymer-Based Drug Delivery Systems: An Overview*. Pharmaceutics, 2022. **14**, DOI: 10.3390/pharmaceutics14091972.
21. Chen, M., et al., *Role of hydrogen bonding in hysteresis observed in sorption-induced swelling of soft nanoporous polymers.* Nat Commun, 2018. **9**(1): p. 3507.
22. El-Shamy, N.T., et al. *DFT, ADMET and Molecular Docking Investigations for the Antimicrobial Activity of 6,6′-Diamino-1,1′,3,3′-tetramethyl-5,5′-(4-chlorobenzylidene)bis[pyrimidine-2,4(1H,3H)-dione]*. Molecules, 2022. **27**, DOI: 10.3390/molecules27030620.

23. Levy-Adam, F., et al., *Identification and characterization of heparin/heparan sulfate binding domains of the endoglycosidase heparanase.* J Biol Chem, 2005. **280**(21): p. 20457-66.
24. Mary, Y.S., et al., *Investigation of the reactivity properties of a thiourea derivative with anticancer activity by DFT, MD simulations*. 2021.

CHAPTER 3: Results and Discussion (Part IV)

Objective IV: Synthesis and characterization of polymeric nanoparticles for siRNA and drug delivery for Cancer treatment.

3.4.1. ABSTRACT. Herein this work new polymeric nanoparticles were synthesized and formulated with newly designed siRNA and chemotherapy drugs for aggressive cancer treatment. The vast heterogeneity of tumors, negative expression of receptors like HER-2, estrogen (ER) and progesterone (PR) receptors in triple-negative breast cancer (TNBC), invasive nature and high recurrence rate are the major challenges in poor prognosis aggressive cancers. High expression of heparanase, L-amino acid transporter (LAT1), and RNA polymerase II (POL2RA) are majorly responsible for the proliferation and invasion of cancer cells. In this line, morphologically spherical, and amorphous acrylate p(NAPA-co-LME) copolymer nanoparticles were synthesized and characterized for physical and biological properties. Formation block-co-polymer p(NAPA-co-LME) nanoparticles reveled with decreased in zeta potential of -28 compared to homopolymeric particle zeta potential-38 to -35 mV. High molecular weight phenylalanine and leucine-based polymers elucidated for it heparanase inhibitory activity that accelerate the cancer treatment. Side chain containing amino acid-derived polymers exhibit significant properties such as stimuli responsiveness, self-assembling characteristic behavior, presence of amino group and -COO favors the interactions

with drug and small molecule such as siRNA. p(NAPA-co-LME) polymer is cytocompatibility in L929 and PC12 cells induce the cellular internalization through the LAT1 transporter and clathrin mediated endocytosis. The presence of aromatic rings in these polymers enhance the loading efficiency of siPOL2RA up to 70% and additionally a higher loading efficiency is observed for the drug along with the silencing of POL2RA. The chemical modification of the nanoparticles induces the serum stability of siRNA. POL2RA expression is also correlated with the other cancer overexpressed marker such as cyclin-dependent kinase. The silencing of POL2RA alters the expression of CDK and finally induces programmed death of the cancer cells. Overall these siRNA drug-loaded polymeric nanoparticles possess a multi-targeting promising potential in the treatment of advanced-stage cancer in a targeted manner.

3.4.2. INTRODUCTION

The RNA interference is the process of repression of gene expression through the 22nt stranded siRNA. It is widely utilized to interrogate molecular biology questions [1]. RNA chemistries are continuously evolving and the success of RNAi technology can be rated by currently approved RNA drugs. However, to date, none of the siRNA-based therapeutics has reached the goal of the clearance of the phase 3 clinical trials.[2] This could be due to the labile nature of siRNA, as siRNA is negatively charged, highly water soluble, and cannot internalized passively, therefore, less cellular uptake and degradation in endo-lysosomal escape is occurred. It is important to optimize the chemical architecture of RNA to build the drug-like properties or it is required to shield the siRNA using polymers, lipids, or nanoparticles to overcome the challenges in therapeutic settings. Due to having the ability to silence oncogenes and multi-drug resistance genes, it is considered as a siRNA drug that can help to overcome the limitations of existing cancer therapy.

According to the WHO, cancer is the second leading cause of death, worldwide and new medicines are required for better treatment efficiency. Aggressiveness of the cancer is associated with the metastasis, the worst pattern of invasion, high mortality even in early diagnosis and a shortened survival rate. One of the common features in aggressive cancer/poor prognostic cancer is overexpressed multifunctional heparanase. This molecule is involved in angiogenesis and regulation of gene transcription [3]. Presence of nuclear heparan sulfate inhibits the histone acetyl transferase followed by the inhibition of gene transcription. While increased expression of heparanase activates the HAT, which leads the transcription of oncogene. It further induces the differentiation of normal tumor to aggressive phenotype. Therefore, heparanase bio-marker is considered as the hall mark of the cancer [3, 4]. Heparanase further enhances the risk for reoccurrence of cancer [5]. As mentioned in earlier chapter-3 Part III, we had clearly mentioned about the heparanase inhibitory potential of p(NAG-b-Ac) hydrogel along with the anticancer property. Therefore, to develop synergistic nano vehicles for the siRNA and drug delivery, we have explored for the first time the heparanase inhibitory potential of synthesized polymeric nanoparticles for the therapy of aggressive cancer such as TNBC.

TNBC and Glioblastoma are aggressive form of cancers, where chemotherapy is a first line therapy. Absence of receptors restrict the use of hormone therapy and chemotherapeutic drug for these type of cancers. First line chemotherapeutic agent paclitaxel, directly induces the cell apoptosis. However, due to poor water solubility ($0.03 \mu g\ mL^{-1}$)/limited bioavailability (<10%), efflux through multidrug transporter P-gp, lack of cell specificity and various side effects, therapeutic use of paclitaxel has been limited [6-8]. It has been considered that simultaneous delivery of siRNA which silence the gene responsible for drug resistance and drug to activate

cell apoptotic pathway may become an effective strategy and give the synergistic effects [9]. Chemo-gene therapy is a promising idea, perhaps selection of target, designing of nanovehicle which could co-deliver polyanionic siRNA and hydrophobic drug is challenging and specificity towards the cancer specific without off targeting is major concern. Many nano platforms like liposomes [10], dendrimer [11], supramolecules [12] and silica nanoparticles [13] etc. [14] were also used for this purposes, however none of them is approved for the clinical application However, still there is a huge scope to explore this area as still none of the siRNA based anticancer therapy/co-therapy got the FDA approval.

Over the conventional pharmaceutical formulations, polymeric carriers become the efficient for nucleic acid delivery and the hydrophobic drug. For the delivery of siRNA, polyamine, polyethylenimine, polysaccharides and polyaminoacids catches the much attention due to superior transfection efficiency. However cytotoxicity is an another major concern [9]. Cavallaro et al. mentioned that ideal carriers need to be amphiphilic or water soluble for efficient gene target. Among the aminoacid based polymers such as Poly L-lysine based cationic polymers offer the good loading capacity and form a polyplex with siRNA. High molecular weight of polymer shows deleterious effects and induces the necrotic cell death [15]. Anionic polymers decrease the toxicity towards the cells, but for the efficient siRNA delivery they require the introduction of cationic functional groups [16], or can develop the acrylate based polymers to reduce positive charge density and to enhance cell viability, or can create the copolymer to achieve the target specific delivery. Similarly, in this work we hypothesized that aromatic ring containing polymer could be a potential candidate in siRNA delivery, specifically towards the cancer therapy. These hypothesis was considered because of the role of aromatic rings in stabilization of siRNA, induces RISC mediated antisense strand selection

and silencing [17] and phenolic compound of oligomer enhances the endosomal buffer capacity [18]. Dense phenolic hydroxyl group act as an electron donor and forms the intermolecular complexes with phosphate groups of siRNA, and they simultaneously enhances the cellular uptake and gene silencing performance [19, 20].

Another important characteristics of cancer is the requirement of massive supply of amino acid and nutrients. To fulfill the requirement, amino acid transporter LAT 1 receptor is highly expressed in various types of cancers, such as hormone resistant prostate cancer [21], melanoma [22], and it is also considered as the hallmark for cancer [23, 24]. The highest expression of LAT1 was found to be 84.4% in luminal A subtype and 82.9% in triple negative subtype breast cancer compared to the 64.3% in triple positive subtype breast cancer. Therefore, we considered that development of amino acid based siRNA/drug delivery amino acid based co-polymeric nanoparticles could accumulate better in tumor cells, and will be the potential approach to deliver the drug and siRNA at the target site.

Our research group is focused towards the development of biocompatible acrylate-amino acid based polymers. Our research group members had already synthesized p(NAPA) and (pLME) polymers nanoparticles which exhibited the adjuvant properties on the innate immune system [25] and exhibited antioxidant potential on macrophage [26]. But the co-polymer was not explored. [26]. [25]

As per previously reported studied by bentolia research group, they have shown that phenylalanine polymer and leucine polymer exhibits the heparanase inhibitory property, however the molecular weight of these polymer was higher. In aggressive cancer, high expression of heparanase, L-amino acid transporter (LAT1), and RNA polymerase II (POL2RA) are majorly responsible for the proliferation and invasion of the cancer cells.

Increased expression of heparanase activates the HAT, which leads the transcription of oncogene. To incorporate the synergistic activity against cancer like heparanase inhibitory and drug/siRNA delivery potential, we explored the designing of p(NAPA-co-LME) NPs. To the best of our knowledge none of the polymeric nanoparticle/co-delivery system explored for heparanase inhibitory activity.

In the present study we have developed the p(NAPA-b-LME) copolymers for the delivery of siRNA and paclitaxel. Further we have targeted towards the POLOR2A gene silencing as POLOR2A expression is correlated with poor clinical outcome. POLOR2A is an oncogene and essential for transcription, represses the apoptosis in tumor and induce the transcription. Hence, silencing of POLOR2A is consider to be a promising approach for the therapy of various cancer like TNBC [27] [28], renal cancer, colorectal cancer [29] and in lung cancer [30]. In this line, herein this work we have developed p(NAPA-co-LME) nanoparticles and analyzed for the LAT1 mediated internalization mechanism and the cancer therapy mechanism. First we have synthesized the p(NAPA-co-LME) nanoparticles and they have been characterized and asses the fitness for the biomedical applications through the various toots and biochemical assays. siRNA has been designed targeting to the POLOR2A gene silencing. siRNA and paclitaxel were formulated with p(NAPA-co-LME) nanoparticles. Finally, the efficiency of the treatment of the TNBC using these formula has been studied. Finally, POLOR2A gene silencing was estimated for the cancer therapy. Finally, the extent of TNBC killing efficiency and their mechanism have been elucidated.

3.4.3. MATERIALS AND METHODS:

Materials used in this work are listed in the experimental section and other materials were used for doing the experiments are mentioned in the subsequent sections.

3.4.3.1. **Synthesis of N-acyloyl leucine methyl ester**. In brief, 10 mMol of L-luecine methyl ester hydrochloride was dissolved in 60 mL of dry DCM and then 1.6 mL of triethylamine was added with slow stirring in ice bath. Afterword chilled 1.1 eqv. (0.9 mL) of N-acyloyl **chloride** in 5mL of dry DCM was added drop wise for 1 h and kept under stirring for another 12 h at 25^{o}C. DCM from the reaction mixture was removed by rotatory evaporator. The obtained product was dissolved in ethyl acetate (100 mL) and the triethylamine hydrochloride crystals were separated through filtration. Then the solution was washed three times with 1M $NaHSO_4$ and 5% $NaHCO_3$ (about 20 mL), respectively and finally with a brine solution. Magnesium sulfate ($MgSO_4$) was used for removing water and then organic solvent was evaporated using vacuum drying by rota-evaporator at low pressure. The monomer was characterized by FTIR, ^{1}H NMR and ^{13}C NMR and used for further process without purification.

The N-acryloyl phenylalanine methyl ester monomer was synthesized in a similar way as mentioned for LME synthesis using the initial reagent N-acryloyl phenylalanine methyl ester.

3.4.3.2. **Synthesis of p(NAPA-co-LME) NPs, p(NAPA)NPs and p(LME) NPs.** Poly ((N-acryloyl phenylalanine methyl ester)-co-(N-acyloyl leucine methyl ester)) (p(NAPA-co-LME)) was synthesized by mini-emulsion polymerization approach. Briefly, 250 mg of NAPA and 250 mg LME, first evenly dispersed in 1.15 mL of toluene using a bath sonicater for 5 minutes and 20 minutes of vertex. After complete dispersion 10mg of hexadecane and 30 mg of DVB and 10mg of AIBN were added after each 5 min of interval with continuous vertaxing and then 22 mg/ 8 mL of SDS solution (H_2O) was added and vertex for 30 min. Then the whole mixture was further sonicated for another 7 mins using ultra-probe sonicator (750W, 30% amplitude), at 0^{o}C (in ice bath) for allowing the formation of emulsion. Then the emulsion was

transferred into a round bottom flask (25 mL) and the vigorous stirred at 70 °C, in oil bath for 24h for complete polymerization. Toluene was removed by addition of 50 ml water to the dispersion and this was stirred for 24 h in an open vial. Then, white polymer product (capsules) was washed repeatedly with water and ethanol mixture (1:1 ratio) and centrifuged at 14000 RPM. Further synthesized product were characterized through FTIR (in KBr pallet; Thermo Electron Scientific Instruments LLC/ model Nicolet iS5), ^{1}H NMR and ^{13}C NMR (CDCl3:DMSO-d6(1:1); AVH D 500 AVANCE III HD 500 MHz spectrometer), MALDI-TOF (MS: Bruker AutoFlex Speed MALDI ToF),TGA(TGA-50 TGA) and DSC (DSC-60 Plus)(heating rate 10 ℃ min^{-1} in N_2-gas), HR-XRD (Rigaku Smart Lab 9 kW Powder type) equipped with Cu Kα X-Ray radiation source of $\lambda = 1.54$ Å, and morphological evaluation through High-resolution transmission electron microscopy (HRTEM) (model: Technai G2 20 TWIN).

The poly ((N-acryloyl phenylalanine methyl ester)) p(NAPA) and poly (N-acyloyl leucine methyl ester)) p(LME) NPs were also synthesized and characterized in the similar procedures as mentioned earlier using 500 mg of N-acryloyl phenylalanine methyl ester (NAPA) and N-acryloyl leucine methyl ester (LME) separately.

3.4.3.3. siRNA encapsulation. siRNA sequence was designed using WI siRNA selection program S5' CGGAUGAACUGAAGCGAAU UU and AS 3' UU GCCUACUUGACUUCGCUUA**,** this sequence is referred as the **siPOLR2A** and Sense-5'-Cy3 [mA] [mU][mG][2flA] [mA] [2fl C] [2fl U] [2fl G] [mA] [mA] [mG] [mC] [mG] [mA][mA][mU] UU 3' and Anti-sense [Phos] [mA] [mU] [mU] [mC] [mG] [2flC] [mU] [mU] [mC] [mA] [mG] [mU] [mU] [2flC] [mA] [2flU] * [mC]* [mC] *[mG] *[mU]*[mU] 3', this sequence referred as **5b-(A)-cy3-siPOLR2A**. For the encapsulation of siRNA, 10μM of

siRNA ≈ 100 ng mL^{-1} was mixed with 20, 10, and 5μM of p(NAPA-co-LME) and vacuum on/off cycle were conducted for 10 times/1min for each vacuum on/off cycle. The loading was performed at 4˚C temperature for 48 h. Afterword centrifugation was performed at 12000 g for 15 minutes. Reading for initial concentration of siRNA and for final concentration of siRNA were taken by using Nanodrop. An Agarose gel retardation assay was utilized to evaluate the siRNA loading on the p(NAPA), p(LME) and p(NAPA-co-LME) nanoparticles. The encapsulation efficiency was calculated using the following equation.

$$\boldsymbol{siRNA\ Encapsulation}\ \% = \frac{\boldsymbol{Total\ siRNA - free\ siRNA}}{\boldsymbol{Total\ siRNA}} \ldots\ldots\ldots\ldots\ldots\ldots\ldots\ldots\ldots (\mathbf{3.4.1})$$

It can be noted that the present (novel) siRNA sequence, novel modified siRNA sequence and siRNA formulations with p(NAPA), p(LME) and p(NAPA-co-LME) nanoparticles have been filed for the ***Indian Patent (Applied on 4th March 2024)***.

3.4.3.4. Serum stability of p(NAPA-co-LME)-siPOLR2A and p(NAPA-co-LME)-5b(A)-cy3-siPOLR2A nanocomplex.

Serum was collected from waster rat blood. The naked siPOLR2A, 5b(A)-cy3-siPOLR2A, p(NAPA-co-LME)-siPOLR2A and p(NAPA-co-LME)-5b(A)-cy3-siPOLR2A nanocomplex were incubated in 50% of rat serum in PBS (pH 7.4). After each interval of time 0, 3h, 9h, 12h, 24h and 48h, 20μL the samples were collected. To stop the nuclease activity samples were placed in 60˚C for 5 minutes and placed at -20˚C temperature. Afterword, samples were run on 2% of agarose gel. Intact siRNA nano complex was retained in well while degraded and fragments move towards of the gel.

3.4.3.5 In vitro cytotoxicity: 5000 MDA-MB cells were seeded in 96 well plate and incubated for 24 hours. After 50-60% of confluence, cells were treated with different combinations of siPOLR2A and 5b(A)-cy3-siPOLR2A nanocomplex, with drug, without drug, with particle and co-loaded particles for 24 hours. After the treatment, treatment media replaced with MTT reagent for 4h and absorbance were recorded at 570nm.

3.4.3.6 siRNA silencing. For the investigation of siRNA mediated silencing, western blot was performed. Cells were transfected with naked siPOLR2A, 5b(A)-cy3-siPOLR2A, p(NAPA-co-LME)-siPOLR2A and p(NAPA-co-LME)-5b(A)-cy3-siPOLR2A. For positive control siPOLR2A and 5b(A)-cy3-siPOLR2A were transfected with using Xtream gene siRNA transfection agent. 30ng of siRNA and 2µL of transfection agent mixed in 45µL of serum free DMEM for 10 min and placed for the treatment. While for the test group, the 30ng siRNA loaded p(NAPA-co-LME)-siPOLR2A and p(NAPA-co-LME)-5b(A)-cy3-siPOLR2A were directly placed in the cell culture medium and treated for 48 h. After the treatment all the dead and live cells were collected and washed with PBS and Lysis using RIPA buffer contains protease inhibitor. Then 15% SDS PAGE was run initially at 80 Volt (for 10 min) followed by 100 Volt till the proteins get separated. Then the proteins were transferred on PVDF membrane at 15 Volt for 30 min using semidry trans blot. Further PVDF membrane blocked with 5% Non-Fat milk at RT (25 ^{o}C) for 1h. Then it was treated with Anti-POlR2A antibody 1:1000 dilution in 5% Non-Fat milk -TBST buffer for overnight at 4˚C. After incubation and washing, treatment with Anti-mouse secondary antibody was performed for 2 h. Then the blot was washed with TBST. Then after adding the ECL substrate chemiluminiscent images were captured using syngene gel documentation system. Images were analysed using ImageJ software.

3.4.3.7 Cellular Internalization mechanism. To investigate endocytosis mechanism, endocytosis inhibitor assays were performed. For this, $10x10^5$ cells were seeded on 6 well plate for overnight. Then cells were treated with Chloropromazine (30μM), Nystatin (25μM and Amiloride (1.5mM) for one hour and without any treatment were considered as positive control for cellular uptake. After the treatment, cells were further treated with 50 μg mL^{-1} of rhodamine B loaded p(NAPA-co-LME) nanoparticles for 5 h. cells were washed, trypsinized and collected in PBS and flow cytometry uptake were quantitated using BD flow cytometer.

The LAT1 mediated internalization immunofluorescence studies were performed using p(NAPA-co-LME)-5b(A)-cy3-siPOLR2A nanocomplex. $10x10^5$ cells were seeded on 6 well plate for overnight. Cells were further treated with p(NAPA-co-LME)-5b(A)-cy3-siPOLR2A nanocomplex for 2 h and 6 hours. For immunofluorescence, cells were fixed with 4% paraformaldehyde for 20 min, permibalized with PBST buffer for 15 min, blocked with 2% BSA at RT for 1 h, and treated with primary Anti-LAT1 antibody 1:250 dilutions for overnight at 4˚C followed by secondary antibody treatment for anti-mouse-Alexa 488 labelled for 2 hours. After, washing cells mount on DABCO, and confocal microscopic images were collected and analysed.

3.4.3.8 Statistical analysis. All data presented were confirmed using at least 3 replicates for each of the experimental groups. The results are expressed as the mean of the values ± standard error of the mean. One-way ANOVA was performed to determine the statistical significance ($p < 0.05$), unless otherwise stated.

3.4.4. Results and Discussion

3.4.4.1. **Physical characterization.** Chemical functionalities of synthesized N-acryloyl-(L-phenylalanine methyl ester) and N- N-acryloyl leucine methyl ester were characterized and confirmed through FTIR, H NMR and ^{1}H NMR and ^{13}C NMR shown in Figure 3.4.1(a-b). The poly ((N-acryloyl-$_{L}$-phenylalanine methyl ester)-co-(N-acryloyl-leucine methyl ester)) [p(NAPA-co-LME)] polymer were synthesized through the mini-emulsion free radical polymerization technique. The p(NAPA-co-LME) NP, a homo-cross-linked polymer of p(NAPA) and p(LME) were also synthesized following the same mini-emulsion free radical polymerization technique, and the chemical conformations were confirmed through the FTIR, UV-Vis, ^{1}H NMR and ^{13}C NMR spectroscopy. In the FTIR spectrum, the presence of ─NH (stretched band) was observed at 3331 cm^{-1} for p(NAPA) (Figure 3.4.1c.1) and for p(LME) (Figure 3.4.1c.2), whereas for p(NAPA-co-LME) NP the band observed at at 3345 cm^{-1} (Figure 3.4.1c3). The band for aliphatic alkane (─CH_2) appeared at 2932 cm^{-1} for both p(NAPA) and p(LME), whereas for p(NAPA-co-LME) NP the band shifted to 2959 cm^{-1}. The bands appeared at 1746 cm^{-1}, 1730 cm^{-1} and 1746 cm^{-1} are for the presence of C=O (ester), and the bands appeared at 1655 cm^{-1}, 1642 cm^{-1} and 1665 cm^{-1} are for –NH-C=O of p(NAPA), p(LME) and p(NAPA-co-LME) NPs. Out-of-plane bending band was observed at 689 cm^{-1} for both p(NAPA) and p(NAPA-co-LME) and while it was absent in p(LME) polymer. This out of plane bending was observed due to an increase in the number of aromatic rings in p(NAPA-co-LME). Furthermore, UV-Vis spectrum also confirms the formation of p(NAPA-co-LME) NP with an absorption band for aromatic ring at 260 nm (Figure 3.4.1d). MALDI-ToF spectrum was obtained using a ditharnol matrix and chloroform: DMSO co-solvent for p(NAPA), p(LME) and p(NAPA-co-LME). The number average molecular weight (M_n) was

calculated to be 1704.379, 1622.9 Da, 1641.72 Da and, weight average molecular weight (M_w), was calculated to be 1788.28 Da, 1675.28 Da, 1720.172 Da, with PDI of 1.04, 1.03 and 1.04 for the respective polymers p(NAPA) (Figure 3.4.2.a), p(LME) (Figure 3.4.2.b), and p(NAPA-co-LME) (Figure 3.4.3.b).

3.4.4.2. **Morphology of p(NAPA-co-LME) NPs:** morphology and structural analysis were performed for the p(NAPA), p(LME), and p(NAPA-co-LME) using High-resolution transmission electron microscopy (HRTEM) (model: Technai G2 20 TWIN). The p(NAPA) particle shown in Figure 3.4.3.(a-e) are hollow with spherical in morphology with particle size ranging from 50 nm to 150 nm in diameter while p(LME) NPs shown in Figure 3.4.3.(f-i) are microporous in nature with spherical morphology and particle size ranging from 40-80 nm in diameter (pore size below 1nm). HRTEM macrograph of p(NAPA-co-LME) NPs (Figure 3.4.3.(k-o)) was revealed that particle were slightly spherical in shape with 50- 150 nm in diameter. The particles are also found with hollow central core with diameter of ~50 nm and with pore size of 1-2.5 nm was observed. Diffused ring patterns of SAED of p(NAPA), p(LME) and p(NAPA-co-LME) NPs revealed that all the types of particles are amorphous in nature. This is further confirmed with XRD (Figure 3.4.3,.c,h,m). The zeta potential for polymeric nanoparticles were calculated to be -35mV and -38 mV for p(NAPA) (Figure 3.4.4 (a)) and p(LME) (Figure 3.4.4 (b)) respectively, whereas the same has been reduced to -25 mV for p(NAPA-co-LME) NPs (Figure 3.4.4 (c)). Thus, this results revealed that the polymeric nanoparticle are colloidal stable in nature.

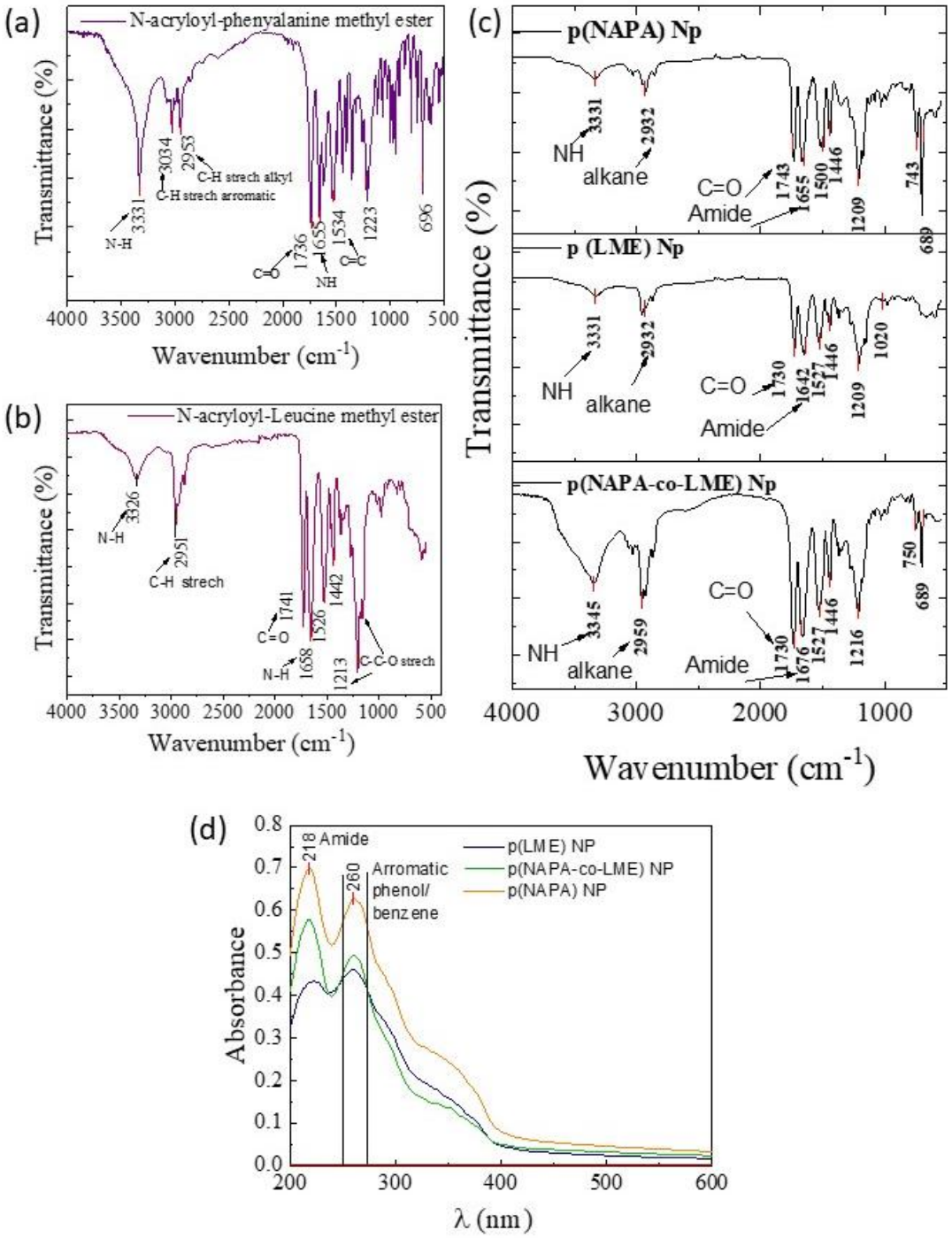

Figure 3.4. 1 FTIR spectra of (a) N-acryloyl phenylalanine methyl ester monomer, (b) N-acryloyl leucine methyl ester monomer, (c) poly (N-acryloyl phenylalanine methyl ester) NPs (p(NAPA)NP), poly(N-acryloyl Leucine methyl ester) NP p(LME), and poly[(N-acryloyl phenylalanine methyl ester)-co-(N-acryloyl Leucine methyl ester)] NP (p(NAPA-co-LEM)NP).(d) UV-Vis spectra of p(LME), p(NAPA) and p(NAPA-co-LEM) NPs.

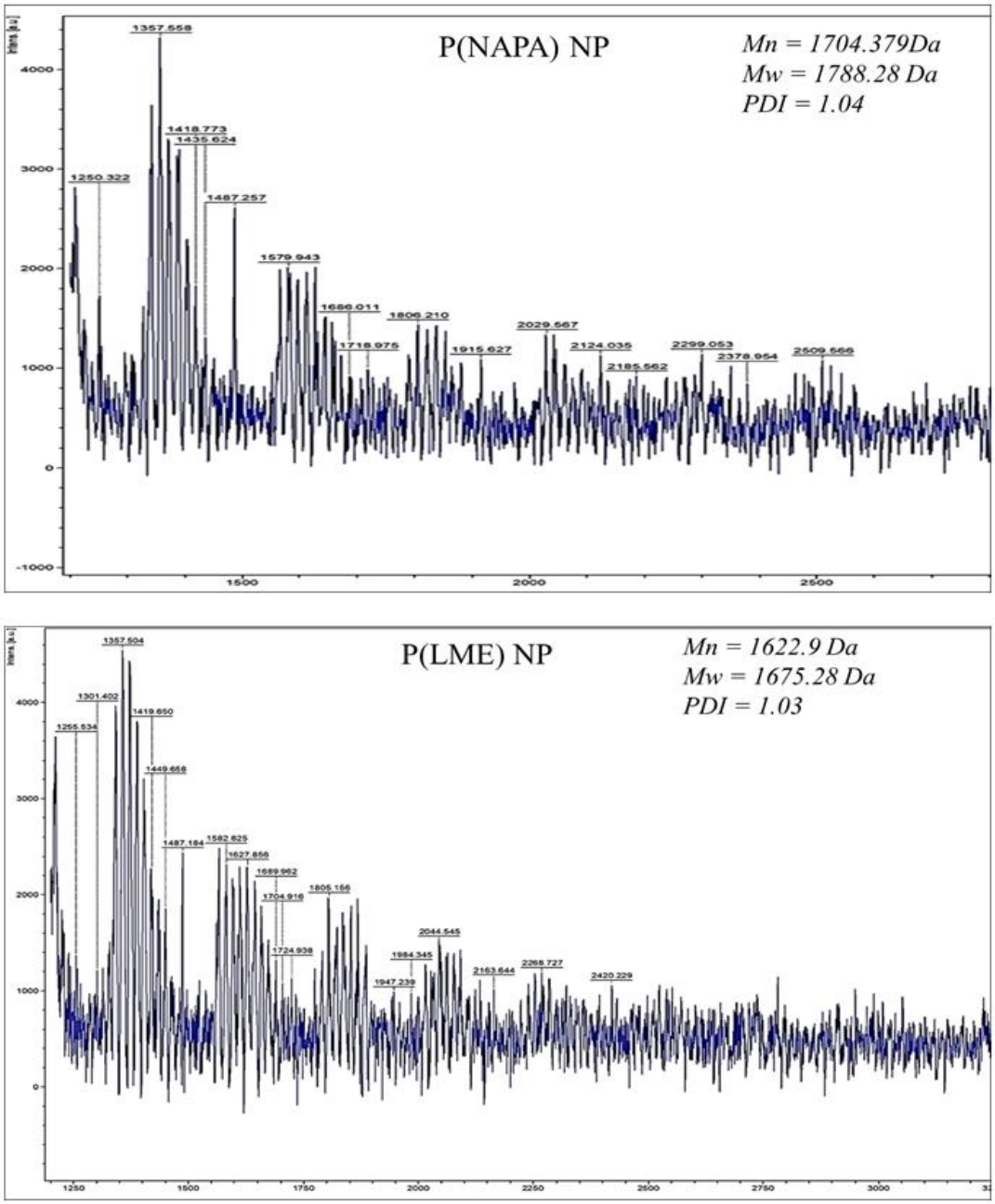

Figure 3.4.2. MALDI-ToF spectra of (a) p(NAPA) and (b) p(LME)

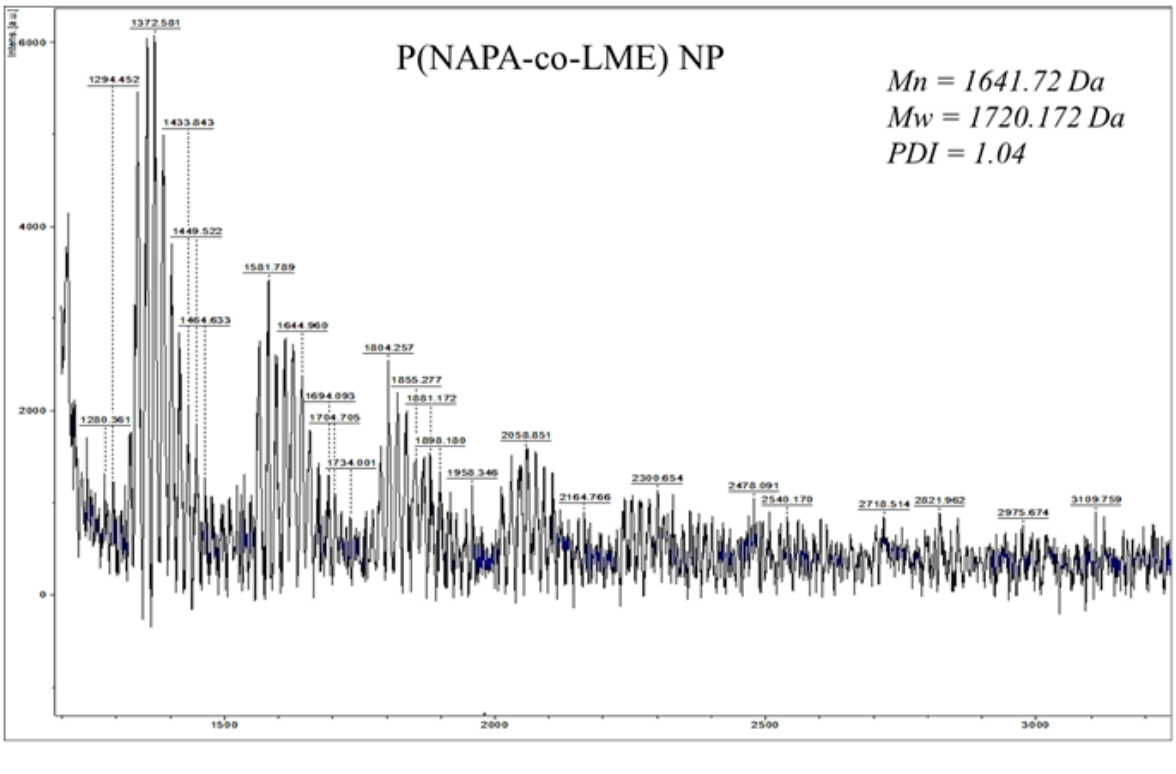

*Figure 3.4. 2(**c**) MALDI-ToF spectra of p(NAPA-co-LEM)NPs*

3.4.4.3. **Thermal stability of particles.** The thermal stability of the polymeric particles was studied through TGA. For p(NAPA) NPs and p(LME) NPs a 2-step TGA thermogram was obtained (Figure 3.4.5a and c). Whereas for the co-polymeric p(NAPA-co-LME) NPs a 3-stage TGA thermogram was observed (Figure 3.4.5d). In 1st step, an initial degradation was observed due to moisture or for low molecular weight polymers for both p(NAPA) NPs and p(LME). For p(NAPA-co-LME) NPs the 3rd phase of degradation was observed at 383 ˚C -542 ˚C with 28.5% mass loss due to the degradation of the high molecular mass polymers. Through the DSC, the glass transition was observed at -37.74 ˚C, -37.83 ˚C, and 34.69 ˚C for the p(NAPA) (Figure 3.4.5 b), p(LME) (Figure 3.4.5 d), and p(NAPA-co-LME) NPs (Figure 3.4.5 f), respectively. The endothermic transition with the highest peak position at 46.42℃ (ΔH_f= 2.37 Jg^{-1}), 48.22 ℃ (ΔH_f= 6.58 Jg^{-1}) and 47.30 ℃ (ΔH_f= 7.01 Jg^{-1}) were observed for p(NAPA)

(Figure 3.4.5 b), p(LME) (Figure 3.4.5 d), and p(NAPA-co-LME) NPs (Figure 3.4.5 f), respectively.

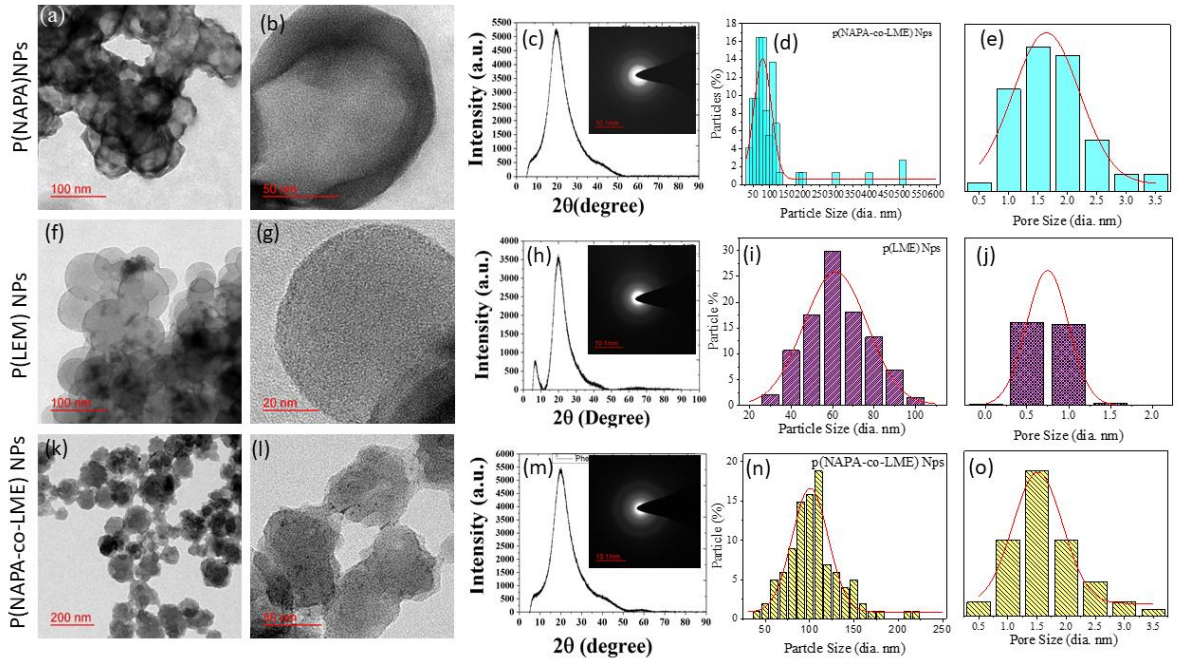

Figure 3.4. 3 Morphological characteristics of (a-e) p(NAPA), (f-j) p(LME) and (k-o) p(NAPA-co-LEM)NP. Figure (a, f and k) represent low magnification TEM macrographs. Figures (b,g and l) represent HRTEM macrographs of respective polymeric nanoparticles. Figures (c, h and m) represent the XRD of particles with SAED pattern obtain from HRTEM of respective polymer. Figures (d, i and n) show the particle size distribution of nanoparticles obtained from HRTEM micrographs and Figures (e, j and o) represent the pore size distribution of the obtained particles.

The rationale behind conducting a thermal degradation study for a polymer intended for *in vivo* use at 37°C (body temperature) is to assess its stability and performance under physiological temperature, which could ensure its safety, durability, functionality, and compliance with regulatory standards in biomedical applications. Our results show that p(NAPA-co-LME) NP are stable upto 279˚C temperature. And its applicability in physiological temperature was clarify by the results obtained from the DSC analysis where its shows that the melting of

p(NAPA-co-LME) NP at the physiological range will be helpful in release study. However, our study has the limitation that we have not studied the release behavior which will be the future scope of this work. And hence, we can conclude that This endothermic heat flow in physiological temperature will help in the delivery of the drug at the physiological condition.

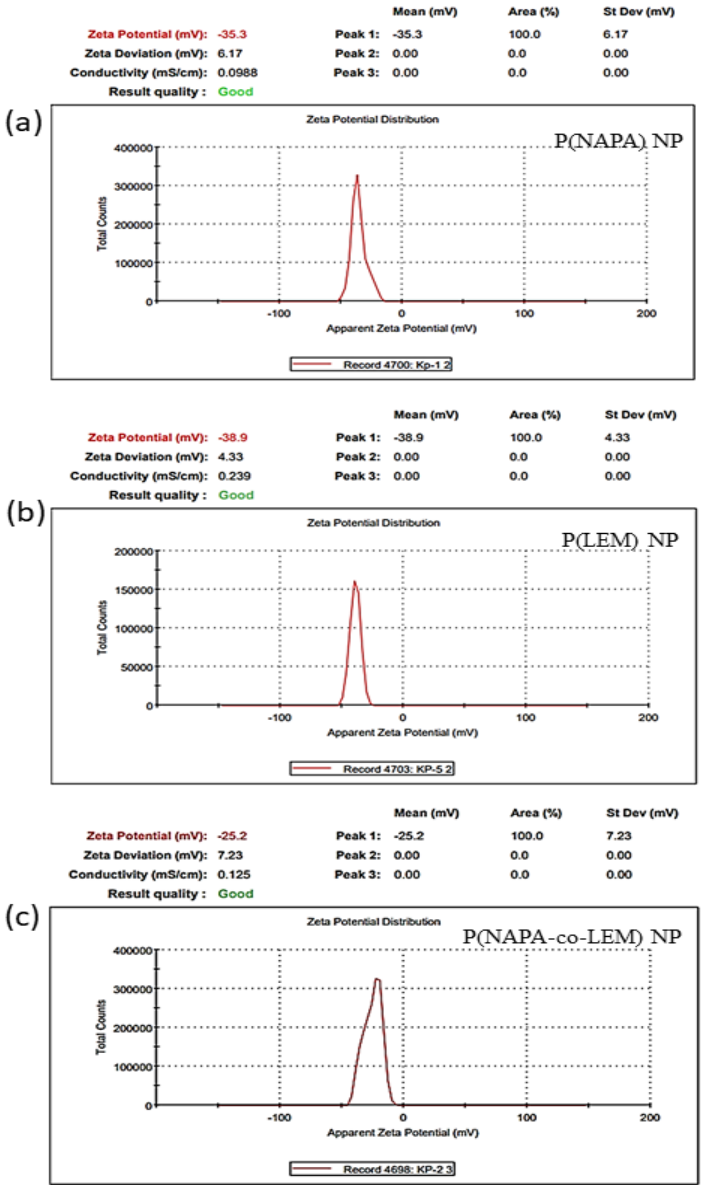

Figure 3.4. 4 Zeta potential of (a) p(NAPA), (b) p(LME) and (d) p(NAPA-co-LEM) NPs

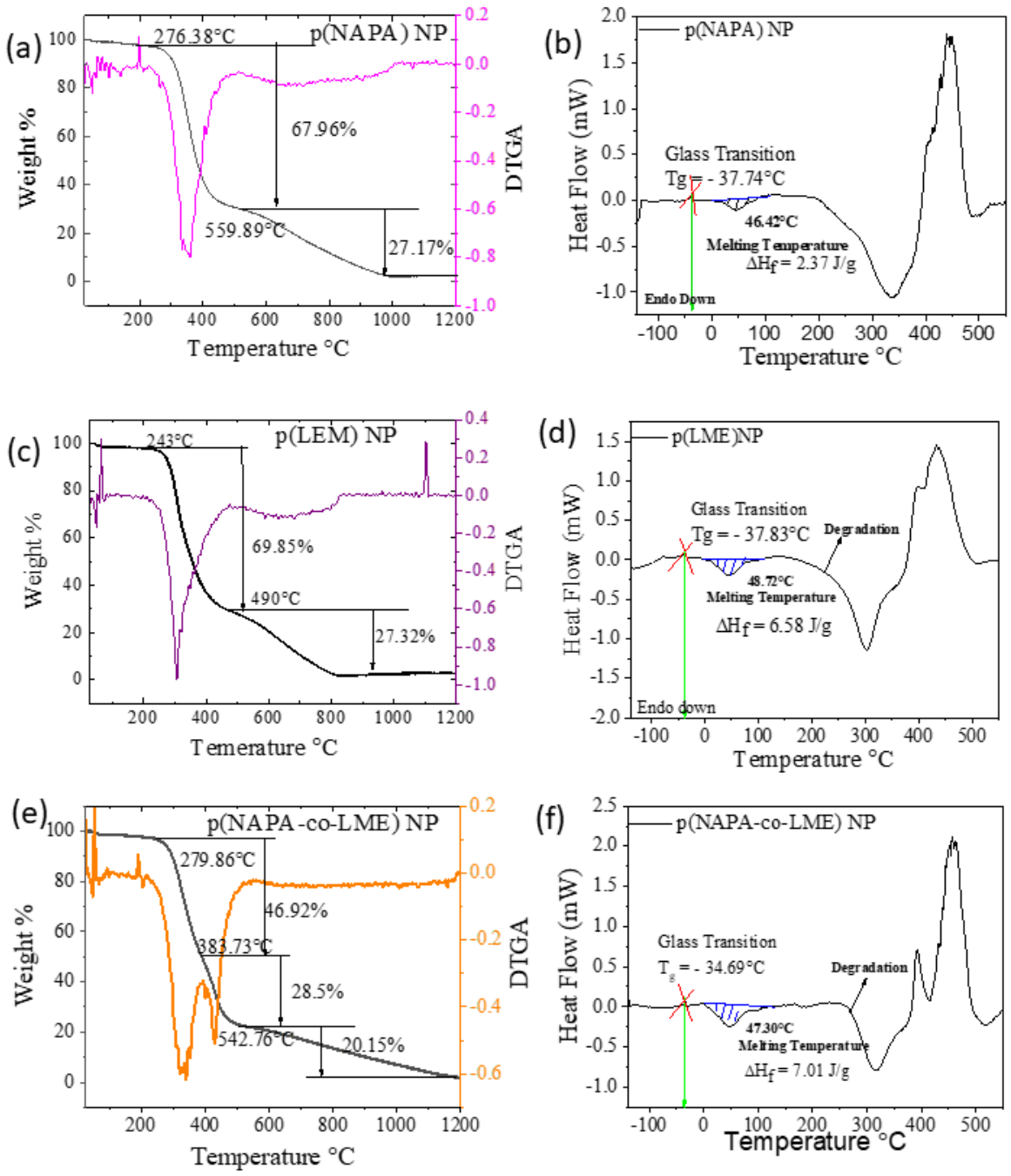

Figure 3.4. 5 Thermogravimetric analysis (TGA) and Differential Scanning Calorimetry (DSC) of (a-b) p(NAPA), (c-d) p(LME) and (e-f) p(NAPA-co-LME) NPs

3.4.4.4. **Heparanase inhibitory activity of the particles**. The suitability of the particles for further biological applications was decided based on the heparanase inhibitory activity. For this, 500 ng, 1000 ng, 5000 ng and 1000 ng of NPs were incubated with Fondaparinux sodium and 200 ng of heparanase enzyme for 24 hours. Reactions were terminated by increasing the temperature and pH. Enzymatically heparanase cleaves the Fondaparinux sodium and produces an aldehyde group at the reducing terminal which reduced the resazurin and emit the fluorescence at the excitation wavelength of 560 nm and emission at 590 nm. Among all the type of nanoparticles, p(LME)NP and p(NAPA-co-LME) particles shown the heparanase inhibitory activity at 1000 ng of particle (Figure ***3.4.6***).

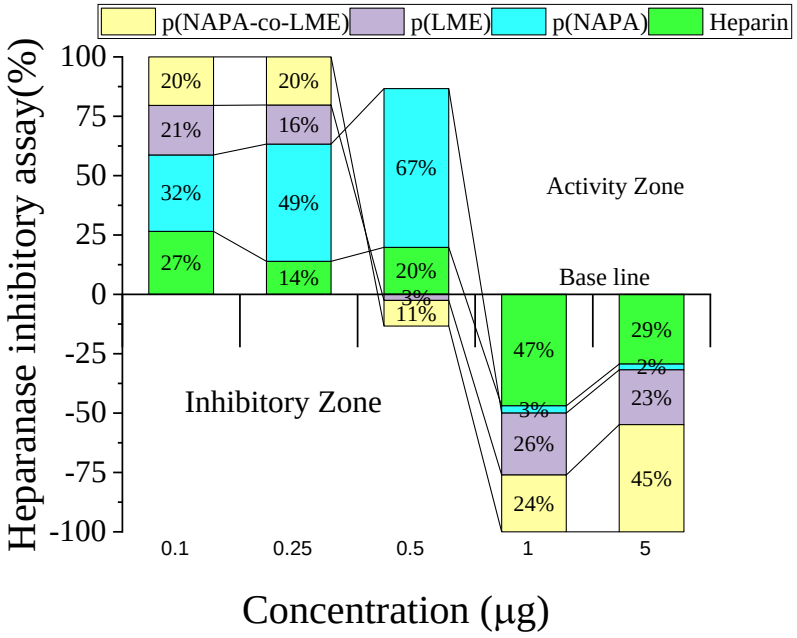

Figure 3.4. 6 Comparative Heaparanse inhibitory activity of p(NAPA), p(LME) and p(NAPA-co-LME) NPs.

3.4.4.5. siPOLR2A encapsulation and serum stability of p(NAPA-co-LME)-co-siPOLR2A complex. To evaluate the encapsulation efficiency of the siRNA in polymeric particle, siRNA and particle in ratios of 1: 20 ng, 1: 30 ng, and 1: 60 ng (siRNA: NPs) were

incubated at 4˚C for 48 h with 10 time on/off cycle of vacuum at 8h of interval and allowed for the complex formation. The encapsulation of siRNA by p(NAPA) (Figure 3.4.7 a), p(LME)NP (Figure 3.47.b) and p(NAPA-co-LME) (Figure 3.4.7 c), particle were conformed though the agarose gel electrophoresis. As shown the highest encapsulation efficiency was observed in p(NAPA-co-LME) (Figure 3.4.7 c) as compared to the p(NAPA) and p(LME) NPs. We have calculated that 1ng of siRNA consists of 4.63X 10^{10} of siRNA copies. siRNA quantification was conducted before loading and after loading through the nanodrop. Accordingly, the siRNA encapsulation efficiency in p(NAPA-co-LME) Np was calculated that 1ng of particle uptake the 0.03ng of siRNA which is equivalent to the 0.14 X 10^{10} number of siRNA copies and this encapsulation efficiency is extra ordinary. To address the stability of p(NAPA-co-LME)-co-siPOLR2A complex against the nucleases, free duplex siPOLR2A (Figure 3.4.7 d), 5-base-assymetric-Cy3-siPOLR2A (5b(A)Cy3-siPOLR2A) (Figure 3.4.7 e), p(NAPA-co-LME)-co-siPOLR2A (Figure 3.4.7 f) and p(NAPA-co-LME)-co-(5b(A)Cy3-siPOLR2A) (Figure 3.4.7 g), complex was incubated with 50% mouse serum at 37˚C temperature in shaker incubator. As shown in Figure free duplex siPOLR2A were completely degrade within 3 hours of incubation while designed and synthesized 5b(A)Cy3-siPOLR2A showed stable up to 48 h or higher duration. Further, when duplex siRNA was loaded in p(NAPA-co-LME), the stability of p(NAPA-co-LME)-co-siPOLR2A and p(NAPA-co-LME)-co-(5b(A)Cy3-siPOLR2A) complex was observed to be stable up to 48 h or more than 48h.

3.4.4.6. Cell Viability of p(NAPA-co-LME) NPs and p(NAPA-co-LME)-co-siPOLR2A complex

To evaluate the biocompatibility of p(NAPA-co-LME) NPs on normal cell (HepG2, PC12 and L929) (Figure 3.4.8a) and cancer cells (MDAMB-231 and LN229), were incubated with

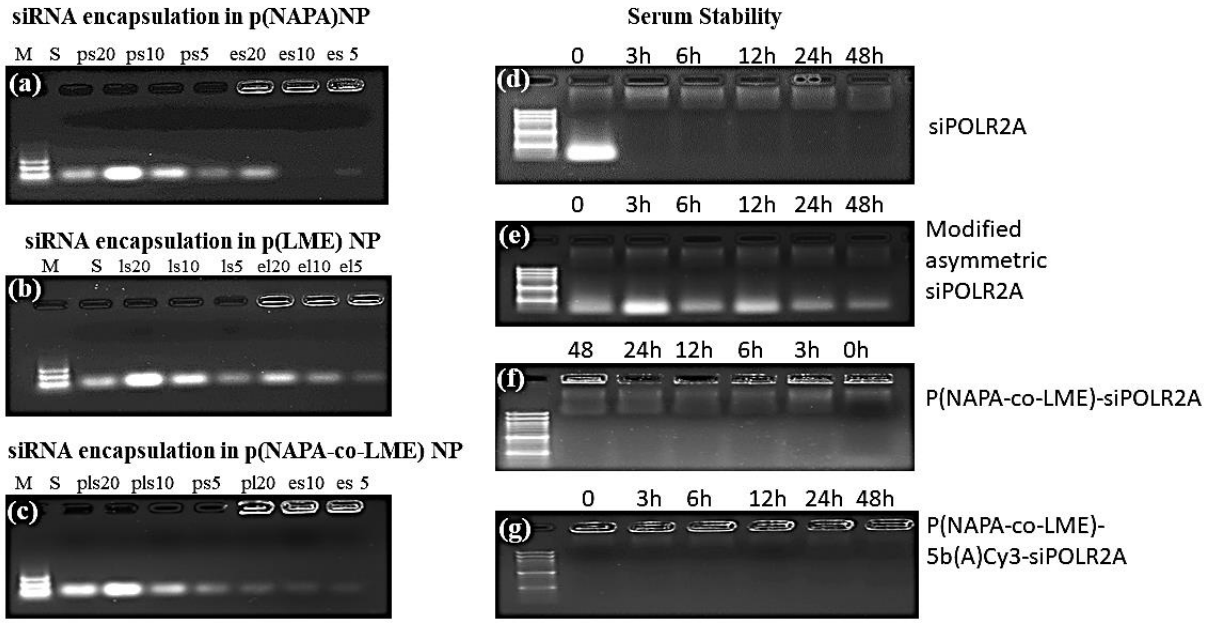

Figure 3.4. 7 siRNA encapsulation and serum stability. Figs. (a-c) represent the siRNA encapsulation in p(NAPA), p(LME) and p(NAPA-co-LME) NPs, where 'M' represent 100 bp ladder, 'S' represents the naked duplex siRNA, ps, ls, and pls- represent supernatant siRNA of different concentration of 20μM (≈200ng) siRNA, 10μM (≈100ng) siRNA and 5 μM (≈50ng) siRNA with respective type of nanoparticle; es, el and pl- represent the encapsulated siRNA in p(NAPA)NP, p(NALE) NP and p(NAPA-co-NALE) NP, lane 4, 5, 6 of each gel of a, b and c represent supernatant obtained after siRNA encapsulation and lane 7, 8 and 9 represent encapsulated particle. Figs. d-g represent the serum stability: (d) naked duplex siPOR2A, (e) naked 5-base-assymetric-Cy3-siPOLR2A, (f) p(NAPA-co-LME)-co-siPOLR2A and (g) p(NAPA-co-LME)-co-(5b(A)Cy3-siPOLR2A) complex at different time interval lane 1-100bp ladder, lane 2-7 different time interval 0, 3, 6, 12, 24 and 48 h.

Different concentrations of p(NAPA-co-LME) NPs. It was observed that 100% cell viability was observed in PC12 cells in almost all concentrations of p(NAPA-co-LME) NPs, and L929 cells were 80% viable and HepG2 of 100 % at 1000 μg mL^{-1} of particles. p(NAPA-co-LME) NPs shows the cytotoxicity towards the cancer cell lines MDA-MB-231, 70% cells are viable at 1000 μg mL^{-1} concentration, and for LN229 IC50 reached at the concentration of 100 μg mL^{-1} (Figure 3.4.8). POLR2A is an emerging target in loss of TP53 [29]. POLR2A expression

has been correlated with the different forms of cancer cell cycle progression and facilitates the transcription of different forms of CDKs [27]. Therefore, in the present study siRNA were designed against the POLR2A and Flouro and methyl, modifications were incorporated into nucleobase to induce the silencing efficiency and induce serum stability. We have observed that this modified 5-base-asymmetric-Cy3-siPOLR2A alone shows high stability against the nucleases. Duplex siPOLR2A and 5-base-asymmetric-Cy3-siPOLR2A were transfected in the MDA-MB-231 cell line using the transfection agent with different concentrations of 10 ng, 30 ng and 50 ng and it is observed that the cell viability was decreased with the viability of 65-55% both the siRNA (Figure 3.4.8.c). However, in siRNA encapsulated nanoparticle p(NAPA-co-LME)-co-5b(A)Cy3-siPOLR2A complex showed the equivalent transfection efficiency and cell killing ability like marketed Xtreme gene siRNA transfection agent and higher compared to the p(NAPA-co-LME)-co-siPOLR2A complex. Further, paclitaxel (PTX) has been loaded in same p(NAPA-co-LME) NPs to evaluate the cytotoxicity towards the MDA-MB-231 cell line. PTX and PTX loaded p(NAPA-co-LME) NPs shows that the 69-70% cells are viable at 12 μg mL^{-1} concentration of PTX and PTX loaded p(NAPA-co-LME) NPs. Interestingly, among the all different concentration of PTX and p(NAPA-co-LME) + PTX NPs, at the 30 ng mL^{-1} of 72% and 70% of cell viability were observed for the respective materials shown in (Figure 3.4.8.d). Although, presently our study has the limitation that we have not checked the cell viability below 30ng of concentration, which will be conducted in future study. From the siRNA-induce cell viability data, the concentration of siPOLR2A was restricted for 30 ng mL^{-1}. Furthermore, to evaluate the siPOLR2A and PTX combination approaches, siPOLR2A: PTX were used in 1:1, 1:10 and 1:100 ratios and the cell viability was studied. Among all the three type of combination, 1:1 combination showed good reduction in

cell viability. In treatment of siPOLR2A: PTX (1:1), 5b(A)Cy3-siPOLR2A: PTX (1:1) and p(NAPA-co-LME) +PTX NPs, almost equal % of cell viability was observed. Reduction in 20% of cell viability was observed in p(NAPA-co-LME)-co-(5b(A)Cy3-siPOLR2A): p(NAPA-co-LME) +PTX (1:1) combination compared to the other combination as showed in Figure 3.4.8.e. For the both co-loaded particle p(NAPA-co-LME)- siPOLR2A and p(NAPA-co-LME) -(5b(A)Cy3-siPOLR2A-PTX treatment to ≈38% decrease in cell viability were Observed at the 30 ng mL^{-1} of concentration compared to the control. Further silencing of POLR2A were confirmed through the western blot as showed in Figure 3.4.9. It has been showed that 5b(A)Cy3-siPOLR2A silencing efficiency were higher compared to duplex siPOLR2A.

3.4.4.7 **Cellular uptake and Internalization mechanism of p(NAPA-co-LME) NPs and p(NAPA-co-LME)-co-siPOLR2A complex.** For any silencing or drug delivery it is important that particle should be internalize and for the effective silencing particle should have the ability to endosome lysosome escape. Cell uptake the nanoparticles were confirmed through the flow cytometry (Figure 3.4.10 c). To elucidate the nanoparticle uptake mechanism, the cells were treated with the chloropramazin (Figure 3.4.10 d), amilride (Figure 3.4.10 e) and nystatin (Figure 3.4.10 f). Chloropramazin inhibits the clathrin mediated endocytosis and nystatin inhibit the calveoli mediated endocytosis. And amiloride inhibits the Na+/H+ exchange. Our flow cytometry results showed that with the treatment of chloropramazin, cellular uptake of the particle was investigated (Figure 3.4.10 d), while with treatment with the other drug, nanoparticle uptake was not altered and hence we can consider that particle internalized through the clathrin mediated endocytosis.

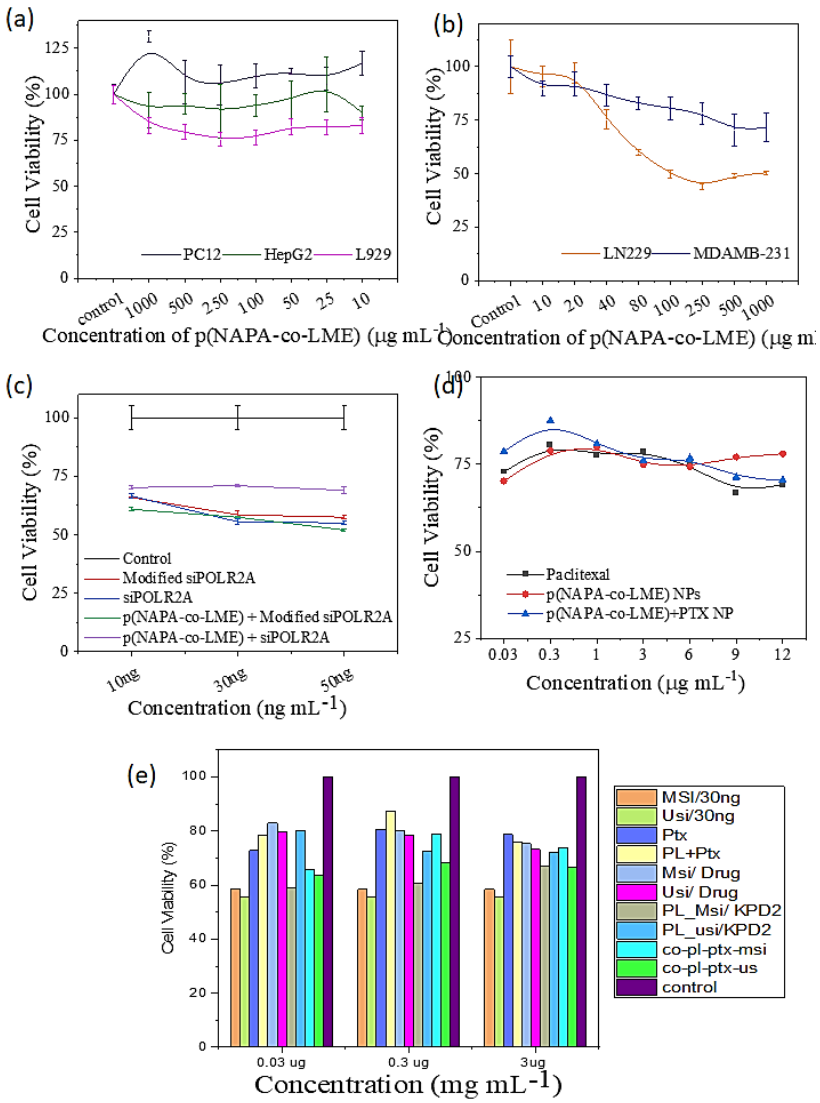

Figure 3.4. 8 Cell Viability of p(NAPA-co-LME) NPs and p(NAPA-co-LME)-co-siPOLR2A complex: (a) treatment with different concentrations of p(NAPA-co-LME) particles to normal cell line PC12, HepG2 and L929 and cell viability (b) cytotoxicity of cancer cell in response to p(NAPA-co-LME) particles, (c) MDA-MB 231 cell viability in response to paclitaxel(ptx) and p(NAPA-co-LME) +PTX NPs, (d) MDA-MB-231 cell viability in response to the siPOLR2A (loaded and naked siRNA) and (e) MDA-MB-231 cell viability in response to different combinations of siRNA: Drug and co-loaded particles.

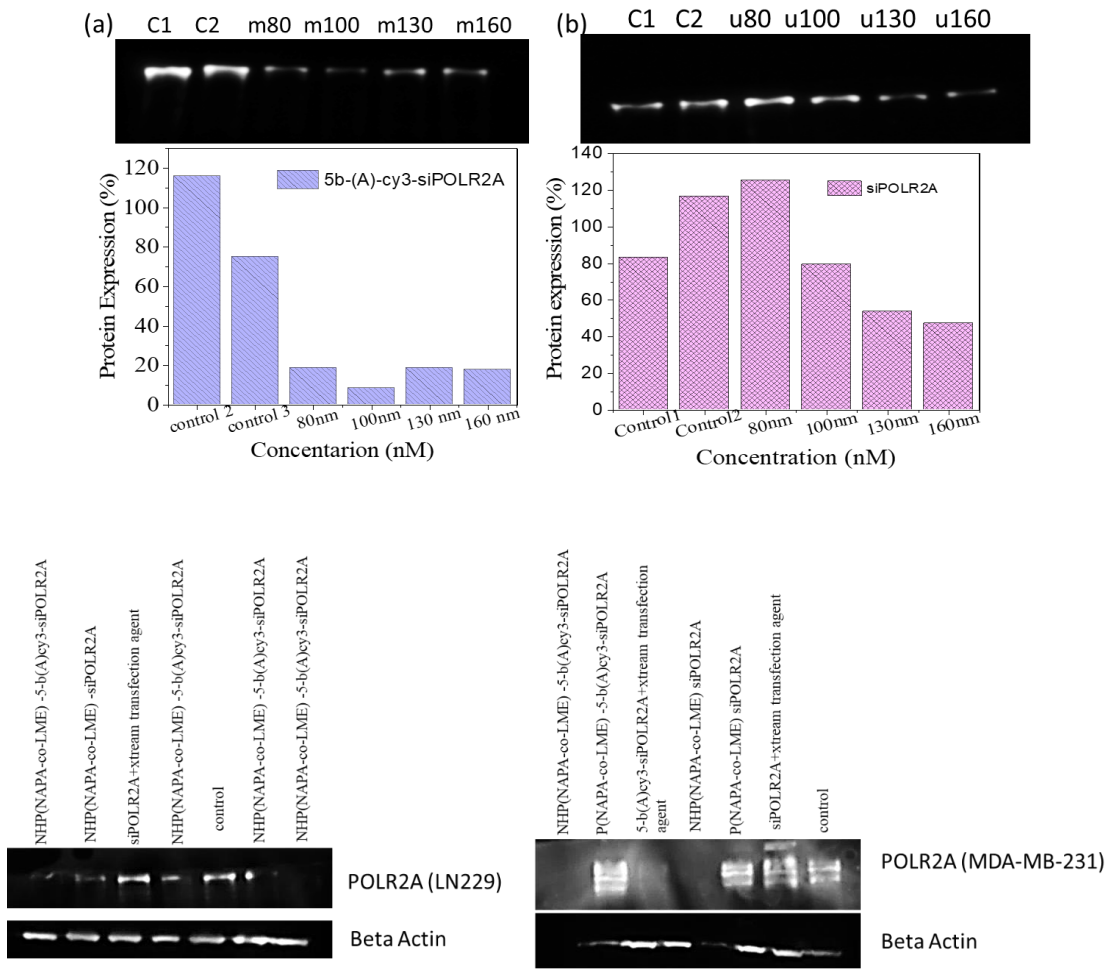

Figure 3.4. 9 Western blot of POLR2A (217 kDa) (a) silencing with 5b(A)Cy3-siPOLR2A and (b) silencing with duplex siPOLR2A

As per literature, it can be noted that in breast cancer SCL7A5 (LAT1 transporter) is highly up and unregulated. [31] It is also facilitating the transport of high affinity for branched chain amino acid such as leucine, phenylalanine, and tryptophan etc. The expression of SLC7A5 is regulated by HIF2α and therefore, it is highly expressed cancer cells as in cancer hypoxia is observed majorly.[32] As per our co-localization study for LAT1 expression in MDA-MB-231 and P(NAPA-co-LME)-5b(A)Cy3-siPOLR2A, it is started to co-localized within 2 hours and it increases in 6 h, represented by orange dots and inside red dots represent the release of siRNA

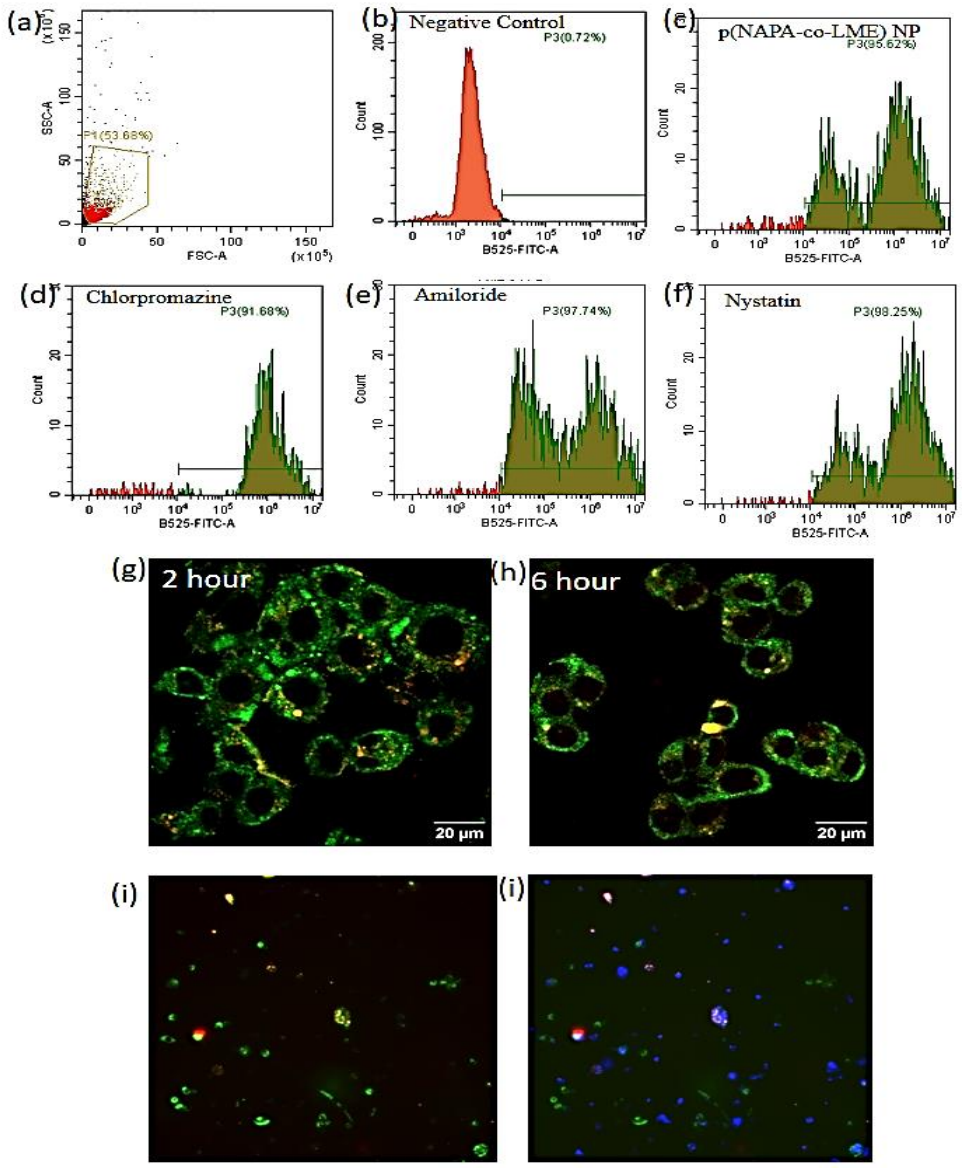

Figure 3.4. 10 Figure 3.9.10 Cellular Internalization mechanism and endolysosomal escape. Fig (a-f): show flow cytometry based cellular uptake of NP, Fig (c), cellular uptake in response to the different inhibitors, (d) chloropramazin, (e) amilroid and (f) Nystatin. Figs. (g-h) confocal microscopic images of LAT1 mediated internalization of P(NAPA-co-LME)-5b(A)Cy3-siPOLR2A at 2 hours and 6 hours. (I and J) endolysozomal escape.

intracellular cytoplasm. Hence, our results conclude p(NAPA-co-LME)-5b(A)Cy3-siPOLR2A internalized through LAT1 transporter represented in Figure 3.4.10 g-h, which enhance selectivity of this particles towards the cancer cells and which reduces the drug associated future toxicity. Furthermore, to confirm the endolysozomal escape and internalization of particle in in cytoplasm, particles were tracked in lysotracker stained reason. We observed distinct red color dots outside the nuclease and lysosome and some orange color dots represent complex particle present in endolysozome represent that our particle follow the endolysozomal mechanism. Hence, we can conclude that these particles have potential in co-delivery of the siRNA and paclitaxel

3.4.5 CONCLUSIONS

In this work, we have successfully synthesized *p(NAPA-co-LME) NPs* of size 150 nm in dia, and with an average molecular weight of Mc≈1622.9Da. These particles are amorphous in nature. The zeta potential value for these particles of -25.2mV revealed that the particles are moderately stabile. Further, p(NAPA-co-LME) NPs shows the highest heparanse inhibitory potential than p(NAPA) and P(LME), and provides synergistic effect in neo-antiangiogenesis. p(NAPA-co-LME) NPs has 60% of encapsulation efficiency of siPOLR2A. our designed 5b(A)-cy3-siPOLR2A shows higher stability and silencing efficiency compared to the siPOLR2A. These nanoparticles effectively can deliver the siRNA to cytoplasm for effective silencing of target gene via the clathrin mediated endocytosis and internalization through the LAT1 transporter which enhances its applicability towards the specific cancer cells compare to normal cells. Our results indicate the future potential of this 5b(A)-cy3-siPOLR2A-PTX-P(NAPA-co-LME) complex in treatment of heparanase driven aggressive malignancies.

REFERENCES.

1. Tian, Z., et al., *Insight Into the Prospects for RNAi Therapy of Cancer*. Front Pharmacol, 2021. **12**: p. 644718.
2. Hattab, D., A.M. Gazzali, and A. Bakhtiar, *Clinical Advances of siRNA-Based Nanotherapeutics for Cancer Treatment.* Pharmaceutics, 2021. **13**(7).
3. Mayfosh, A.J., T.K. Nguyen, and M.D. Hulett *The Heparanase Regulatory Network in Health and Disease*. International Journal of Molecular Sciences, 2021. **22**, DOI: 10.3390/ijms222011096.
4. Jayatilleke, K.M. and M.D. Hulett, *Heparanase and the hallmarks of cancer.* Journal of Translational Medicine, 2020. **18**(1): p. 453.
5. Zahavi, T., et al., *Heparanase: a potential marker of worse prognosis in estrogen receptor-positive breast cancer.* npj Breast Cancer, 2021. **7**(1): p. 67.
6. Ezrahi, S., A. Aserin, and N. Garti, *Basic principles of drug delivery systems – the case of paclitaxel.* Advances in Colloid and Interface Science, 2019. **263**: p. 95-130.
7. Sharifi-Rad, J., et al., *Paclitaxel: Application in Modern Oncology and Nanomedicine-Based Cancer Therapy.* Oxid Med Cell Longev, 2021. **2021**: p. 3687700.
8. Yakati, V., et al., *Enhancing the anticancer effect of paclitaxel by using polymeric nanoparticles decorated with colorectal cancer targeting CPKSNNGVC-peptide.* Journal of Drug Delivery Science and Technology, 2022. **68**: p. 103125.
9. Sun, H., et al., *Polymers in the Co-delivery of siRNA and Anticancer Drugs for the Treatment of Drug-resistant Cancers.* Topics in Current Chemistry, 2017. **375**(2): p. 24.
10. Xia, Y., J. Tian, and X. Chen, *Effect of surface properties on liposomal siRNA delivery.* Biomaterials, 2016. **79**: p. 56-68.
11. Biswas, S. and V.P. Torchilin, *Dendrimers for siRNA Delivery.* Pharmaceuticals (Basel), 2013. **6**(2): p. 161-83.
12. Aliabadi, H.M., et al., *Supramolecular assemblies in functional siRNA delivery: Where do we stand?* Biomaterials, 2012. **33**(8): p. 2546-2569.
13. Na, H.-K., et al., *Efficient Functional Delivery of siRNA using Mesoporous Silica Nanoparticles with Ultralarge Pores.* Small, 2012. **8**(11): p. 1752-1761.

14. Luo, K., et al., *Co-delivery of paclitaxel and STAT3 siRNA by a multifunctional nanocomplex for targeted treatment of metastatic breast cancer.* Acta Biomaterialia, 2021. **134**: p. 649-663.
15. Zheng, M., et al., *Poly(α-l-lysine)-based nanomaterials for versatile biomedical applications: Current advances and perspectives.* Bioactive Materials, 2021. **6**(7): p. 1878-1909.
16. Richter, F., et al., *The impact of anionic polymers on gene delivery: how composition and assembly help evading the toxicity-efficiency dilemma.* Journal of Nanobiotechnology, 2021. **19**(1): p. 292.
17. Kubo, T., et al., *SiRNAs conjugated with aromatic compounds induce RISC-mediated antisense strand selection and strong gene-silencing activity.* Biochem Biophys Res Commun, 2012. **426**(4): p. 571-7.
18. Troiber, C., et al., *Stabilizing effect of tyrosine trimers on pDNA and siRNA polyplexes.* Biomaterials, 2013. **34**(5): p. 1624-1633.
19. Shui, M., et al., *Engineering polyphenol-based carriers for nucleic acid delivery.* Theranostics, 2023. **13**(10): p. 3204-3223.
20. Shen, W., et al., *Natural Polyphenol Inspired Polycatechols for Efficient siRNA Delivery.* CCS Chemistry, 2020. **2**(3): p. 146-157.
21. Xu, M., et al., *Up-Regulation of LAT1 during Antiandrogen Therapy Contributes to Progression in Prostate Cancer Cells.* The Journal of Urology, 2016. **195**(5): p. 1588-1597.
22. Shimizu, A., et al., *Prognostic significance of L-type amino acid transporter 1 (LAT1) expression in cutaneous melanoma.* Melanoma Research, 2015. **25**(5).
23. Kanai, Y., *Amino acid transporter LAT1 (SLC7A5) as a molecular target for cancer diagnosis and therapeutics.* Pharmacology & Therapeutics, 2022. **230**: p. 107964.
24. Lopes, C., C. Pereira, and R. Medeiros *ASCT2 and LAT1 Contribution to the Hallmarks of Cancer: From a Molecular Perspective to Clinical Translation*. Cancers, 2021. **13**, DOI: 10.3390/cancers13020203.
25. Yamala, A.K., et al., *Poly-N-acryloyl-(l-phenylalanine methyl ester) hollow core nanocapsules facilitate sustained delivery of immunomodulatory drugs and exhibit adjuvant properties.* Nanoscale, 2017. **9**(37): p. 14006-14014.

26. Yamala, A.K., et al., *P-LME polymer nanocapsules stimulate naïve macrophages and protect them from oxidative damage during controlled drug release.* Journal of Applied Polymer Science, 2020. **137**(6): p. 48363.
27. Jiang, Q., et al., *POLR2A Promotes the Proliferation of Gastric Cancer Cells by Advancing the Overall Cell Cycle Progression.* Front Genet, 2021. **12**: p. 688575.
28. Xu, J., et al., *Precise targeting of POLR2A as a therapeutic strategy for human triple negative breast cancer.* Nat Nanotechnol, 2019. **14**(4): p. 388-397.
29. Liu, Y., et al., *TP53 loss creates therapeutic vulnerability in colorectal cancer.* Nature, 2015. **520**(7549): p. 697-701.
30. Mao, C.G., et al., *BCAR1 promotes proliferation and cell growth in lung adenocarcinoma via upregulation of POLR2A.* Thorac Cancer, 2020. **11**(11): p. 3326-3336.
31. Saito, Y. and T. Soga, *Amino acid transporters as emerging therapeutic targets in cancer.* Cancer Science, 2021. **112**(8): p. 2958-2965.
32. Bhutia, Y.D., et al., *Amino Acid Transporters in Cancer and Their Relevance to "Glutamine Addiction": Novel Targets for the Design of a New Class of Anticancer Drugs.* Cancer Research, 2015. **75**(9): p. 1782-1788.